EMISSION, SCATTERING AND ABSORPTION OF RADIATION IN CIRRUS CLOUD LAYERS

by

HERBERT JACOBOWITZ

B.S., BROOKLYN COLLEGE
(1960)

M.S., UNIVERSITY OF MARYLAND
(1965)

SUBMITTED IN PARTIAL FULFILLMENT

OF THE REQUIREMENTS FOR THE

DEGREE OF DOCTOR OF

PHILOSOPHY

at the

MASSACHUSETTS INSTITUTE OF

TECHNOLOGY

September, 1970

Signature of Author .....
Department of Meteorology, July 2, 1970

Certified by .....
Thesis Supervisor

Accepted by .....
Chairman, Departmental Committee
on Graduate Students

EMISSION, SCATTERING AND ABSORPTION OF RADIATION IN CIRRUS CLOUD LAYERS

by

Herbert Jacobowitz

Submitted to the Department of Meteorology on July 6, 1970, in partial fulfillment of the requirement for the degree of Doctor of Philosophy.

Abstract

The effect that cirrus clouds have upon the radiation emitted to space from the earth-atmosphere system is studied theoretically using a matrix method for computing the transfer of radiation in model cloud layers. The matrix method, which in essence is a generalization of a multi-streams approximation, is used to obtain the thermal radiation emitted by the clouds as well as their transmissivities to radiation from below. However, in order to perform these computations it is necessary to determine some of the physical characteristics of the clouds such as the form, size, and orientation of the ice crystals, the ice concentration, temperature distribution, etc.

By studying photographs of ice crystals collected in cirrus clouds, information with respect to the size and form of the crystals is obtained. Deductions from visual optical phenomena and laboratory studies of falling bodies which simulate ice crystals falling in air lead to the conclusion that the crystals are randomly oriented in any horizontal plane in the cloud but are not random in all three dimensions. The long axes of hexagonal columns tend to align themselves more with the horizontal plane than with any other plane.

Utilizing this information about the ice crystals, the angular patterns of the radiation scattered by the individual crystals are obtained. For the infrared wavelengths studied and the sizes of the crystals involved, it is concluded that refraction through the crystals is negligible and that the scattering patterns could be well approximated by Kirchhoff diffraction and surface reflection. It is further shown that if the ice crystals were approximated by circular cylinders, the diffraction pattern for crystals randomly oriented in either a plane or in three dimensions would be nearly identical to that for spheres which scatter the same total amount of energy as that scattered by the crystals.

In the case that radiation in the visible portion of the spectrum is scattered, refraction must be taken into account and therefore the above spherical approximations are not valid. For this radiation, a method is described for computing the angular pattern of radiation scattered by hexagonal crystals which makes use of the laws of geometric optics. It is shown that by tracing the paths of a large number of parallel rays through the crystals, the scattering pattern is sufficiently determined.

Before applying the above results to a computation of the radiation in cirrus layers, the matrix method is tested by performing computations of the angular reflection patterns from model stratus clouds and comparing them with observations made from an airplane over stratus clouds. The comparisons give one confidence in applying the method to cirrus layers.

Computations are then performed for 120 cloud models, whose parameters were chosen to cover the range of possibility of the physical characteristics of actual cirrus clouds. It is found that unless the ice concentration approaches .1 g/m^3, a value unlikely in most cirrus layers, the cloud will not radiate as a blackbody, but rather at a much lower value.

The results of the computations are used in conjunction with the observations by the SIRS radiometer aboard the Nimbus III spacecraft, when cirrus was in the field of view, to study the characteristics of cirrus clouds that could account for the observed radiances. In one particular case, the models give a wide range of values of the geometric thickness and ice concentration that would account for the observed radiances. However, it is noticed that the values of the product of the ice concentration and geometric thickness do not vary by more than about 50 percent. It is shown that the visible optical thickness depends upon such a product. Therefore, it is concluded that the models mainly provide information about the optical thickness of the cirrus layer. The cloud model solutions that result are moderately thin optically. This is consistent with the cirrus observed in satellite photographs of the region of observation taken at the same time that the SIRS observations were made.

Analysis of a second case provided no consistent cloud parameters. After some study it was concluded that the surface temperature was probably too low, causing the radiances in the window channel to be too low. Since the channel at 750.0 cm^{-1} would also be affected, only the remaining two channels are considered in determining the cloud parameters that would fit the observations.

Recommendations for future studies that are needed to resolve some of the remaining problems are made.

Thesis Supervisor: Henry G. Houghton
Title : Professor of Meteorology

BIOGRAPHY

The author was born in New York City, New York, on July 2, 1936. Here he completed his elementary education, after which he entered Brooklyn Technical High School. Later, after moving to upstate New York, he attended Watertown High School. Another move the following year brought him to North Carolina, where he attended Central High School in Charlotte, from which he graduated in 1954, receiving the Bausch and Lomb Science Medal.

In the following years, the author attended East Carolina College in Greenville, North Carolina, and Brooklyn College in Brooklyn, New York. In January of 1960, he received the Bachelor of Science degree from Brooklyn College, graduating cum laude with honors in physics.

Before entering graduate school, the author was employed as a physicist with the Allis-Chalmers Mfg. Co. in their Atomic Energy Division, in Washington, D.C. In September of 1960, he entered the University of Maryland where he held a teaching assistantship in physics. After receiving the Master of Science degree in 1965, he jointed the staff of the U.S. National Environmental Satellite Center in Suitland, Maryland, where he was employed originally as a physicist and later as a meteorologist. During this period, he published three papers: "Matrix Methods in Multiple Scattering Problems" and "Light Scattering by Cloud Layers" (with S. Twomey and H. B. Howell), and "On Cloud Top Determination from Gemini-V" (with F. Saiedy and D. Q. Wark). All of these publications appeared in the Journal of Atmospheric Sciences.

In 1967, the author was sent under the auspices of the United States Government to pursue a full course of study at the Massachusetts

Institute of Technology in Cambridge, Massachusetts. While at the Institute he was elected to a full membership in the Society of the Sigma Xi. In the natural course of events, he met the former Barbara Esterman, whom he married in 1968.

At the completion of his doctoral thesis, the author returned to his research activities at the National Environmental Satellite Center.

ACKNOWLEDGMENT

The author wishes to express his sincere appreciation to Professor Henry G. Houghton for the guidance and valuable suggestions and discussions received during the preparation of this thesis.

Appreciation is also expressed to Dr. William Smith of the National Environmental Satellite Center of the Environmental Science Services Administration (ESSA) for permission to use his figures and computer programs concerning the SIRS-A data, to Dr. Helmut Weickmann of the ESSA Research Laboratories in Boulder, Colorado, for permission to use his excellent photographs of ice crystals and to Thomas Mee of Mee Industries, Inc., for the use of his photograph of ice crystals.

The author also is grateful to Miss Betty Mengel, who helped in the preparation of the computer programs and to Leonard Hatton, who drafted the figures. Mrs. Martha Young is commended for her care and attention to detail in typing the manuscript and early drafts.

A special acknowledgment goes to the author's wife, Barbara, whose encouragement and understanding during the preparation of the thesis are greatly appreciated.

TABLE OF CONTENTS

CHAPTER ONE

INTRODUCTION

A. The Problem

The development of meteorological satellites has brought with it a renewed interest in the radiative processes at work within our atmosphere. The utilization of the satellites to measure the radiation field reflected or emitted from the atmosphere below has made it possible to infer many of the physical properties of the atmosphere such as its temperature structure, the amount of water vapor, ozone and liquid water present and the heights of cloud layers, to name just a few. However, this can be achieved only after there is a thorough understanding of the way that the radiation field is influenced by the various atmospheric parameters. In practice, equations are formulated which relate the parameters to predicted values of the radiation emitted or reflected. To deduce the values of the atmospheric parameters from actual radiation measurements; one must then "invert" the equations; that is, find what values the parameters must take in order for the predictions to coincide with the measurements. An example where this has been successfully demonstrated is the deduction of vertical temperature profiles of the atmosphere from measurements in eight specially chosen spectral intervals in and near the 15 μm CO_2 band. A large effort is also being directed to develop means of deriving the concentrations of the various atmospheric constituents from measurements of the radiation.

In all of these studies, however, a number of assumptions are made, often with respect to the influence that clouds have on the eventual radiation received by the satellite. While it seems quite reasonable to treat low and middle clouds as black or nearly blackbodies in the infrared,

as most investigators do, the same cannot be said of cirrus layers. Due to the lack of adequate knowledge of the radiative properties of cirrus clouds, a number of very weak assumptions are put forth which could have profound affects on the results obtained. It is to this very problem that the bulk of this research is devoted.

The problem, therefore, is to determine how the various physical characteristics of cirrus clouds (ice particle size and concentration, geometric thickness of the layer, temperature variation, etc.) influence the radiation emitted to space. Once this is achieved, the possibility of determining some of the physical parameters themselves from actual radiation data (inverse problem) will be investigated. Estimates of the cloud parameters from the satellite data can then be used in an attempt to answer such questions as the degree to which cirrus acts like a blackbody in the infrared and the effect that thin invisible cirrus layers have on terrestrial radiation.

B. Review of Previous Work

Theoretical - One of the earliest theoretical investigations into the transfer of radiation through a gas cloud was that conducted by Schuster (1905). By treating the radiation field as consisting of two oppositely directed streams he was able to take account of the emission, absorption and scattering processes within a cloud in an attempt to explain the conditions under which one would obtain "bright line" or "dark line" spectra from a radiating mass of gas. Although this approximation may be fairly reasonable when considering a diffuse radiation field in a weakly absorbing medium, it is not expected to work well when the radiation is peaked in a particular direction; because then the angular effects become

important. Near the tops of clouds, for example, the radiation from the sun would not be well approximated by this method while in the interior it should be a good approximation to the upward and downward fluxes.

Following the early work of Schuster there have been a number of investigators of similar problems, all of whom made use of the two streams approximation in modified form. One of these, Mecke (1921), was the first one who treated water drops as the particles which absorbed and scattered radiation in terrestrial clouds. Some of the others were Dietzius (1922), Albrecht (1933), Hulbert (1943) and Hewson (1943).

Another method used to approximate the scattering of solar radiation was the diffusion approximation developed by Fritz (1953). In this method the radiation is divided into three categories: (a) direct sunlight, (b) light scattered at an angle less than 60° from the direction of incidence, and (c) diffuse scattered light which is assumed to be isotropically distributed. The intensity of the light in (b) was assumed to be described by the Wiener function (1907). The basic idea of the method was to follow the direct and forward scattered beams, (a) and (b), down through the cloud and to compute the diffuse energy generated by them. Using this as a source, the diffusion equation was applied to describe the diffuse radiation field. As a result, the albedo was obtained as a function of cloud thickness, liquid water content and solar zenith angle.

Although these two previous methods yield albedos and diffuse transmissivities that are generally consistent with the few observations, they do not present any information pertaining to the angular distribution of the emerging radiation.

The method of discrete ordinates applied to the complete equation of radiative transfer yields approximate solutions which contain such angular

distributions. All angular integrals are replaced by sums according to the Gauss quadrature formula which leads to a set of simultaneous equations, the number of which depends upon the number of directions to be considered.

While this method seems quite adequate if only a single case is studied it is too time-consuming even for a large computer when many computations are required. One may want to study the changes that would occur in the radiation field if the thickness, liquid water content, or the drop size distribution were varied.

Recently, Yamamoto (1966) has attempted to take scattering into account in the 8-12 μm region of the spectrum by calculating the first few orders of the multiple scattering. Hall (1968), working in the same spectral region, used only single scattering for thin cirrus clouds. However, thicker cirrus clouds would require additional orders of scattering. While this technique is much faster than those discussed above it is not as useful in the visible portion of the spectrum where very high orders of multiple scattering are involved. As a result, the time needed to compute all the orders is prohibitive. Also, the analytical forms become very complex.

Another method which is becoming increasing popular is the Monte Carlo method. This method consists of following the paths of many hypothetical photons in their travels through a cloud layer, the path being determined by a random number selection. The angular scattering distribution from a small volume element (phase function) along with the scattering and absorption coefficients are converted into probabilities. The probability of an outcome is then made proportional to the size of an interval of numbers. In other words, the more numbers assigned, the greater is the probability. One randomly selected number might indicate the distance a

photon will travel before being scattered, another into what direction it will be scattered, and another if it will be absorbed. The photon is followed until it is either lost by absorption or is scattered out of the layer (reflection or transmission). The direction of emergence is then recorded. When a sufficiently large number of such photons are followed a steady nearly continuous distribution of the number of emerging photons as a function of the emerging angle is observed. This constitutes the solution of the problem. While photons are followed many other quantities may be recorded, if desired, such as the total number of scattering events, path lengths, etc. Plass (1968) has successfully used such a program. While it has the virtue that one can vary the physical parameters describing the scattering and absorption, the time for such computations can be very long, especially for thick layers where many multiple scatterings of the photons take place.

What is therefore needed is a reasonably fast method which is capable of computing the angular distribution of radiation where the physical parameters that enter can be conveniently varied. Such a method has been found and will be discussed after we consider the experimental work that has been done up to date on these problems.

Experimental - The first cloud albedo measurements were made by Aldrich (1919) from a balloon overlooking stratus clouds, obtaining a value of 78%, regardless of the cloud thickness or solar zenith angle. Luckiesh (1919) made similar measurements from an airplane over cumulus clouds and found, in contradiction to the work of Aldrich, that the mean albedo varied with the cloud thickness.

Nothing more was done along these lines until Neiburger (1949) made detailed measurements using two pyreheiliometers mounted on a blimp. In

this way he was able to measure the ascending and descending radiation beneath, in, and above California stratus, while simultaneously sampling the drop size and liquid water content. The means of the albedos derived from this data were fairly consistent with the predictions from the two streams model. Similarly, Cheltsov' (1962), using two Yanishevskii pyranometers studied the radiation field for various stratified clouds obtaining the variation of albedo with thickness for each type of cloud observed.

More recently, satellite data have been utilized in order to obtain the angular distributions of solar radiation reflected from clouds. One such study was made at the National Environmental Satellite Center by Ruff et al. (1967) from TIROS radiometer measurements.

When dealing with cirrus clouds we must concern ourselves with the fact that the clouds are composed of ice crystals rather than liquid water drops. MacDonald and Delterne (1963) conducted measurements on the infrared and visible reflection properties of cirrus ice clouds formed at Yellowstone National Park. They claimed that winter ice fogs which are formed here are very nearly identical to natural high altitude cirrus in regard to the ice particles present. As a result of their measurements, no noticeable difference in the reflectivity of water or ice fogs was observed.

Most of the experimental work discussed above is concerned with the radiative effects in the visible region of the spectrum. Shaw and Gates (1960), however, conducted measurements of the transmission of infrared radiation by comparing the intensity of the direct solar beam after its passage through clouds with the direct solar beam through the clear sky. The results reported were for various cloud types and selected wavelengths in the region .48 to 12.0 μm. However, it is not clear why they were able

to neglect the self-emission by the clouds, for surely such radiation would also reach the detector. If this is so, then the values reported are not necessarily true transmittances, particularly for those wavelengths in which emission is strong.

In 1963, Kuhn was able to estimate the long-wave emissivity of clouds by using observations of the upward and downward fluxes provided by the radiometersonde in conjunction with actual aircraft observations of the bases and tops of the clouds. As a result, the effective long-wave emissivity, that he defined as one minus the slab transmissivity, was obtained for clouds of various heights. Based on 55 measurements, he showed cirrus emissivity to range from .10 to .75. More recent radiometric measurements of cirrus were conducted by Kuhn and Weickmann (1969) for the wavelength region 8-13 μm. Transmissivities varied from 95% for high, thin cirrus to 53% for 5 km thick cirrus.

Valovcin (1968) made infrared measurements (8-13 μm) of jetstream cirrus, while flying in a U-2 aircraft, above, in, and beneath the cirrus, simultaneously recording the ambient temperature. As a result of such measurements, an effective cirrus emission-transmission coefficient was obtained as a function of cloud depth for different cirrus clouds. However, the coefficient, defined as the value by which the effective blackbody temperature (radiometric temperature) must be multiplied to obtain the ambient temperature, differs from the emissivity definitions discussed by other researchers. A number of other possible definitions can be found in the work of Rodgers (1967). Therefore, one must be very careful in accepting at face value the reported emissivities of clouds. The definitions are usually tailored to the particular problem in which

the individual researcher is engaged. The method of computation that is employed in this research makes use of the concept of emissivity only for thin "isothermal" layers and avoids such use when describing the radiative properties of the entire cloud.

C. Method of Attack

The method which is employed to obtain the solution of the radiative transfer in the cloud layers is one originally devised by van de Hulst (1963) and applied in modified form by Twomey, et al. (1966) for problems of the scattering of solar radiation in clouds. However, it is also readily applicable to the case where the cloud is a thermal emitter as well as a scatterer of external radiation.

In this method, the multiple scattering of a continuous field of radiation is approximated by the scattering of discrete streams of radiation, the scattering process being imagined as a redistribution of energy among the streams. The diffuse reflectance and transmittance and direct transmittance of radiation in the cloud layers are described by the matrices S, T, and E, respectively. For example, S_{ij} refers to the radiation which is reflected into the i-direction due to a unit flux incident upon the layer from the j-direction. The matrices T and E have similar explanations. Matrix solutions corresponding to a layer of thickness $(\tau_1 + \tau_2)$ are related by reasonably simple matrix equations to the matrix solutions corresponding to layers of thicknesses τ_1 and τ_2. Therefore, once the solutions for two layers are known, the solution for the layer composed of the sum of the original two layers can easily be found. Solutions for thicker layers can be determined by a continuous

application of this procedure. In practice, one begins with two identical sublayers which are so thin that the scattering and emission solutions are closely approximated by single scattering theory. From this, the solutions for the thicker layers are generated.

D. Choice of Wavelength for Study

The wavelengths which were chosen for study are in the 11-15 μm and the 0.4-0.7 μm (visible) portions of the spectrum. From the 11-15 μm region, four special wavelengths (11.12, 13.33, 1400, and 14.16 μm) were chosen, each of which coincides with the centers of the bands of four of the channels of the SIRS A instrument aboard the Nimbus III spacecraft. The reasons for these choices were:(1) observational data were readily available and could be used in helping to show the validity of the theoretical computations, (2) the bandwidths of the SIRS A channels were narrow so that theoretical computations needed to be performed only at a single wavelength of each channel and (3) strong interest was shown by other investigators in a cirrus cloud radiation study at the SIRS A wavelengths.

While actual results were obtained for the wavelengths mentioned above, the analyses that follow can be applied to many other regions of the spectrum.

CHAPTER TWO

THE COMPOSITION OF CIRRUS CLOUDS

A. Classification of Cirrus Types

Cirrus clouds (more accurately called cirriform type clouds) are generally classified into the three broad types, cirrus (ci), cirrostratus (cs), and cirrocumulus (cc). Cirrus, which is found at the greatest altitudes, have a typical fibrous structure that is threadlike in appearance and is often composed of detached elements that are arranged in the sky in an irregular manner, without any connection with cirrostratus. These are known as fair-weather cirrus. If the cirrus are arranged in bands or connected with cirrostratus, they usually indicate that bad weather may be on the way. Cirrostratus, in comparison, are composed of thin whitish sheets of clouds that resemble a fibrous veil covering the entire sky. The third type, cirrocumulus, usually consists of regular arrays of small white flakes of cloud that develop from cirrostratus. All three of these basic types of cirriform clouds are found to exist in a variety of forms and are given a host of names to describe their structure, color, and shape.

B. Climatology of Cirrus

Extensive measurements of cirrus clouds have never been made on the same scale as those for middle and lower clouds. Nevertheless from the few measurements that are published, we can obtain some idea of the heights and thicknesses of cirrus clouds as well as the temperatures of their bases and tops. Figure 2.1 presents a summary of some of these measurements which were taken over the United States, Germany, and Great Britain. The measurements over the United States

were collected by Fletcher and Sartor (1952); those over Germany by Weickmann (1949); and those over Great Britain by Murgatroyd and Goldsmith (1953).

Upon inspection of the distribution of the heights of cirrus bases it is evident that they are generally restricted to the interval between 20 and 40 thousand feet and are most often found between 25 and 30 thousand feet.

The data show that the thickness of cirrus may range from very thin layers to clouds 15 to 20 thousand feet thick. While the flights over Great Britain show a most frequent thickness of 5 to 6 thousand feet, those over Germany and the United States show a greater frequency of thinner layers.

The most frequent base temperatures found over Europe lie between -35°C and -45°C, but over the United States these temperatures tend to be much higher. However, the observations show a very broad range of base temperatures extending from -10°C to -62°C. The temperatures of the cloud tops also have a broad range with a maximum frequency at temperatures of -45°C to -60°C.

C. Form, Size and Orientation of the Ice Crystals

There are a number of ways of obtaining information of the form and size of the ice crystals that are present in cirrus clouds. One can directly sample the clouds, make deductions from visual optical phenomena, or make laboratory measurements of a simulated cirrus cloud.

In directly sampling the clouds from an airplane, a number of difficulties are encountered. Due to the high speeds involved, it becomes a difficult matter to avoid shattering of the ice crystals during

their collection. Although this problem has been partially solved by using sampling tubes in which crystal-laden air is decelerated before reaching the detector, large delicate crystals will still undergo fracture.

The most extensive collection of ice crystals has been obtained by Weickmann (1945, 1947) while flying in a specially instrumented aircraft at various elevations in the troposphere up to the cirrus levels. At each of the elevations that was sampled, the temperature was simultaneously recorded. Figures 2.3 to 2.5 show sample micrographs of some of the crystals that he found along with the temperatures of the sampled environment. These observations show that columnar crystals are predominant in cirrus clouds. In cirrostratus clouds, it was found that a single more or less completely formed column was the predominant cyrstal form, whereas in cirrocumulus, clusters of incompletely formed columns dominated. It was generally observed that cirrostratus crystals have a length of approximately 100 μm and a width of approximately 40 μm, the exact dimensions varying with the temperature, duration of supersaturation, and concentration. The length of one component of the clusters in cirrocumulus is on the average about 200 to 300 μm and the width is about 50 to 100 μm. Weickmann further estimated that the water content in cirrus clouds is of the order of 0.01 g/m^3.

The Japanese physicist Ukichiro Nakaya devoted many years to the study of snow and ice crystals. His now famous book, Snow Crystals: Natural and Artificial (1954), contains numerous photomicrographs of natural snow and ice crystals collected at the surface as well as those artificially grown in the laboratory.

From the sizes of the images shown on the micrographs and the magnification given for each one, it is a simple matter to obtain the original dimensions of the crystals. In this manner, the lengths of the major and minor axes of 17 columnar type crystals were obtained. Results of these determinations are shown in figure 2.2 where the length of the major axes for each crystal is plotted against the length of its minor axis. However, the sizes of these 17 crystals may not be too representative of the actual sizes of cirrus crystals for two basic reasons. One of these is the fact that larger crystals more often reach the surface than smaller crystals (heavier crystals have a greater chance of precipitating out of the cloud). The other reason is that many of the crystals may have fallen from regions lower than cirrus levels, such as from cumulus tops, where the crystals tend to be larger than those from cirrus levels. This latter effect will be discussed shortly in connection with the sampling of crystals at various altitudes. Probably more significant than the sizes of these 17 crystals are the ratios of the lengths of their major and minor axes, which results in a mean value of 3.49 with a standard deviation of 1.82.

More recently there has been developed a Continuous Particle Sampler which can operate in airplanes having speeds up to Mach 0.8 and altitudes to 40,000 feet. The sampler, which makes Formvar replicas of the ice crystals collected, provides a permanent record for future analysis. Figure 2.6 shows a photograph of some of the samples collected by the sampler aboard an X-21A Laminar Flow Control Aircraft (Mee and Williamson, 1965).

The sampler has also been employed by Mossop and Ono (1969) on flights over New South Wales in an attempt to measure ice crystal

concentration in clouds as well as in determining the shape and riming characteristics of natural ice crystals (Ono, 1969). Besides using the sampler, Mossop and Ono used an aluminum foil impactor as well as two different deceleration tubes. Results of their measurements of "cold-region" columns are reproduced in figure 2.7 in which the lengths of the major and minor axes of the crystals are plotted, along with an approximate mean curve and boundary limits. The "cold-region" columns were chosen from their measurements because the average temperature of the sampled region was approximately -32°C which falls within the observed temperature range of cirrus clouds.

On the basis of this data, a histogram of the ratio of the length of the major to that of the minor axis was drawn and is shown in figure 2.8. The mean ratio which is approximately 2.30 with a standard deviation of 0.87, is fairly consistent with the averages of the lengths of the major and minor axes which were 147 μm and 61 μm, respectively.

The warm region columns that Ono sampled at an average ambient temperature of -2°C have approximately the same range in the length of their minor axis as that for cold region columns. However, while the lengths of the major axis of the cold region columns reach at most to about 300 μm, those of warm region columns can reach to 600 μm. On the basis of this evidence, one would have to conclude that the axial ratios determined from Nakaya's micrographs are probably too high for cirrus crystals; the value of 2.30 is considered to be more realistic.

In summary, figure 2.9 presents a comparison of the dimensions of the crystals collected by Nakaya, Weickmann and Ono. In the upper portion of the graph, the ranges in length of the major axes of the crystals

are compared while in the lower portion of the graph, the ranges in length of the minor axes are compared. A solid bar indicates the mean of the observed lengths in the range shown.

It is fairly obvious from these comparisons that the crystals collected by Nakaya have dimensions that are many times greater than those collected by either Weickmann or Ono. For the reasons discussed above they do not appear to be too representative of cirrus crystals. The dimensions of the crystals collected by Weickmann compare fairly well with those collected by Ono. Since Weickmann's crystals were collected in cirrus clouds and Ono's were collected in temperature regions fairly typical of cirrus levels, the dimensions shown for their collections will be considered indicative of the true dimensions of cirrus crystals. In future computations it will be assumed that cirrus crystals have major axes that range in length from 100 to 300 μm with a mean value of about 150 μm and minor axes that range in length from 40 to 100 μm with a mean value of about 60 μm.

The deduction of crystal shapes and orientations from the visual optical phenomena they produce enables us to obtain much useful information about the ice crystals found in cirrus clouds. By noting the particular optical phenomenon present, one can determine the shape and orientation of the crystals that caused it by utilizing optical theory. For example, clouds containing ice crystals often show a halo of 22° around the sun or moon. It can be shown (Humphreys, 1964) that this phenomenon could only be caused by refraction within ice crystals when light enters and leaves the crystal from faces that form a diehedral angle of 60°. This will be the case when hexagonal ice columns orient themselves so that their long axes are parallel to the

ground. Then light will enter and leave alternate faces of the crystal which form an angle of 60°. Although the long axes lie in the horizontal plane, the crystals are still free to orient themselves in any direction within this plane. The fact that the halo appears to be uniformly bright is evidence that such orientations in the plane are random.

If the crystals consist of small hexagonal plates that are not too small, they tend to fall with the planes of the crystals nearly horizontal. If one were to then look down at a cloud of such crystals, one would see a bright spot in the cloud at a distance below the horizon equal to the height of the sun above the horizon (sub-sun, mock-sun, or undersun). Due to the slight tilting of the crystals from the horizontal and the multiple reflections involving two or more crystals, the spot of light is often drawn out into a vertical column which may extend both above and below the horizon and even above the sun itself (sun pillar).

Another phenomenon that could be caused by such plate crystals is the appearance of bright spots called sun dogs on either side of the sun when the sun is on the horizon. For clouds of such crystals near the horizon, the geometry would be nearly identical to that discussed above for the halo of 22°. Since it would be impossible to see the rays of the sun deviated by clouds above the horizon we would only see the two spots. Sun dogs could also be caused by columnar ice crystals if their long axes were nearly aligned with the vertical. However, this is an unstable mode of fall for such crystals so that the sun dogs would be predominantly caused by hexagonal plates.

The halo of 46° is produced by prisms whose refracting faces form an angle of 90°. Either plane crystals falling with their planes horizontal or columnar crystals falls with their long axes vertical will

produce such a halo. However, as mentioned above, such vertically oriented columnar crystals are not too common. The fact that this halo is not too commonly observed must then be explained by the fact that plate crystals are less numerous than columnar crystals which is consistent with the findings from direct sampling of the clouds.

In practice, only a small proportion of cirrus produce halos, most of which occur in clouds of freshly formed prismatic crystals, in not too thick cirrostratus veils. Pillars are typical in the ice mists and cirrus hazes of polar regions (Stone, 1957).

In 1962, McDonald and Delterne conducted an experiment in Yellowstone National Park where it was reported that the winter ice fogs that developed in the geyser basins were identical to natural high altitude cirrus. Taking advantage of this situation, they studied the ice crystal shapes and sizes composing the fog by making use of the replica method developed by Schaefer.. They reported that the ice crystals they observed were textbook examples of cirrus crystals, similar to the photomicrographs taken by Schaefer (1962) at Yellowstone a short time before.

However, a comparison of Schaefer's micrographs with those taken by Weickmann (1945) in actual cirrus show some strong differences. Schaefer's micrographs show numerous spherical or nearly spherical frozen drops that are much smaller on the average than the ice crystals observed in cirrus clouds. It is therefore not clear what was the basis for concluding that the ice fogs were identical to cirrus. After all, the environmental conditions are quite different. In a cirrus cloud, ice crystals have a longer time to grow and develop and their concentrations are quite different than those of the frozen drops and crystals found in the ice fogs. Despite these shortcomings the experiment does show fairly well

how optical phenomena are related to crystal shape. Table 2.1 is a summary of their findings which relates the crystal type and size observed to the ambient temperature and optical phenomenon present.

While a great deal of information has come from measurements either direct or indirect of actual cirrus clouds, much has come from laboratory studies. Some of these studies have taken the form of experiments in controlled environment chambers which simulated the conditions of temperature and humidity found in cirrus. Others have been involved in studying the behavior of freely falling objects of various sizes and shapes in order to ascertain the effect that hydrodynamic drag has upon the orientation that the crystals take.

One of the best known experiments on ice crystal growth were those of Nakaya (1936, 1951, 1954) previously referred to, who suspended growing ice crystals upon a fine filament in a cylindrical cold chamber in which a fog was produced. The rising fog was supercooled before reaching the crystals, which permitted the crystals to grow in an environment that was near water saturation. In this manner the growth habit of the ice crystals were studied as a function of the physical conditions present.

Following these earlier investigations Kampe and Weickmann (1951) performed experiments in a cold chamber (10 ft. x 10 ft. x 8 ft.) in which a supercooled fog could be produced by the introduction of steam. The chamber could be cooled to any desired temperature down to -45°C. After a stable supercooled fog of constant temperature had been obtained, it was seeded. Samples of the ice crystals that were produced in the

TABLE 2.1

CLOUD CRYSTAL SUMMARY

(from McDonald and Delterne, 1963)

Date	Time	Temp. °C	Crystal type	Size (microns)	Conc. #/cc	Comments
30 Jan.	0730	-16.5				
	0800	-14	Plates	120-180	0.5/cc	Crystals show considerable internal structure. Undersun and sun pillars in evidence.
	0900	-12	Plates	200X40	1/cc	Crystals still showing good internal structure. Undersun and sun dogs.
	1000	-8	Plates	200	Very low	Too warm for effective seeding.
31 Jan.	0730	-16				
	0830	-14				
	0900	-12	Plates	200-400	2/cc	Plates and prisms occurring in about equal numbers. Plates with internal structure, prisms with deep cavities. Halo of 22° with bright sun dogs.
	0930	-9.5	Prisms	90X60	2-3/cc	Prisms in excess of plates now, about 3 to 1. Marked cavities in prisms, good structure in plates. 22° and 46° haloes, sun dogs, circumzenithal arc.
	0945		Prisms	150X50	1/cc	All prisms now, showing deep cavities. Magnificent halo phenomena: 46° halo, circumscribed halo appearing as ox yoke, lower tangential arc to 46° halo.
	1000	-8	Prisms	90X45	Very low	Too warm, stopped generators.
1 Feb.	0730	-15.5				
	0800	-14	Plates	150	1-3/cc	Undersun.
	0900	-10	Plates	150	1-3/cc	2/1 plates to prisms. 22° halo, pillars, ox yoke.
	0930		Prisms	140X40		Too warm for seeding.

TABLE 2.1 (Continued)

Date	Time	Temp. °C	Crystal type	Size (microns)	Conc. #/cc	Comments
3 Feb.	0730	-11	Plates	120X30	1-2/cc	Brilliant undersun. Good structure on crystals.
	0830	-9	Plates Prisms	150 90X40	2/cc	Prisms beginning to show. Plates show good structure, prisms show cavities. 22° halo, pillars, sun dogs, faint circumzenithal ace.
3 Feb.	0900	-9	Plates Prisms	100-200 100X50	2-3/cc	Prism and plates in a ratio of 1 to 1. Plates show some structure, prisms appear as columns with some cavity development. Halo phenomena are fantastic. Very bright, everything in the book, including 180° pillar.
	0930	-6	Prisms Plates	150X50 200	1/cc	Predominantly prisms showing cavities, but plates are quite plain now. Concentrations dropping.
	1000	-4	Prisms	200X70	0.5/cc	Prisms show skeletal structure. Halo of 22°. Too warm for effective seeding.
5 Feb.	0730	-15.5				
	0800	-12	Plates	100-200	2/cc	Little internal structure. Sun pillars and undersun.
	0830		Plates	225X30	2/cc	Plates showing more structure now.
	0900		Plates	100-150	2-3/cc	Some clumping of crystals. Halo of 22°, faint sun dogs, faint circumzenithal arc.
	0915		Plates	200-300	1/cc	Plates show some structure. Optical phenomena dimning.
	0945	-8	Plates	200-300	1/10 cc	Lots of structure on plates. Counts dropping way down. Faint circumzenithal arc.

TABLE 2.1 (Continued)

Date	Time	Temp. °C	Crystal type	Size (microns)	Conc. #/cc	Comments
27 Feb.	0730	-43				
	0800	-40				
	0815		Prisms	100X50	0.5/cc	Best day. Prisms show cavity development.
	0830		Prisms	100X50	0.5/cc	Sun dogs showing now.
	0900	-32	Prisms	100X50	0.5/cc	Some conglomerates showing. Sun dogs, faint 22° halo.
	0930	-27				
	1000		Prisms	70X30	0.6/cc	Halo 22°; sun dogs becoming faint. Low humidities leading to rapid dissipation of fog.

presence of a supercooled cloud were then collected on glass plates and immediately photographed under a microscope. Just before seeding, the temperature was carefully measured.

Figures 2.10 to 2.14 show some of the ice crystals they grew at water saturation. They show that at first clear single plates are formed down to about -4°C with a sudden change to short prisms, twin prisms and hollow twin crystals. Then, around -9°C, the shape is again back to plates, but this time double plates are present and plates with ribs and internal structure, characteristic of dendritic stellar forms. Such two-dimensional dendritic forms appear at about -13°C. At -20°C, three-dimensional aggregates of plates first occur. Also at these temperatures, columns appear, the size of which decreases with decreasing temperature.

Kampe and Weickmann also made observations of the visual optical phenomena produced by the shining of a lantern-slide projector on the supercooled fog. The 22° halo, the sun pillar, sun dogs, and the upper and lower tangent arcs of the 22° halo were seen. However, the sun pillars were the most frequently observed optical phenomena occurring in the presence of both plates and prism crystals. Observations of the halos confirm the crystal forms that were seen.

Jayaweera and Mason (1965) studied the behavior of freely falling cylinders, cones, and loaded cylinders and disks in viscous fluids in order to gain an understanding of the terminal velocities, drag coefficients, and orientations that are possible with actual ice crystals in natural clouds. Their measurements covered the range of Reynolds numbers, Re, from 10^{-2} to 10^{3}.

They found that with $Re < 10^{-2}$ cylinders showed no preferred orientation but for $10^{-2} < Re < 10^{-1}$, they were oriented to offer maximum resistance to the motion. If the ratio of diameter to length d/L is greater than unity, they fall with their short axis vertical and those with d/L less than unity fall with their long axis horizontal. At $Re < 50$, the cylinders fall stably, but at higher Re, short cylinders flutter as they fall.

An order of magnitude estimate of the Reynolds number associated with ice crystals at cirrus levels may be obtained using Jayaweera and Mason's experimentally determined values of the drag coefficient versus Reynolds number for long cylinders. For a cylinder falling with its long axis horizontal, the terminal velocity, V_o, that results from equating the net weight of the cylinder to the drag forces is given by

$$V_o = \left[\frac{\pi}{2} \frac{d}{C} \left(\frac{\rho_i - \rho_a}{\rho_a} \right) g \right]^{\frac{1}{2}} \qquad (2\text{-}1)$$

where d is the diameter of the cylinder, C is the drag coefficient and ρ_i and ρ_a are respectively the densities of the ice and of the surrounding air. Since $\rho_a \ll \rho_i$ at cirrus levels, ρ_a may be neglected in the numerator of the expression in brackets in equation (2-1).

The Reynolds number for a cylinder is defined by the expression

$$Re = \frac{V_o d}{\nu} \qquad (2\text{-}2)$$

where υ is the kinetic viscosity of the air. As a result of combining equations (2-1) and (2-2) the Reynolds number may be written

$$Re = \left[\frac{\pi \rho_i g d^3}{\rho_a \nu^2 C} \right]^{\frac{1}{2}} \qquad (2\text{-}3)$$

Upon substitution of the values for the parameters ρ_i, ρ_a, and υ appropriate to cirrus levels as given in the Handbook of Geophysics (1960) and a value for the diameter, d, an expression for the Reynolds number versus the unknown drag coefficient, C, results. The drag coefficient may be approximated by making an initial guess at the value of Re and obtaining the value of C corresponding to the initial guess from the graphs of drag coefficient versus Reynolds number given by Jayaweera and Mason (1965). This can then be used in equation (2-3) to compute a second approximation to the value of Re which in turn will yield a second approximation to C. This procedure can be continued until the values of Re and C converge to a single pair of values. Such a procedure was performed, which converged fairly well. To test the values obtained, the entire procedure was repeated using a different initial guess of Re. The results were the same.

Table 2.2 summarizes these results for 3 different elevations at cirrus levels, and for 3 different cylindrical diameters. On the basis of these computations, it appears thatcirrus crystals have Reynolds numbers that are generally between the values of 0.1 and 10, and thus tend to fall stably. This means that hexagonal prisms will fall with their long axes parallel to the ground which is consistent with the formation of halos previously discussed.

Jayaweera and Mason also made studies of the influence of captured droplets on the falling motion of needles and columns. They observed that when the ratio of the weight of a captured sphere to that of the capturing cylinder was small, the cylinder will tend to fall with its

TABLE 2.2

SUMMARY OF COMPUTED ESTIMATES OF REYNOLDS NUMBERS

Altitude (km)	ρ_a (g cm^{-3})	υ (cm^2 sec^{-1})	d (μm)	C	Re
7	5.90×10^{-4}	2.60×10^{-1}	40	19.5	0.48
9	4.67×10^{-4}	3.20×10^{-1}	40	20.0	0.43
11	3.65×10^{-4}	3.90×10^{-1}	40	22.0	0.38
7	5.90×10^{-4}	2.60×10^{-1}	70	8.0	1.74
9	4.67×10^{-4}	3.20×10^{-1}	70	8.2	1.57
11	3.65×10^{-4}	3.90×10^{-1}	70	9.3	1.37
7	5.90×10^{-4}	2.60×10^{-1}	100	5.3	3.65
9	4.67×10^{-4}	3.20×10^{-1}	100	5.7	3.20
11	3.65×10^{-4}	3.90×10^{-1}	100	6.0	2.90

long axis horizontal, while if the ratio is large, the cylinder will fall with its long axis vertical. For intermediate ratios, the axis of the cylinder will tend to be inclined to the horizontal.

Another interesting experiment that they conducted was to study the falling behavior of perspex cylinders capped at each end by perspex disks with the hope of inferring something about the behavior of ice prisms capped by hexagonal plates. By dropping the capped cylinders into a tank of water, it was observed that the cylinders fell with their unique axis horizontal if the cylinder length exceeded a certain critical value, while short cylinders tended to fall with their unique axis vertical. Cylinders that were released with their unique axis vertical tended to maintain the orientation, regardless of their length. It was their conclusion that many of the capped ice columns observed in nature could fall with their column axis vertical. This orientation would give rise to the 46° halo previously discussed.

The last experiment that will be mentioned concerning the orientations of falling bodies is their experiment on clusters of falling disks. They observed that a cluster of three equal disks will tend to fall in a butterfly arrangement; that is, one member will be horizontal while the other two will form a symmetrical "vee" with it. It was observed that such a cluster is very stable when the smaller included angle between the disks is less than 30°. Only at high Reynolds numbers do the clusters break up because of the highly turbulent nature of the flow.

One can therefore see from these experiments that hydrodynamically speaking single isolated ice columns tend to fall with their long axes

parallel to the ground. However, other influences are at work such as drop capture, capping of columns, etc. that tend to disturb the horizontal stability of the column.

On the basis of all of the evidence discussed above, we must conclude that cirrus crystals are predominately composed of hexagonal columns whose axes are randomly oriented in the horizontal plane; the degree to which they are randomly oriented with the vertical is not known, though there is the greater tendency toward a more horizontal orientation of the axes. In the computations that follow it will be assumed that the ice crystals are composed of hexagonal columns with their long axis lying at random in a horizontal plane. We shall see later on that this restriction upon the orientation of the crystals may be lifted and that to a sufficient approximation the crystals may be treated as randomly oriented in three dimensions.

Table 2.3 summarizes all the assumptions that have been made regarding the crystal size, shape, and orientation in space.

TABLE 2.3

PHYSICAL CHARACTERISTICS ASSUMED FOR CIRRUS ICE CRYSTALS

Shape	Predominantly hexagonal columns
Size	Major axis - 100 to 300 μm, mean = 150 μm Minor axis - 40 to 100 μm, mean = 60 μm
Orientation	Long axis random in horizontal plane

CHAPTER THREE

ANGULAR SCATTERING PATTERNS FROM INDIVIDUAL CRYSTALS

A. Nature of the Scattering Patterns

Before proceeding to a computation of the transfer of radiation in clouds containing ice crystals, the angular distribution of the radiation they scatter as well as the scattering and absorption coefficients must be determined. While the scattering from spheres can be treated exactly by applying the results of the Mie theory (1908), the same cannot be done for the non-spherical ice crystals. Exact solutions for cylinders and spheroids do exist but only for special angles of incidence.

In order to gain insight into the nature of the scattering that might result from ice crystals, an estimate will be made of the angular scattering pattern from a model distribution of simple-shaped, but non-spherical crystals. This will then be compared with the angular scattering pattern computed for spheres whose size is such as to scatter and absorb out of an incident beam as much energy as would be scattered and absorbed by the model crystals.

The model which will be used for this estimate is one consisting of circular cylinders whose lengths are several times their diameters and whose orientations in space are random. Such cylinders were chosen because of their similarity to some of the columnar ice crystals that actually occur.

Hodkinson (1963) has shown that for a distribution of spheres whose diameters are larger than about 2 or 3 wavelengths, the scattering pattern may be conveniently divided into three separate parts. One part is the sharply peaked pattern around the forward direction that is due to

diffraction which may be computed according to the formula derived by Kirchhoff (van de Hulst, 1957, P. 106), the second is the radiation reflected from the surface, and the third part is due to refraction within the crystal.

The computation of the scattering according to this separation approximates the scattering calculated from Mie theory fairly well for scattering angles less than the angular limit for scattering by two refractions,

$$\theta_m = \pi - 2 \sin^{-1}\left(\frac{1}{n}\right) \qquad (3\text{-}1)$$

where n is the index of refraction. For an index n equal to 1.22, this would set the angular limit at 70°. At larger angles, the approximation underestimates the scattering. However, with opaque particles, the approximation does not appear to be too bad even at large angles.

Hodkinson's results further showed that scattering patterns from irregular particles can also be divided into the same three separate parts as long as the particles are large enough to have their extinction efficiency factor (ratio of the sum of the scattering and absorption cross-sections to the geometric cross-section) nearly equal to 2.

For the infrared wavelengths with which we shall be concerned, contributions to the scattering from refraction may be neglected. However, when performing computations in the visible portion of the spectrum where the absorption coefficients may be fairly small, refraction must be included. By simple geometric analyses, which are given in Appendix A, the mean path lengths of radiation through both an infinitely long cylinder and a sphere, $\bar{\ell}_c$ and $\bar{\ell}_s$, respectively, are derived as functions of their respective radii, a_c and a_s, and the index

of refraction, n. For the cylinder, two cases were considered. In the first case, the mean path length was computed for a cylinder whose axis was oriented at a right angle to the incident radiation, while in the second case the mean path length was computed for a distribution of cylinders in random orientation. The results of the analyses are as follows. For the cylinder oriented at right angles to the radiation,

$$\bar{\ell}_c = a_c\left[\frac{\sqrt{n^2-1}}{n} + n \sin^{-1}\left(\frac{1}{n}\right)\right] \tag{3-2}$$

and for the sphere

$$\bar{\ell}_s = \frac{4}{3n} a_s\left[n^3 - (n^2-1)^{\frac{3}{2}}\right] \tag{3-3}$$

Since the solution for the mean path length in the random distribution of cylinders could not be obtained in closed form, the solution in integral form must be numerically evaluated.

$$\bar{\bar{\ell}}_c = \frac{1}{2}\int_0^{\pi} a_c n\left[\frac{\sqrt{n^2-1}}{n^2-\cos^2\gamma} + \frac{1}{\sin\gamma}\sin^{-1}\left(\frac{\sin\gamma}{\sqrt{n^2-\cos^2\gamma}}\right)\right]\sin\gamma\, d\gamma \tag{3-4}$$

If k is the absorption coefficient in the ice, the mean transmissivity after one refraction will be given approximately by $e^{-k\bar{l}_s}$ for the sphere, $e^{-k\bar{l}_c}$ for cylinders oriented at right angles to the radiation, and $e^{-k\bar{\bar{l}}_c}$ for the randomly oriented cylinders.

The variation of such transmissivities with the size of the particle is shown in figure 3.1 for three different wavelengths. As can be observed, the transmissivity through the cylinders or spheres is less than 3% for radii greater than 30μm and less than .5% for the randomly

oriented cylinders. For radii less than 30 μm, the transmissivity curves rise sharply with decreasing radius for the sphere and normally oriented cylinder.

From the considerations of Chapter Two, we have seen that typical columnar type crystals have widths of the order of 40 to 100 μm and lengths from 100 to 300 μm. This roughly corresponds to cylinders of radii 20 to 50 μm. For randomly oriented cylinders in this size range, transmissivity is at most around 1% and generally much less. The equivalent spheres for crystals of this size will generally have radii greater than 35 μm. For such radii, the transmissivities are at most 2%. Even if cavities are present in the crystal, only few crystals will have path lengths sufficiently small to result in an appreciable transmissivity. On this basis refraction will be neglected in the computation of the angular scattering pattern for the infrared wavelengths, taking only diffraction and surface reflection into account.

A further simplification can be made in our comparison of the scattering patterns for ice crystals and spheres. According to the theorem proved by van de Hulst (1957), the reflection pattern from randomly oriented particles is identical to that from spheres of the same material. Therefore, only the diffraction pattern of the model crystals need to be compared with the diffraction pattern of the spheres to see how the total scattering patterns differ.

Before proceeding with these comparisons, it is appropriate to determine how well the diffraction-reflection computation of the scattering pattern approximates the exact pattern. This can be done not only for spheres from the results of the exact Mie theory, but also from

the exact theory for cylinders with normally incident radiation. The results of such a comparison will show how much confidence can be placed in the approximations. The previous analysis only made the approximations seem reasonable.

B. Diffraction-Reflection Approximation Versus the Exact Computation.

When a plane parallel beam of radiation is intercepted by a particle, a hole of the size and shape of the geometrical shadow of the particle is made in the wave front. As a result, the incomplete wave front interferes with itself to produce at large distances the angular intensity pattern known as the Fraunhofer diffraction pattern.

If I_o represents the flux (energy per unit area per unit time), of radiation of wavelength λ incident upon the particle of shadow area G, then the intensity, I, (energy per unit area normal to the beam per unit solid angle per unit time) in the direction having spherical polar angles θ and ϕ at a distance r from the particle is given according to van de Hulst (1957) by the expression (see figure 3.2).

$$I(\theta,\phi) = \frac{G^2}{\lambda^2 r^2} I_o \left| D(\theta,\phi) \right|^2 \qquad (3\text{-}5)$$

where

$$D(\theta,\phi) = \frac{1}{G}\int\int_G e^{-ik(x\cos\phi + y\sin\phi)\sin\theta}\, dx\, dy \qquad (3\text{-}6)$$

k is the wavenumber, $2\pi/\lambda$.

D may be computed for various shaped particles. In the case of symmetrical particles, the integration leads to standard tabulated functions, while for nonsymmetrical particles, the integrations must be performed numerically.

For a sphere of radius a_s,

$$D(\theta) = \frac{2 J_1(k a_s \sin\theta)}{k a_s \sin\theta} \qquad (3\text{-}7)$$

where J_1 is the Bessel function of first order and θ is the angle of scatter.

For a cylinder of radius a_c, length $l \gg a_c$ and inclined to the direction of propagation of the radiation by an angle γ,

$$D(\theta,\phi) = E(k a_c \sin\theta\cos\phi)\, E(\tfrac{1}{2} k l \sin\theta \sin\phi \sin\gamma) \qquad (3\text{-}8)$$

where

$$E(u) = \frac{\sin u}{u} \qquad (3\text{-}9)$$

for any argument u.

A cylinder of infinite length inclined at a right angle to the direction of propagation of the radiation will result in the expression for D obtained by setting $\phi = 0$ in equation (3-8),

$$D(\theta) = E(k a_c \sin\theta) \qquad (3\text{-}10)$$

Here, θ is the angle of scattering. The diffracted ray is restricted to lie in a plane normal to the cylindrical axis. There can be no ϕ dependence for an infinite cylinder.

The reflection from the surface can also be readily obtained. van de Hulst (1957) has shown that for a sphere the reflected intensity is given very closely by,

$$I(\theta) = \frac{I_0 a_s^2}{8 r^2}\left[r_1^2(\theta) + r_2^2(\theta) \right] \qquad (3\text{-}11)$$

where r is the distance from the center of the sphere and $r_1(\theta)$ and $r_2(\theta)$ are the Fresnel reflection coefficients.

A similar expression can be derived for the infinite cylinder and is given in Appendix B. The resulting intensity is

$$I(\theta) = \frac{I_0 a_c}{4r}\left[i_1^2(\theta) + i_2^2(\theta)\right]\sin\frac{\theta}{2} \qquad (3\text{-}12)$$

where a_c is the cylindrical radius and r is the distance from the axis of the cylinder.

On the basis of the above formulae, the scattering patterns for the sphere and the cylinder were computed and compared with the scattering patterns obtained from the exact expressions. Figures 3.3 to 3.8 show these comparisons for spheres and cylinders of radii 25 and 50 μm for the wavelengths 6.7 and 10.5 μm.

Superimposed upon each scattering pattern, a smooth curve has been drawn which passes through points halfway (on a linear scale) between the maxima and minima of the diffraction fringes, excepting the principal maximum where the curve follows fairly close to the original curve. These curves more closely approximate the scattering patterns that would result for a size distribution of particles since such a distribution would tend to "smear out" the fringe pattern for a single size particle. The effect of such a "smearing out" is shown in figure 3.9 for radiation of wavelength 6.7 μm. The diffraction-reflection pattern from a sphere of radius 50 μm is compared with the pattern from a Gaussian distribution of spheres having a mean radius of 50 μm and a standard deviation of 10 μm. As can be seen, the pattern for the distribution does tend to smooth out the fringes to a great extent and is fairly close to the smooth curve of the pattern, particularly at smaller angles where most of the energy is scattered. Small differences at larger angles are not too significant.

To further take account of the effect of a finite distribution, the smooth curve was forced to take on a value at $\theta = 0$ which is approximately 25 percent greater than the corresponding value for the original curve. The reason for this can be seen upon integrating the value of the diffraction pattern at $\theta = 0$ over a Gaussian size distribution. Since the value at $\theta = 0$ varies as a_s^4, which will be seen a little later, the integral represented by $\mathcal{I}$ is given by

$$\mathcal{I} = \frac{1}{\sqrt{2\pi}} \cdot \frac{1}{\sigma} \int_0^\infty a_s^4 e^{-\left(\frac{a_s - \bar{a}_s}{\sqrt{2}\,\sigma}\right)^2} da_s$$
$$\approx \bar{a}_s^4 \left[1 + 6\left(\frac{\sigma}{\bar{a}_s}\right)^2 + 3\left(\frac{\sigma}{\bar{a}_s}\right)^4\right] \qquad (3\text{-}13)$$

where σ is the standard deviation of the distribution. Considering a typical value for σ/a_s to be 1/5, then $\mathcal{I} \approx 1.245\ a_s^4$ which accounts for the 25 percent increase. Figure 3.9 shows this increase.

Another way of showing the similarities and differences between the diffraction-reflection approximation and the exact Mie theory is to compare their cumulative scattered fluxes $f(\theta)$, which is defined by the relation,

$$f(\theta) = \frac{2\pi \int_0^\theta I(\theta) \sin\theta\, d\theta}{2\pi \int_0^\pi I_{Mie}(\theta) \sin\theta\, d\theta} \qquad (3\text{-}14)$$

where $I(\theta)$ is the intensity versus the scattering angle, θ, computed either according to the diffraction-reflection approximation or by the Mie theory. The numerator, therefore, represents the total energy scattered between the angles 0° and θ while the denominator represents the total energy scattered in all directions, computed according to the Mie theory. For the exact Mie case, $f(\theta)$ approaches unity as θ approaches 180° and therefore, is also the fraction of the total energy

scattered between 0° and θ. In the diffraction-reflection approximations used, the assumption was made that the spheres that scatter the radiation are very large. As a consequence, the extinction efficiency factors that result are equal to two. A computation using the Mie theory to obtain these factors for the wavelengths and size spheres actually considered, show that the extinction efficiency factors are about five percent greater than the value of two. The greater the ratio of the size of the sphere to the wavelength of the radiation, the closer will the value of the extinction efficiency factor approach two.

To correct for this difference, the magnitude of the intensity must be adjusted by a factor so that the correct amount of radiation is extinguished. Only after this is done can the diffraction-reflection approximation and the results of the Mie theory be properly compared.

Figure 3.10 shows the comparisons of the normalized cumulative fluxes of the adjusted diffraction-reflection approximation with that obtained from the Mie theory. One may notice immediately the fairly close agreement at small scattering angles, where most of the energy is scattered. Substantial differences at larger angles are not too important since multiple scattering effects are fairly small and we shall be mostly concerned with the radiation emerging upward in a small cone of directions around the vertical. The Medium Resolution Radiometer aboard the Nimbus III Satellite that operates in the wavelength regions plotted, have half angular fields of view of approximately 1.5°. As the angular field of view increases, the poorer the approximations become; but then the inhomogenieties in the field of view are important.

It seems justifiable to conclude that the diffraction-reflection approximation represents the exact scattering pattern sufficiently well for our purposes. The larger the radii of the cylinders or spheres, the better the approximation becomes.

C. Comparisons of the Scattering Patterns for Spheres and Randomly Oriented Cylinders

To find the angular intensity distribution from randomly oriented cylinders the intensity must be averaged over all azimuth angles ϕ and orientations γ. Let $\langle\ \rangle$ be the operator for averaging over ϕ and $\overline{\ \ }$ be the operator for averaging over γ. The intensity from randomly oriented cylinders, I_{rc}, may thus be written symbolically,

$$I_{rc} = \frac{k^2}{4\pi^2 r^2} I_0 \langle \overline{(GD)}^2 \rangle \tag{3-15}$$

For each cylinder, $G = 2\ell\, a_c \sin\gamma$ and therefore

$$GD = (2\ell a \sin\gamma)\ \frac{\sin(k\frac{\ell}{2}\sin\gamma\sin\theta\sin\phi)}{(k\frac{\ell}{2}\sin\gamma\sin\theta\sin\phi)}\ \frac{\sin(ka_c\sin\theta\cos\phi)}{(ka_c\sin\theta\cos\phi)} \tag{3-16}$$

and

$$\langle (GD)^2 \rangle = \frac{1}{2\pi}\int_0^{2\pi}(GD)^2 d\phi = \frac{16}{k^4\sin^4\theta}\cdot\frac{1}{2\pi}\int_0^{2\pi}\frac{\sin^2(m\sin\phi)}{\sin^2\phi}\,\frac{\sin^2(n\cos\phi)}{\cos^2\phi}\,d\phi \tag{3-17}$$

where

$$m = \frac{k\ell}{2}\sin\gamma\sin\theta \tag{3-18}$$

and

$$n = ka_c\sin\theta \tag{3-19}$$

Also,

$$\overline{\sin\gamma} = \frac{2\pi\int_0^{\pi}\sin\gamma\sin\gamma\,d\gamma}{2\pi\int_0^{\pi}\sin\gamma\,d\gamma} = \frac{\pi}{4} \approx .785 \qquad (3\text{-}20)$$

A reasonably good approximation to the integral in equation (3-17) may be deduced after consideration of the form taken by the integrand in a typical case. Let us assume that we have crystals each with a radius of 30 μm and length 240 μm and let us further assume that radiation of wavelength 6.7 μm is incident upon them. If the crystals are randomly oriented, on the average

$$m \sim 88\sin\theta \qquad (3\text{-}21)$$

and

$$n \sim 28\sin\theta \qquad (3\text{-}22)$$

Figure 3.11 shows the variation of the function, $f(\phi) = \frac{\sin^2(m\sin\phi)}{\sin^2\phi}$ with ϕ for m = 10 which corresponds in the above case to $\theta \sim 6.5°$. One notices immediately the strong peaks that occur at ϕ = 0°, 180°, and 360° and the relatively quick drop off toward very low values a few degrees away. These features are further enhanced at even larger values of m, the curves then beginning to appear very much like a series of Dirac δ functions. In fact, it can be shown that 1/m $f(\phi)$ does approach a series of δ functions as m approaches ∞.

The δ function is defined by the following properties:

i. $\delta(\phi - a) = \infty$ for $\phi = a$

ii. $\delta(\phi - a) = 0$ for $\phi \neq a$

iii. $\frac{1}{2\pi}\int_0^{2\pi}\delta(\phi - a)\,d\phi = 1$ if $0 \leq a \leq 2\pi$ (3-23)

and has the additional property,

$$\frac{1}{2\pi}\int_0^{2\pi}\delta(\phi-a)f(\phi)\,d\phi = f(a) \quad \text{if} \quad 0 \le a \le 2\pi \tag{3-24}$$

It can be shown that 1/m $f(\phi)$ also satisfies i, ii, and iii in the limit as m approaches ∞. Since

$$\frac{1}{m}f(\phi) = m\left[\frac{\sin(m\sin\phi)}{m\sin\phi}\right]^2 \tag{3-25}$$

then,

$$\frac{1}{m}f(\phi) \xrightarrow[\phi \to 0^\circ, 180^\circ, 360^\circ]{} m \xrightarrow[m\to\infty]{} \infty \tag{3-26}$$

$$\frac{1}{m}f(\phi) \le \frac{1}{m} \xrightarrow[m\to\infty]{} 0 \tag{3-27}$$
$$\phi \neq 0^\circ, 180^\circ, 360^\circ$$

and

$$\frac{1}{2\pi}\int_0^{2\pi}\frac{1}{m}f(\phi)\,d\phi \simeq \frac{1}{m}\cdot\frac{4}{2\pi}\int_0^{\infty}\frac{\sin^2 m\phi}{\phi^2}\,d\phi = 1 \tag{3-28}$$

The integral approaches 1 exactly as m approaches ∞. Equations (3-25) through (3-28) demonstrate that 1/m $f(\phi)$ does approach a series of δ functions as m approaches ∞. $f(\phi)$ can then be approximated for finite m by the expression,

$$f(\phi) \equiv \frac{\sin^2(m\sin\phi)}{\sin^2\phi} \simeq m\left[\frac{1}{4}\delta(\phi)+\frac{1}{2}\delta(\pi-\phi)+\frac{1}{4}\delta(2\pi-\phi)\right] \tag{3-29}$$

Then,

$$\begin{aligned}\langle(GD)^2\rangle &\simeq \frac{16}{A^4\sin^4\theta}\cdot\frac{1}{2\pi}\int_0^{2\pi} m\left[\tfrac{1}{4}\delta(\phi)+\tfrac{1}{2}\delta(\pi-\phi)+\tfrac{1}{4}\delta(2\pi-\phi)\right]\frac{\sin^2(n\cos\phi)}{\cos^2\phi}\,d\phi \\ &= \frac{16}{A^4\sin^4\theta}\,m\sin^2 n\end{aligned} \tag{3-30}$$

or alternatively,

$$\langle (GD)^2 \rangle \simeq \frac{16}{k^4 \sin^4\theta} m n^2 E^2(n)$$

$$= \frac{8 l q_c^2}{k \sin\theta} \sin\gamma E^2(k q_c \sin\theta) \qquad (3\text{-}31)$$

Averaging over γ,

$$\langle \overline{(GD)^2} \rangle \simeq \frac{2\pi l q_c^2}{k \sin\theta} E^2(k q_c \sin\theta) \qquad (3\text{-}32)$$

is obtained. As a result,

$$I_{nc} = \frac{I_0}{r^2} \frac{k l q_c^2}{2\pi \sin\theta} E^2(k q_c \sin\theta) \qquad (3\text{-}33)$$

which is a reasonably good approximation for angles θ such that $m \geq 10$.

The first minimum of $E^2(k\, a_c \sin\theta)$ occurs when $k\, a_c \sin\theta = \pi$. In the example considered previously this leads to $\theta_{min} \approx 6.4°$ which is quite close to the cutoff angle of applicability of equation (3-33). We may then say that equation (3-33) is roughly valid down to the first minimum of the function $E^2(k\, a_c \sin\theta)$.

For small θ, we may write

$$(GD)^2 \simeq 4 l^2 q_c^2 \sin^2\gamma \left[1 - \frac{k^2 a_c^2 \sin^2\theta \cos^2\phi}{3}\right]\left[1 - \frac{k^2 l^2 \sin^2\theta \sin^2\gamma \sin^2\phi}{12}\right] \qquad (3\text{-}34)$$

Therefore,

$$\langle \overline{(GD)^2} \rangle \simeq 4 l^2 q_c^2 \left[\overline{\sin^2\gamma} - \frac{k^2 q_c^2 \sin^2\theta\, \overline{\sin^2\gamma}}{6} - \frac{k^2 l^2 \sin^2\theta\, \overline{\sin^4\gamma}}{24}\right] \qquad (3\text{-}35)$$

It can be readily verified that

$$\overline{\sin^2\gamma} = \frac{2}{3} \qquad (3\text{-}36)$$

and

$$\overline{\sin^4\gamma} = \frac{8}{15} \tag{3-37}$$

Then,

$$\langle(\overline{GD})^2\rangle = \frac{8}{3}\ell^2 a_c^2\left[1 - \frac{k^2}{30}(\ell^2 + 5a_c^2)\theta^2\right] \tag{3-38}$$

which results in

$$I_{1c} = \frac{I_0}{R^2}\cdot\frac{2}{3\pi^2}k^2\ell^2 a_c^2\left[1 - \frac{k^2}{30}(\ell^2 + 5a_c^2)\theta^2\right] \tag{3-39}$$

for small θ.

As stated earlier, these intensities are to be compared with those from spheres that scatter and absorb out of an incident beam as much energy as would be scattered and absorbed by the model cylinders. For the size particles and infrared wavelengths that will be studied, the scattering and absorption cross sections are both nearly equal to the area of the crystal projected upon the plane normal to the direction of propagation of the incident beam, regardless if the particle is spherical or cylindrical. As a consequence, the comparison spheres should have a cross-sectional area equal to the mean projected area of the cylinders.

If a_c denotes the radii of the cylinders and a_s the radii of the equivalent spheres, then

$$\pi a_s^2 = 2a_c\ell\,\overline{\sin\gamma} = a_c\ell\frac{\pi}{2} \tag{3-40}$$

or

$$a_s = \sqrt{\frac{\ell a_c}{2}} \tag{3-41}$$

In the example considered above, $a_s = 60\,\mu m$. The intensity pattern from a sphere of radius a_s is given by

$$I_s(\theta) = \frac{I_0}{r^2} \frac{k^2 a_s^4}{4} F^2(k a_s \sin\theta) \tag{3-42}$$

where

$$F(u) = \frac{2 J_1(u)}{u} \tag{3-43}$$

The expression given by equation (3-42) is valid for all θ.

We are now in a position to derive approximate expressions for the smooth curves, for it is these curves we are most interested in comparing in light of what was discussed previously. Let us first consider the scattering pattern for the cylinders. Equation (3-33) gives the intensity for angles such that $k\,a_c \sin\theta >> 10$ which for the previous model leads to $\theta \geq 6.5°$. For such angles, the smooth curve will very nearly coincide with the curve obtained by setting the sine function equal to 1/2 in the numerator of the intensity expression. The smooth curve is then given by

$$\tilde{I}_c(\theta) = \frac{I_0}{r^2} \frac{b a_c}{4\pi k} \frac{1}{\sin^3\theta} \tag{3-44}$$

where

$$b = \frac{l}{a_c} \tag{3-45}$$

The value of $\tilde{I}_c$ at $\theta = 0$ may be obtained from equation (3-39). It is given by

$$\tilde{I}_c(0) = \frac{I_0}{r^2} \cdot \frac{2}{3\pi^2} k^2 b^2 a_c^4 \cdot (1.25) \tag{3-46}$$

The smooth curve between the lower limit of applicability of equation (3-44) and $\theta = 0$ are joined by a fairly smooth, monotonically increasing curve as θ goes to zero.

The smooth curve for the equivalent spheres can be obtained similarly. For angles θ such that $k\, a_s \sin\theta >> 1$, equation (3-42) becomes

$$I_s(\theta) = \frac{I_0}{r^2} \frac{2k^2 a_s^4}{\pi} \frac{\sin^2\left(k a_s \sin\theta - \frac{\pi}{4}\right)}{(k a_s \sin\theta)^3} \qquad (3\text{-}47)$$

Actually equation (3-47) is a good approximation for angles as small as 7 to 10° for the spheres of radius 60 μm which are equivalent spheres to the model cylinders. Again, setting the sine function in the numerator equal to 1/2 the smooth curve, $\tilde{I}_s(\theta)$ that results is

$$\tilde{I}_s(\theta) \simeq \frac{I_0}{r^2} \frac{1}{\pi} \frac{a_s}{k} \frac{1}{\sin^3\theta} \qquad (3\text{-}48)$$

Substituting for a_s from equation (3-41) and for ℓ from equation (3-45) into equation (3-48),

$$\tilde{I}_s(\theta) \simeq \frac{I_0}{r^2} \frac{1}{\pi} \sqrt{\frac{b}{2}} \frac{a_c}{k} \frac{1}{\sin^3\theta} \qquad (3\text{-}49)$$

is obtained.

Since $F^2(k a_s \sin\theta) = 1$ at $\theta = 0$,

$$\tilde{I}_s(0) = \frac{I_0}{r^2} \frac{k^2 a_s^4}{4} \cdot (1.25)$$

$$= \frac{I_0}{r^2} \frac{k^2 b^2 a_c^4}{16} \cdot (1.25) \qquad (3\text{-}50)$$

Again, the smooth curves between the lower limit of applicability of equation (3-49) and $\theta = 0$ will be a monotonically increasing curve as θ goes to zero.

Let us now compare the expressions we have derived for the smooth curves. We notice immediately that the expressions in equations (3-44) and (3-49) have the identical functional form, the intensity varying with θ as $1/\sin^3 \theta$. However, the amplitudes in general differ. The ratio of the amplitude for the cylinder to that of the sphere gives the result

$$\frac{\tilde{I}_c(\theta)}{\tilde{I}_s(\theta)} = \sqrt{\frac{b}{8}} \qquad (3\text{-}51)$$

The amplitudes are then equal for b = 8, which was our choice for the model cylinders. For b = 16, the ratio is equal to $\sqrt{2}$, and for b = 4 it is $1/\sqrt{2}$. In general, columnar type crystals have dimensions that are within this range of b with a maximum frequency of occurrence close to 5 (Ono, 1969).

The intensities at $\theta = 0$ can also be compared. The ratio of the intensity for the cylinders to that of the equivalent sphere results in

$$\frac{I_c(0)}{I_s(0)} = \frac{32}{3\pi^2} \simeq 1.08 \qquad (3\text{-}52)$$

The ratio is therefore independent of size and fairly close to unity.

This analysis shows that, for very small angles, the scattering pattern for the cylinders will be quite close to the pattern for the equivalent spheres. At larger angles, the patterns will continue to be similar for values of b near 8 and be nearly identical at b = 8.

These results can be graphically seen in figure 3.12 where the diffraction pattern for model cylinders of radius 30 μm and length 240 μm is plotted along with the pattern for the equivalent spheres or radius 60 μm. Also shown are the smooth curves which fit very closely to the

approximations derived. Figure 3.13 shows the same smooth curves along with the curves for a model of cylinders of radius 30 μm and length 480 μm and equivalent spheres of radius 85 μm.

All of these analyses of the diffraction pattern from randomly oriented cylinders have neglected the end effects; that is the computations actually apply only to long cylinders. For example, the projected length of the cylinder upon the plane normal to the direction of incidence is not equal to $\ell \sin \gamma$, but is somewhat larger due to the addition of a portion of the end projected upon the plane.

On may approximate the contribution to the diffraction from these end effects fairly well by replacing the cylinder with a rectangular solid having the same length as the cylinder and a width equal to the cylindrical diameter. The computation of the diffraction pattern for the rectangular solid is performed in Appendix C with the result that to a good approximation the length in all of the diffraction formula derived previously need only be changed by the factor, $(1 + 4/\pi b)$. In other words an actual length is replaced by an effective length. As a result the intensity is increased by this factor. Also, the radius of the equivalent sphere is increased as well as the corresponding intensity. After making all the appropriate changes, the ratio $\frac{\tilde{I}_c(\theta)}{\tilde{I}_s(\theta)}$ will now be given by the expression

$$\frac{\tilde{I}_c(\theta)}{\tilde{I}_s(\theta)} = \sqrt{\frac{b}{8}\left(1 + \frac{4}{\pi b}\right)} \qquad (3\text{-}53)$$

The amplitudes are then equal for b = 6.73, a value closer to the ratios that actually occur than previously calculated. At $\theta = 0$, the ratio of the intensities are the same as previously since the intensities both increase by the same factor.

It therefore appears from all this evidence that a randomly oriented distribution of cylinders may be replaced by equivalent spheres in computations of the scattering patterns for radiation at least in the infrared wavelength region, 6 to 15 μm.

D. Scattering Patterns for Cylinders Randomly Oriented in a Single Plane

In the analyses of Chapter Two strong evidence was found for a preferential orientation of the axes of hexagonal ice prisms found in cirrus clouds. It was shown that because of the range of Reynolds numbers involved and the optical phenomena that are observed, the long axes tend to lie in a horizontal plane. Aside from this important restriction, the crystals can have any orientation. As a result, the scattering functions for a two-dimensional random orientation will be derived and compared with the functions derived for the three-dimensional random orientation of the cylinders.

Consider a beam of radiation which is incident upon a horizontal plane containing ice cylinders randomly distributed in two dimensions as discussed above and let θ' be the angle that the beam makes with the upward pointing normal to the plane. The projection of the beam upon the horizontal plane will define an X-axis. The orientation of any cylinder axis may then be specified by the azimuth angle ϕ measured from the X-axis. Since the projection of the cylinders upon a plane normal to the direction of the incident beam is required for computing the diffraction, let us

define ℓ' as the length of the projection of the cylinder and ℓ the actual length of the cylinder. It can then be readily shown (see figure 3.14) that

$$\ell' = \ell\sqrt{1 - \cos^2\phi \sin^2\theta'} \qquad (3\text{-}54)$$

The radii of the cylinders which we shall call a_c are unchanged by any projection.

An X'-axis in the plane normal to the beam will be defined as the projection of the X-axis vertically upon the plane. Then, the orientation of the projection of any cylinder can be described by the azimuth angle ϕ' measured with respect to the X'-axis. For convenience the horizontal plane will be referred to as the H-plane and the plane normal to the beam will be referred to as the N-plane.

A point P in the H-plane with coordinates (x,y) has an azimuth ϕ associated with it given by

$$\tan\phi = \frac{y}{x} \qquad (3\text{-}55)$$

The projection, P', of this point into the N-plane will have the coordinates ($x\cos\theta'$,y). As a result, the azimuth angle, ϕ', associated with P' will be given by

$$\tan\phi' = \frac{x}{x\cos\theta'} = \frac{\tan\phi}{\cos\theta'} \qquad (3\text{-}56)$$

Equation (3-56) can then be used to relate the azimuth angle of the cylinder with the azimuth angle of its projection.

The diffraction function D for each cylinder may now be written down at once (see equation (3-8)).

$$D(\Theta\,\phi_o') = E\left(\tfrac{1}{2} k l' \sin\Theta \sin(\phi_o' - \phi')\right) E\left(k a_c \sin\Theta \cos(\phi_o' - \phi')\right) \qquad (3\text{-}57)$$

where Θ is the polar angle of the emerging beam of radiation (scattering angle) with respect to the incident beam, and ϕ_o' is the azimuth of the emerging beam measured in the N-plane. We shall denote by ϕ_o the azimuth angle in the H-plane corresponding to ϕ_o'. The projected area of the cylinder, G, is given by

$$G = 2 a_c l' \qquad (3\text{-}58)$$

Then,

$$(GD)^2 = \frac{16}{k^4 \sin^4\Theta} \left\{ \frac{\sin^2[m \sin(\phi_o' - \phi')]}{\sin^2(\phi_o' - \phi')} \quad \frac{\sin^2[n \cos(\phi_o' - \phi')]}{\cos^2(\phi_o' - \phi')} \right\} \qquad (3\text{-}59)$$

where

$$m = \frac{k l'}{2} \sin\Theta \qquad (3\text{-}60)$$

and

$$n = k a_c \sin\Theta \qquad (3\text{-}61)$$

a result similar to that derived in section C.

As before, let $\langle\ \rangle$ be the operator for averaging over all crystal orientations. Then

$$\begin{aligned} \langle (GD)^2 \rangle &= \frac{1}{2\pi} \int_0^{2\pi} (GD)^2 d\phi \\ &= \frac{1}{2\pi} \int_0^{2\pi} (GD)^2 \frac{d\phi}{d\phi'} d\phi' \end{aligned} \qquad (3\text{-}62)$$

From equation (3-56), we may determine the factor $d\phi/d\phi'$. As a result,

$$\langle (GD)^2 \rangle = \frac{16}{k^4 \sin^4\Theta} \cdot \frac{1}{2\pi} \int_0^{2\pi} \frac{\sin^2[m \sin\eta]}{\sin^2\eta} \frac{\sin^2[n\cos\eta]}{\cos^2\eta} \frac{\sec^2(\phi_0' - \eta)\cos\theta'}{1+\cos^2\theta' \tan^2(\phi_0'-\eta)} d\eta \qquad (3\text{-}63)$$

where

$$\eta = \phi_0' - \phi' \qquad (3\text{-}64)$$

The integral above may be approximated in exactly the same manner as was done in section C. This leads to

$$\langle (GD)^2 \rangle = \frac{16}{k^4 \sin^4\Theta} \cdot \frac{1}{2\pi} \int_0^{2\pi} \ln\left[\tfrac{1}{4}\delta(\eta) + \tfrac{1}{2}\delta(\pi-\eta) + \tfrac{1}{4}\delta(2\pi-\eta)\right] \frac{\sin^2(n\cos\eta)}{\cos^2\eta} \frac{\sec^2(\phi_0'-\eta)\cos\theta'}{1+\cos^2\theta' \tan^2(\phi_0'-\eta)} d\eta \qquad (3\text{-}65)$$

and finally,

$$\langle (GD)^2 \rangle = \frac{8 l q_c^2}{k \sin\Theta} \frac{[1-\cos^2\phi_0 \sin^2\theta']^{\frac{3}{2}}}{\cos\theta'} E^2(k q_c \sin\Theta) \qquad (3\text{-}66)$$

The intensity as a function of the angles Θ, θ', and ϕ_0 is therefore

$$I(\Theta, \theta', \phi_0) = \frac{k^2 I_0}{4\pi^2 r^2} \langle (GD)^2 \rangle$$

$$= \frac{I_0}{\pi^2} \frac{2 k l q_c^2}{\pi^2} \frac{[1-\cos^2\phi_0 \sin^2\theta']^{\frac{3}{2}}}{\cos\theta'} \frac{E^2(k q_c \sin\Theta)}{\sin\Theta} \qquad (3\text{-}67)$$

The computations which will be discussed in the next chapter are averages over the azimuth angle ϕ_0. As a result,

$$I(\Theta,\Theta') = \frac{1}{2\pi}\int_0^{2\pi} I(\Theta,\Theta';\phi_0)\,d\phi_0$$
$$= \frac{I_0}{r^2}\,\frac{2\pi l q_c^2}{\pi^2}\,\frac{E^2(\pi q_c \sin\Theta)}{\sin\Theta}\,c(\Theta') \qquad (3\text{-}68)$$

where

$$c(\Theta') = \frac{1}{2\pi\cos\Theta'}\int_0^{2\pi}\left[1-\cos^2\phi_0\sin^2\Theta'\right]^{\frac{3}{2}}\,d\phi_0 \qquad (3\text{-}69)$$

The integral in the expression for $c(\theta')$ cannot be written in closed form. We may, however, write $c(\theta')$ in a different form. The cross-section for scattering due to the diffraction, C_{sca}, can be obtained from the relation

$$C_{sca} = \frac{2\pi}{I_0}\int_0^{\pi} I(\Theta,\Theta')\,r^2\sin\Theta\,d\Theta$$
$$= \frac{4}{\pi}\,\pi l q_c^2\,c(\Theta')\int_0^{\pi} E^2(\pi q_c \sin\Theta)\,d\Theta \qquad (3\text{-}70)$$

The integral above may be sufficiently approximated by replacing $\sin\Theta$ by Θ and extending the limit of the integration to infinity. Then,

$$C_{sca} = \frac{4}{\pi}\,\pi l q_c\,c(\Theta')\,\frac{\pi}{2} = 2\pi l q_c\,c(\Theta') \qquad (3\text{-}71)$$

The mean projected area of the cylinder, $\bar{A}$, is given by

$$\bar{A} = 2a_c\bar{l} = 2a_c l\cdot\frac{2}{\pi}\int_0^{\frac{\pi}{2}}\sqrt{1-\sin^2\Theta'\cos^2\phi}\,d\phi$$
$$= \frac{4a_c l}{\pi}\,E_1(\sin\Theta') \qquad (3\text{-}72)$$

where $E_1(\sin\theta')$ is the elliptic integral of the second kind. The efficiency factor for scattering, Q_s, is defined as the ratio of the scattering cross-section to the geometric cross-section. In our case,

$$Q_s = \frac{2\lambda q_c\, c(\theta')}{\frac{4 q_c \ell}{\pi} E_1(\sin\theta')} = \frac{\pi}{2} \frac{c(\theta')}{E_1(\sin\theta')} \tag{3-73}$$

Therefore,

$$c(\theta') = \frac{2 Q_s}{\pi} E_1(\sin\theta') \tag{3-74}$$

In the limit of geometric optics, Q_s approaches unity while for particles a little larger than the wavelength, which will be the case for the scattering of infrared radiation, Q_s differs from unity by a small percentage ($\sim$ 5-15%).

We may then write the intensity function in the form,

$$I(\Theta,\theta') = \frac{I_0}{r^2} \frac{4}{\pi^3} A \lambda q_c^2 E_1(\sin\theta') \frac{E^2(\ell q_c \sin\Theta)}{\sin\Theta} \tag{3-75}$$

where Q_s has been set equal to unity.

A comparison of the intensity function of equation (3-75) with the corresponding function derived for the randomly oriented cylinders in three dimensions, shows that the variation of the scattered intensity with scattering angle, Θ, is described in both cases by the same function; only the magnitude differs. For the two-dimensional random orientation the magnitude of the intensity varies with θ'.

For each incident direction, θ', an equivalent sphere may be defined in the same manner as before; one can then compare the resulting intensity patterns to see how much similarity there is. We already know that the shapes of the smoothed curves will be the same; one need only compare the amplitudes.

Before proceeding with these comparisons, the intensity for $\Theta = 0$ must be derived since the intensity function of equation (3-75) is only valid down to approximately the first minimum of $ka_c \sin\Theta$. For $ka_c = 30$, $\Theta_{min} \sim 6°$. The curve at $\Theta \approx 6°$ can then be joined by a fairly smooth curve to the value at $\Theta = 0$ as discussed in the preceding section.

For $\Theta = 0$, we have $D(\Theta) = 1$; therefore

$$(GD)^2 = 4a_c^2 l^2 (1 - \cos^2\phi \sin^2\theta') \tag{3-76}$$

Then

$$\langle (GD)^2 \rangle = 4a_c^2 l^2 \left(1 - \frac{\sin^2\theta'}{2}\right) \tag{3-77}$$

Therefore

$$I(0,\theta') = \frac{I_0}{r^2} \frac{1}{\pi^2} k^2 a_c^2 l^2 \left(1 - \frac{\sin^2\theta'}{2}\right) \tag{3-78}$$

As before, smooth curves, $\tilde{I}_c(\Theta, \theta')$, can be defined. They are given by

$$\tilde{I}_c(\Theta,\theta') = \frac{I_0}{r^2} \frac{2}{\pi^3} \frac{ba_c}{k} \frac{1}{\sin^3\Theta} E_1(\sin\theta') \tag{3-79}$$

where $b = l/a_c$. The smooth curve for the sphere is given by

$$\tilde{I}_s(\Theta) = \frac{I_0}{r^2} \frac{1}{\pi} \frac{a_s}{k} \frac{1}{\sin^3\Theta} \tag{3-80}$$

where a_s is the radius of the equivalent sphere as determined from the relation

$$\pi a_s^2 = \bar{A} = \frac{4a_c l}{\pi} E_1(\sin\theta') \tag{3-81}$$

Therefore,

$$a_s = \frac{2a_c}{\pi} \sqrt{b E_1(\sin\theta')} \tag{3-82}$$

As a result,

$$\tilde{I}_s(\Theta) = \frac{I_0}{r^2}\,\frac{1}{\pi}\,\frac{2q_c}{\pi\ell}\,\sqrt{\ell E_1(\sin\theta')}\,\frac{1}{\sin^3\Theta} \tag{3-83}$$

The ratio of the intensities are then

$$\frac{\tilde{I}_c(\Theta,\theta')}{\tilde{I}_s(\Theta)} = \frac{1}{\pi}\sqrt{\ell E_1(\sin\theta')} \tag{3-84}$$

It is equal to unity when

$$\ell = \frac{\pi^2}{E_1(\sin\theta')} \tag{3-85}$$

Since $E_1(\sin\theta') = \Pi/2$ when $\theta' = 0$, the ratio equals unity when

$$\ell(\theta' = 0) = 2\pi \sim 6.28 \tag{3-86}$$

Also, since $E_1(\sin\theta') = 1$ when $\theta' = \Pi/2$, it will equal unity when

$$\ell(\theta' = \tfrac{\pi}{2}) = \pi^2 \sim 9.87 \tag{3-87}$$

the ratios determined in (3-86) and (3-87) are fairly close to typical values determined from actual ice crystals.

The intensity at $\Theta = 0$ for spheres are given by

$$I_s(0) = \frac{\ell^2 q_s^4}{4} \tag{3-89}$$

$$= \frac{4\ell^2}{\pi^4}\,\ell^2 q_c^4 E_1^2(\sin\theta')$$

Therefore,

$$\frac{\tilde{I}_c(0)}{\tilde{I}_s(0)} = \frac{\pi^2\left(1 - \frac{\sin^2\theta'}{2}\right)}{4E_1^2(\sin\theta')} \tag{3-90}$$

At $\theta' = 0$,

$$\frac{\tilde{I}_c(0)}{\tilde{I}_s(0)} = 1 \tag{3-91}$$

and at $\theta' = \Pi/2$,

$$\frac{\tilde{I}_c(0)}{\tilde{I}_s(0)} = \frac{\pi^2}{8} \simeq 1.23 \tag{3-92}$$

It is seen therefore that the scattering pattern may be fairly well represented by the pattern for an equivalent sphere, even when considering a two-dimensional random orientation. The range in the size of the equivalent spheres as a function of θ' may be readily obtained. Previously for the three-dimensional random orientation,

$$(a_s)_{random} = \sqrt{\frac{a_c 1}{2}} \tag{3-93}$$

Now, in the two-dimensional case, when $\theta' = 0$,

$$\begin{aligned} a_s &= \frac{2}{\pi}\sqrt{a_c 1 \frac{\pi}{2}} \\ &= (a_s)_{random}\sqrt{\frac{4}{\pi}} \\ &\simeq 1.128\,(a_s)_{random} \end{aligned} \tag{3-94}$$

When $\theta' = \Pi/2$,

$$\begin{aligned} a_s &= \frac{2}{\pi}\sqrt{a_c 1} \\ &= (a_s)_{random}\sqrt{\frac{8}{\pi^2}} \\ &\simeq 0.9003\,(a_s)_{random} \end{aligned} \tag{3-95}$$

For the case that (a_s) random is approximately 50 μm, $a_s(\theta' = 0) \simeq 56.4\,\mu$m, and $a_s(\theta' = \pi/2) \simeq 45.0\,\mu$m. Since the variation in the scattering function with such a range in the equivalent sphere is fairly small, one may approximate the scattering function for all θ' by the value of a_s corresponding to the three-dimensional random orientation. The variation in the magnitude in the intensity with θ' will be taken into account when we compute the scattering coefficient k_s, which is a measure of the fraction of the incident radiation that has been scattered per unit of path length of the incident radiation in the cloud layer. It is given by the relationship

$$k_s = N C_{sca} \tag{3-96}$$

where N is the number of crystals per unit volume. For the two-dimensional orientation,

$$k_s(\theta') = \frac{4aN}{\pi} E_1(\sin\theta') \tag{3-97}$$

E. Scattering Patterns for Hexagonal Prisms

In the previous sections, the scattering patterns for radiation incident upon a cloud of ice crystals were approximated by computing the diffraction and reflection from cylinders distributed randomly either in a plane or in space. It was shown that for wavelengths whose absorption coefficients are sufficiently large, refraction of radiation through the crystal may be neglected. Since diffraction depends upon the projection of the crystals upon the plane of the incident wave front and since the hexagonal prisms were assumed randomly distributed about their central axes, the diffraction pattern could be well approximated by the diffraction

pattern for a cylinder of comparable size. Also, the reflection pattern for the hexagonal crystals would be identical to that for the cylinders since the normals to the cylinders would have a spatial distribution identical to those of the hexagonal prisms.

However, when deriving the scattering pattern for wavelengths whose absorption coefficients are fairly small, refraction through the crystal must be taken into account. Since refraction is strongly dependent upon the shape of the crystal, the computation must be performed for the hexagonal prisms themselves. Even random distributions of crystals will not be sufficiently approximated by randomly distributed cylinders when considering refraction. We have already seen that ice crystal clouds produce various kinds of halos, the halo of 22° being the most predominant one. In any computation of the scattering pattern of visible light from ice crystal clouds, such a maximum in the radiation pattern at the halo angle should result. The geometry of a hexagonal prism is such as to produce this halo, while no such halo can occur for cylinders.

As a consequence of this, the scattering patterns of visible radiation from distributions of hexagonal ice prisms were computed under the assumptions that 1) forward scattering in the first few degrees around the incident direction could still be approximated fairly well by diffraction and that 2) refraction and reflection could be computed using the results of geometric optics, the size of the crystals being many times the wavelengths of the radiation.

The method used in computing the refraction and reflection from a prism consists basically of mathematically tracing the paths of a sufficiently large number of equally spaced, parallel rays through the

prism. One can imagine that each ray is initially equivalent to a unit of energy. As each ray encounters a face of the prism, the fraction of the energy that is either reflected or transmitted is computed from the Fresnel coefficients, discussed previously. After a small number of internal reflections (4 or 5) most of the energy that was initially incident upon the prism has been reflected or transmitted by it. In this way, one can obtain the angular distribution of the radiation for any orientation of the prism. The procedure can be continued for a number of orientations to obtain the scattering pattern for any distribution of prisms.

Figure 3.15 shows the results of such a computation for radiation that is incident either normally or at an angle of 45° to the long axes of the prisms, with the orientations of the prisms about their long axes assumed to be random. The fraction of the incident energy that is scattered into a unit angle, $m(\theta)$, is shown versus the scattering angle.

For the case of the normally incident radiation, one may readily notice the rather sharp peak at a scattering angle, $\theta = 0°$, which is due largely to the refraction through opposite faces of the prism that are parallel to one another. This refraction is analogous to that which is observed through a glass window. After the strong forward peak there is a sharp drop in the refraction at angles between zero and 20° followed by a rather large increase toward a peak at 22°. This peak is the cause of the well-known halo previously discussed. After the peak at the halo angle, there is a gradual decrease in the scattered energy to an angle of approximately 45° where the scattering levels off somewhat. The strong forward peak and the peak at 22° are due largely to a single refraction through the crystal (no internal reflection). In fact, a single

refraction contributes nothing to the scattering pattern for angles between 0 to 20° and for angles greater than 45°. The scattered energy in these regions is caused by refractions after a number of internal reflections have occurred. The broad maximum at 152° is the result of the refraction after a single internal reflection.

For the case of the radiation that is incident at 45° to the axes, the halo peak is shifted toward greater angles and diminished in magnitude while the broad maximum now occurs around 80° and is increased in magnitude. The absolute cutoff at 90° is only a consequence of geometry.

Figure 3.16 shows $m(\theta)$ versus θ for a distribution of hexagonal prisms in random orientation. In comparison to figure 3.15 one notices that the halo is still quite prominent though substantially broadened. The prominent secondary maxima that are present in the previous figure are absent in this one. Here, one notices that the scattered energy falls off sharply at angles greater than about 160°.

The fraction of the energy that is scattered into a unit angle (energy per unit degree), $m(\theta)$, for the randomly oriented prisms may be readily transformed into an intensity (energy per unit solid angle). If radiation of intensity I_0 is incident upon a small volume element containing such prisms, than the total energy scattered by the prisms through a large sphere of radius r, centered on the volume element, will be given by

$$2\pi \int_0^{\pi} I(\theta) r^2 \sin\theta \, d\theta = \pi q_s^2 I_0 \qquad (3\text{-}98)$$

where a_s is the radius of an equivalent sphere at the volume element which will scatter an amount of energy equal to that scattered by the prisms. Since the total fraction scattered into all directions is unity by definition,

$$\int_0^{180^\circ} M(\theta)\, d\theta = 1 \tag{3-99}$$

or

$$\frac{\pi}{180^\circ} \int_0^{\pi} M(\theta)\, d\theta = 1 \tag{3-100}$$

A comparison of equations of (3-98) and (3-100) yields

$$M(\theta) = \frac{\pi}{90} \cdot \frac{I(\theta) r^2 \sin\theta}{q_s^2 I_0} \tag{3-101}$$

The non-dimensional intensity, $i_r(\theta)$, is defined by the relation

$$I(\theta) = \frac{I_0}{k^2 r^2}\, i_r(\theta) \tag{3-102}$$

Then,

$$M(\theta) = \frac{\pi}{90}\, i_r(\theta)\, \frac{\sin\theta}{k^2 q_s^2} \tag{3-103}$$

Therefore,

$$i_r(\theta) = \frac{90}{\pi}\, x^2 \left(\frac{M(\theta)}{\sin\theta} \right) \tag{3-104}$$

where $x = ka_s$.

The diffraction pattern for the randomly oriented prisms, $i_d(\theta)$, is well approximated by the diffraction pattern for a distribution of cylinders in random orientation. This pattern, in turn, can be approximated by the diffraction pattern for an equivalent sphere in the manner previously discussed.

Figure 3.17 shows the resulting intensity pattern, $i(\theta) = i_d(\theta) + i_r(\theta)$ for the hexagonal prisms as compared with that for the equivalent sphere for radiation of wavelength 0.76 μm and for an equivalent sphere radius of 25 μm. As can be observed, the principal difference in the two patterns is the rather prominent secondary peak in the prism curve near 23° which corresponds to the halo, while no such peak for the sphere is in evidence. The peak in the scattering pattern for the sphere at 140° is not matched by that in the pattern for the prisms. At angles less than 4° the patterns are identical because of the fact that the diffraction was assumed to be the same for both the prisms and the sphere. Aside from this, the curves have quite different characteristics. It is therefore obvious that the scattering function for an equivalent sphere is not a sufficiently accurate approximation to the scattering function for randomly oriented ice crystals.

Figure 3.18 shows the scattering patterns that result for hexagonal crystals in random orientation for radiation of wavelength 0.55 μm and for equivalent sphere radii of 20, 40, 60, and 100 μm. In accordance with equation (3-104), it is seen that by increasing the radius by a factor of 5, the intensity of the halo will be increased by a factor of 25. While the intensity in the forward direction is many times the intensity of the halo, the actual energy scattered into each of these angular regions is comparable in magnitude. This can be seen in figure 3.19 where $i(\theta) \sin \theta$ is plotted versus θ for each of the equivalent sphere radii. Such curves as these are proportional to the energy scattered per unit angle, similar to the curves of $m(\theta)$ previously shown. Now, one can clearly see the importance of the halo to the overall energy that is scattered. It is interesting to note that

the ratio of the maximum of the curve in the near forward direction (2-4°) to the maximum at the halo angle remains fairly constant, independent of the equivalent sphere radius. Therefore, the relative amount of energy scattered in both of these angular regions will be fairly independent of the size of the crystals.

CHAPTER FOUR

EMISSION, ABSORPTION, AND SCATTERING IN CLOUD LAYERS

A. Formulation of the Equations

The matrix method developed by Twomey, et al. (1966) for the solution of problems dealing with the multiple scattering of light by cloud layers is generalized to include the thermal emission from clouds. While the original method described the scattering and absorption of radiation whose source was outside the cloud layer, the generalization is capable of treating radiation whose source is within the cloud as well as outside of it.

The multiple scattering of a continuous, distributed field of radiation is approximated by the scattering of discrete streams of radiation, the scattering process being considered as a redistribution of scattered energy among the streams. One may visualize that each "direction" actually consists of a small cone of directions which is labeled with an integer to denote it.

If the intensity of the incident radiation field is described by the vector $\underline{v}$ with elements v_j (j representing each incident direction), then a reflection matrix, S, diffuse transmission matrix, T, and a direct transmission matrix, E, can be defined so that $S\underline{v}$, $T\underline{v}$, and $E\underline{v}$ will describe the field of radiation after reflection, diffuse transmission and direct transmission, respectively. Consequently, the elements of the matrices, S, T, and E describe the fraction of the radiation which is incident from a particular stream that is either reflected or transmitted by the cloud layer into another stream.

If radiation described by the intensity vector $\underline{v}$, falls upon a layer of thickness τ_1, which is characterized by the scattering matrices S_1, T_1, and E_1, then radiation $S_1\underline{v}$ will be scattered back by the layer and will consist of all radiation which either does not penetrate the layer or is not absorbed by it. If a second layer of thickness τ_2 is added below, which is characterized by the scattering matrices S_2, T_2, and E_2, the component $S_1\underline{v}$ will not be affected; however, the diffusely and directly transmitted fields, $T_1\underline{v}$ and $E_1\underline{v}$, will be incident upon the second layer, part of which will be reflected by it to become an additional radiation field incident upon the first layer from below. Some of this radiation will be transmitted through the first layer which will add to the reflected radiation field. The process of reflection and transmission by the two layers continues indefinitely as is shown schematically in figure 4.1. The combination of the two layers must be equivalent to a layer of thickness $\tau_1 + \tau_2$. Since $\underline{v}$ is arbitrary, one can relate the matrices for the layer of thickness $\tau_1 + \tau_2$, which will be denoted by S, T, and E, to the matrices S_1, T_1, and E_1 and S_2, T_2, and E_2, by adding together all of the individual contributions. The equations that result are

$$S = S_1 + (T_1+E_1)S_2[I + S_1S_2 + (S_1S_2)^2 + \ldots](T_1+E_1) \qquad (4\text{-}1)$$

and

$$T+E = (T_2+E_2)[I + S_1S_2 + (S_1S_2)^2 + \ldots](T_1+E_1) \qquad (4\text{-}2)$$

where I is the identify or unit matrix.

By adding a layer of thickness τ_1 or τ_2 to the total layer, the solution for an even thicker layer is obtained. This process may be continued to obtain the scattering matrices for a very thick layer. In practice, one begins with two identical layers that are so thin that single scattering theory is sufficiently accurate to determine the scattering matrices. These matrices are then used in the above equations to generate the scattering matrices for a layer double the thickness of the original layer. Continuous doubling will yield solutions for thicker layers.

Similar to the scattering matrices S and T, we may define the matrices B and P, which describe the scattering properties of a small volume element of the cloud. For radiation incident from the i-direction upon an element of volume, B_{ij} is the fraction which is scattered backward into the i-direction and P_{ij} is the fraction which is scattered forward into the i-direction. The matrices B and P are derived from a function called the phase function, $p(\cos\Theta)$ which describes the angular variation of the scattered radiation. Θ, which is called the scattering angle, is the angle between the incident and emerging directions. Aside from a normalization factor, $p(\cos\Theta)$ is identical to the intensity functions derived in Chapter Three. For conservative scattering, the function is normalized so that

$$2\pi \int_0^{\pi} p(\cos\Theta) \sin\Theta \, d\Theta = 1. \qquad (4\text{-}3)$$

If k_s and k_a are the volume scattering and absorption coefficients, respectively, then the single scattering albedo, ω, is given by

$$\omega = \frac{k_s}{k_s + k_a} \qquad (4\text{-}4)$$

and represents the fraction of the original incident radiation that is scattered; $(1 - \omega)$ therefore, is the fraction absorbed. For conservative scattering ($\omega \neq 1$), the normalization of $p(\cos\Theta)$ is generalized to

$$2\pi \int_0^{\pi} p(\cos\Theta) \sin\Theta \, d\Theta = \omega \qquad (4\text{-}5)$$

In order to show how the matrices B and P are related to the phase function, $p(\cos\Theta)$, it will be necessary at this point to define a system of angles in which to describe the different streams.

Referring to figure 4.2, let θ be the polar angle defined with respect to the upward pointing normal to the cloud layer and let ϕ be the azimuth angle with respect to some arbitrary origin. Furthermore, let $\mu = |\cos\theta|$. If μ_j and ϕ_j represent the direction of the j-stream of radiation and μ_i and ϕ_i represent the i-stream, then the scattering angle Θ will be given by

$$\cos\Theta = \pm\mu_i \mu_j + \sqrt{1-\mu_i^2}\sqrt{1-\mu_j^2}\cos(\phi_i - \phi_j) \qquad (4\text{-}6)$$

where the plus sign above corresponds to forward scattering ($\Theta \leq 90°$) and the minus sign corresponds to backward scattering ($90° < \Theta \leq 180°$). As a result, P_{ij} and B_{ij} are given by the expressions

$$P_{ij} = p\left(\mu_i \mu_j + \sqrt{1-\mu_i^2}\sqrt{1-\mu_j^2}\cos(\phi_i - \phi_j)\right) \qquad (4\text{-}7)$$

and

$$B_{ij} = p\left(-\mu_i \mu_j + \sqrt{1-\mu_i^2}\sqrt{1-\mu_j^2}\cos(\phi_i - \phi_j)\right) \qquad (4\text{-}8)$$

For a given wavelength it is convenient to define the optical depth, τ, in a cloud, as that depth to which a vertical beam of radiation ($\mu = 1$) is attenuated to $e^{-\tau}$ of its original value. For oblique rays ($\mu \neq 1$), the beam is attenuated to $e^{-\tau/\mu}$ of its original value. The direct transmission matrix, thus, consists of diagonal elements given by $e^{-\tau/\mu_j}$.

From a knowledge of the variation of the volume scattering and absorption coefficients with the geometric depth, the optical depth may be readily computed. For a geometric depth H in a cloud, the optical depth τ is given by the relation

$$\tau = \int_0^H \left(k_s(z) + k_a(z)\right) dz$$
$$= \int_0^H k(z)\, dz \qquad (4\text{-}9)$$

where $k_a(z)$ includes absorption by the scatterers as well as by any gases intervening between the scatterers. $k(z)$ is known as the extinction coefficient. For a medium whose scattering and absorption coefficients are independent of the depth

$$\tau = k H \qquad (4\text{-}10)$$

To see how the scattering matrices, S and T are related to the matrices B and P, consider the infinitesimal layer of optical thickness $\Delta\tau$, shown in figure 4.3, where radiation of intensity u_j is incident from the direction (μ_j, ϕ_j) within a small solid angle $\Delta\Omega$. The energy of the radiation intercepted by an area ΔA of the layer is equal to $\mu_j u_j \Delta A \Delta\Omega$. Of this energy, a fraction $\Delta\tau/\mu_j$ will be scattered,

a fraction B_{ij} of this reappearing in the i-direction (μ_i, ϕ_i). The energy that emerges therefore in the i-direction due to the scattering, $\Delta\mathcal{E}_i$, is given by

$$\Delta\mathcal{E}_i = B_{ij}\left(\frac{\Delta\tau}{\mu_i}\right)\mu_i\,\mu_j\,\Delta A\,\Delta\Omega$$

$$= B_{ij}\,\mu_j\,\Delta A\,\Delta\Omega\Delta\tau \qquad (4\text{-}11)$$

Since the projection of the area element in the i-direction is equal to $\mu_i\ \Delta A$, the intensity of the emerging radiation in the i-direction, which we shall denote by v_i, is given by

$$v_i = \frac{B_{ij}\,\mu_j\,\Delta A\,\Delta\Omega\,\Delta\tau}{\mu_i\,\Delta A\,\Delta\Omega}$$

$$= \mu_i^{-1} B_{ij}\,\Delta\tau\,\mu_j \qquad (4\text{-}12)$$

One may then identify S_{ij} for the infinitesimal layer with $\mu_i^{-1}B_{ij}\,\Delta\tau$ and similarly for T_{ij}. In matrix form we then have

$$S(\Delta\tau) = M^{-1}\,B\,\Delta\tau \qquad (4\text{-}13)$$

and

$$T(\Delta\tau) = M^{-1}\,P\,\Delta\tau \qquad (4\text{-}14)$$

where M is a diagonal matrix with elements μ_i.

When dealing with the thermal emission from cloud layers, it is convenient to divide the cloud into a number of homogeneous, isothermal layers. Each layer is then characterized by a single temperature, θ, and a single value of the albedo, ω, as well as mean values for the volume scattering and absorption coefficients.

The computation of the emission proceeds by first superposing the two top layers. Reflection and transmission matrices are then obtained in the manner already outlined. From this, one can compute the total fraction of the radiation that was reflected or transmitted for each incident direction. The remaining fraction is therefore the fraction absorbed (absorptivity). Since the absorptivity in the cloud is also equal to the emissivity, the amount that each layer radiates can be computed.

A layer at the temperature θ which has an emissivity a_i will radiate at the wavelength λ into the i-direction (up or down) with an intensity e_i given by the relation

$$e_i = a_i B_\lambda(\theta) \tag{4-15}$$

where B_λ is the Planck function. These sources of emission, together with the scattering matrices for the layers, yield the resulting emissions from the composite layer.

Let us define $\underline{e_{1,+}}$ and $\underline{e_{1,-}}$ to be the emission vectors from the layer of optical thickness τ_1 directed upward and downward, respectively; and let $\underline{e_{2,+}}$ and $\underline{e_{2,-}}$ be the corresponding vectors for the layer of optical thickness τ_2. Furthermore, let $\underline{e_+}$ and $\underline{e_-}$ be the emission vectors for the combination of the two layers. As a result of the multiple reflections and transmissions between the two layers, as shown schematically in figure 4.4, the equations for the emissions that result are

$$\begin{aligned}\underline{e_+} = \underline{e_{1,+}} &+ (T_1 + E_1) S_2 \left[I + S_1 S_2 + (S_1 S_2)^2 + \cdots \right] \underline{e_{1,-}} \\ &+ (T_1 + E_1) \left[I + S_2 S_1 + (S_2 S_1)^2 + \cdots \right] \underline{e_{2,+}}\end{aligned} \tag{4-16}$$

and

$$\underline{e_-} = \underline{e_{2,-}} + (T_2+E_2)S_1\left[I + S_2S_1 + (S_2S_1)^2 + \cdots\right]\underline{e_{2,+}}$$
$$+ (T_2+E_2)\left[I + S_1S_2 + (S_1S_2)^2 + \cdots\right]\underline{e_{1,-}} \qquad (4\text{-}17)$$

$\underline{e_+}$ and $\underline{e_-}$ now take the place $\underline{e_{1,+}}$ and $\underline{e_{1,-}}$, while the matrices S, T, and E appropriate to the layer of optical thickness $\tau_1 + \tau_2$ become the new S_1, T_1, and E_1 matrices. A new set of emission vectors, $\underline{e_{2,+}}$ and $\underline{e_{2,-}}$ are calculated for the third isothermal layer beneath the original two layers. The calculation of the emission vectors for the layer of optical thickness $\tau_1 + \tau_2 + \tau_3$ then proceeds as before with the use of equations (4-16) and (4-17). The process is repeated as each layer is added on below until the emission vectors for the entire cloud layer result.

A considerable improvement in the possible fineness of subdivision of the specified directions is obtained if a finite array of μ's (latitude belts) is considered, while the variations with azimuth angle is treated by expanding the scattering matrices B, P, S, and T and the emission vectors, $\underline{e_+}$ and $\underline{e_-}$ as Fourier series in the azimuth angle. For example, the amount of radiation reflected from the $(\mu_j, 0)$ direction to the (μ_i, ϕ) direction may be written,

$$S_{ij}(\phi) = \sum_{m=0}^{\infty} S_{ij}^{(m)} \cos m\phi \qquad (4\text{-}18)$$

The other matrices and vectors may be similarly expressed. As a result of the orthogonality of the trigonometric functions, the equations separate into equations each of which involve only harmonics of the same order. Equations (4-1), (4-2), (4-16), and (4-17) are then generalized to the following equations:

$$f_m \underline{\underline{S}}^{(m)} = f_m \underline{\underline{S}}_1^{(m)} + (f_m \underline{\underline{T}}_1^{(m)} + \underline{\underline{E}}_1)\, f_m \underline{\underline{S}}_2^{(m)} \left[\underline{\underline{I}} + f_m \underline{\underline{S}}_1^{(m)} \underline{\underline{S}}_2^{(m)} + \cdots\right] (f_m \underline{\underline{T}}_1^{(m)} + \underline{\underline{E}}_1) \qquad (4\text{-}19)$$

$$f_m \underline{\underline{T}}^{(m)} + \underline{\underline{E}} = (f_m \underline{\underline{T}}_2^{(m)} + \underline{\underline{E}}_2) \left[\underline{\underline{I}} + f_m \underline{\underline{S}}_1^{(m)} \underline{\underline{S}}_2^{(m)} + \cdots\right] (f_m \underline{\underline{T}}_1^{(m)} + \underline{\underline{E}}_1) \qquad (4\text{-}20)$$

$$f_m \underline{e}_+^{(m)} = f_m \underline{e}_{1,+}^{(m)} + (f_m \underline{\underline{T}}_1^{(m)} + \underline{\underline{E}}_1) f_m \underline{\underline{S}}_2^{(m)} \left[\underline{\underline{I}} + f_m \underline{\underline{S}}_1^{(m)} \underline{\underline{S}}_2^{(m)} + \cdots\right] f_m \underline{e}_{1,-}^{(m)}$$
$$+ (f_m \underline{\underline{T}}_1^{(m)} + \underline{\underline{E}}_1) \left[\underline{\underline{I}} + f_m \underline{\underline{S}}_2^{(m)} \underline{\underline{S}}_1^{(m)} + \cdots\right] f_m \underline{e}_{2,+}^{(m)} \qquad (4\text{-}21)$$

and

$$f_m \underline{e}_-^{(m)} = f_m \underline{e}_{2,-}^{(m)} + (f_m \underline{\underline{T}}_2^{(m)} + \underline{\underline{E}}_2) f_m \underline{\underline{S}}_1^{(m)} \left[\underline{\underline{I}} + f_m \underline{\underline{S}}_2^{(m)} \underline{\underline{S}}_1^{(m)} + \cdots\right] f_m \underline{e}_{2,+}^{(m)}$$
$$+ (f_m \underline{\underline{T}}_2^{(m)} + \underline{\underline{E}}_2) \left[\underline{\underline{I}} + f_m \underline{\underline{S}}_1^{(m)} \underline{\underline{S}}_2^{(m)} + \cdots\right] f_m \underline{e}_{1,-}^{(m)} \qquad (4\text{-}22)$$

where

$$f_m = \begin{cases} \frac{2\pi}{N} & \text{for } m = 0 \\ \frac{\pi}{N} & \text{for } m \neq 0 \end{cases} \qquad (4\text{-}23)$$

N is the size of the square matrices (number of values of μ).

B. Comparison of Theory with Airplane Observations of Solar Radiation Reflected from Stratiform Clouds

In order to ascertain whether the method of computation discussed above leads to results that are in harmony with actual observations, a comparison was made between the computed angular patterns of solar radiation reflected from stratiform clouds with those measured by medium resolution radiometers from an airplane. In the numerical computations, a Gaussian size distribution of spherical water particles having a mean

radius of 6 μm and a standard deviation of 1 μm was assumed. Using the equations of the Mie theory, the single scattering phase function for such particles was computed, which was then used in the manner discussed in the preceding section to obtain the angular scattering function for a cloud of such particles. The observations consisted of those obtained by two separate groups of investigators looking in the spectral interval 0.2 to 4.0 μm. Cherrix and Sparkmann (1967) looked at stratocumulus clouds from the NASA Convair 990, while Solomonson and Marlatt (1968) looked at California stratus.

Figures 4.5 to 4.8 show the comparisons of the theory with measurement for four special cases. In three of these, the angular patterns are shown for three different azimuth planes for a single solar zenith angle, while in the fourth figure, the angular pattern is only shown for the principal plane and a high sun. While the measurements extend over a spectral interval and include clouds of a variety of thicknesses the computations were made for the single wavelength 0.76 μm and for the single optical thickness, $\tau = 8.4$.

It is fairly apparent from these comparisons that the basic characteristics of the theoretical curves are in good agreement with the observations, although the magnitudes of some of the curves tend to differ in varying degrees. However, one should not expect the magnitudes to necessarily agree, since only a single optical thickness was chosen. Variations of the cloud thickness would tend to shift the curves up or down. Also, the magnitude of the scattering averaged over the spectral range probably differs from that for one wavelength alone.

Although the comparisons were not made for the emission and scattering from cirrus cloud layers, they do show that the method of computation leads to results that are consistent with the measurements.

C. Numerical Results for Model Cirrus Cloud Layers

Using the methods of computation previously discussed, the radiances due to thermal emission and the transmissivities of model cirrus cloud layers were computed for a number of wavelengths. The model clouds were characterized by one of four possible base pressures (500, 400, 300, or 200 mb.), one of three possible ice concentrations (.001, .01, or .1 g/m^3), and one mean ice particle size (equivalent sphere radius of 40 μm). For each combination of these parameters, ten geometric thicknesses were chosen with the maximum thickness set at 5 km. This gave a total of 120 cloud models, with the parameters chosen to embrace the anticipated range of the physical characteristics of actual cirrus clouds.

The wavenumbers for which the computations were made (706.3, 714.3, 750.0, and 899.3 cm^{-1}) correspond to four of the eight channels of the SIRS (Satellite Infrared Spectrometer) instrument aboard the Nimbus III spacecraft. These four channels were chosen because it was expected that the observed radiances would be affected to a measurable degree by the presence of cirrus layers in the observed area. The other four channels observe the stratosphere and are therefore not sensitive to cirrus clouds.

The SIRS instrument was developed principally for the purpose of deducing vertical temperature profiles on a global basis from a satellite. Using numerical inversion techniques, the eight radiance measurements yield sufficient information to produce a fairly accurate vertical temperature profile. Aside from this, other related studies may be

pursued with the radiance data that are available. Utilizing the four channels previously mentioned when cirrus clouds are in the field of view, one is able to study the effect that the clouds have on the radiation that is measured. Along these lines, three sets of SIRS observations were chosen for special study. Two of these sets were chosen because 10/10 cirrus or cirrostratus was reported by ground observers at nearly the same time and place that the SIRS observations were made. Also, radiosonde measurements of the air and dew point temperature profiles were made at a station in the vicinity of each of these SIRS observations. The third set of radiance measurements was taken over a clear area near one of the above cloudy regions, which was to be used for comparison purposes.

For each of the cases above, the atmospheric transmissivities as a function of the pressure were computed for each of the channels using a program developed by Wark, Fleming, and Smith (private communication) which was based upon the transmissivity computations of Drayson (1967). Wark and Fleming used Drayson's results to produce a simplified program for computing the transmissivities through carbon dioxide which included a temperature correction, while Smith (1969) developed a program for computing the transmissivities through water vapor. Drayson (1969) determined a global average transmissivity profile for ozone. Since the bandwidth of each of the channels is fairly narrow, the total transmissivity in each channel may be approximated sufficiently well by the product of the transmissivities through the carbon dioxide, water vapor, and ozone.

The transmissivities obtained above were then assumed capable of being written in the form

$$\tau(0,p) = e^{-\int_0^p k_c(p)\,dp} \qquad (4\text{-}24)$$

where $\tau(0,p)$ is the transmissivity through the atmosphere from a pressure level p=0 to the pressure level p, and $k_G(p)$ is the total gaseous absorption coefficient. To avoid possible confusion between optical thickness and transmissivity, the pressure levels which characterize the transmissivity will always be indicated in parenthesis following the symbol for transmissivity. From the numerical values of $\tau(0,p)$ at each of the pressure levels p, it is a simple matter to extract the numerical values of k_G at each pressure level. This computation was performed with the result that the numerical values of k_G were very nearly the same for all three cases studied. Figure 4.9 shows a plot of the values of k_G that resulted versus the pressure level p. For convenience in later computations the unit of k_G was chosen to be km^{-1} rather than mb^{-1}. For the cirrus radiation computations, only the values of k_G that correspond to the pressure levels between 500 mb and approximately 80 mb are of interest.

In addition to the gaseous absorption coefficients one must determine the scattering and absorption coefficients, k_s and k_a, respectively, due to the ice crystals. These can be readily estimated from the relations

$$k_s = N \pi r^2 Q_s \qquad (4\text{-}25)$$

and

$$k_a = N \pi r^2 Q_a \qquad (4\text{-}26)$$

where Q_s and Q_a are respectively the ice scattering and absorption efficiency factors which may be computed according to the Mie theory, r is the equivalent ice sphere radius, and N is the ice crystal number density (m^{-3}). The ice concentration, $w(g/m^3)$ is given by

$$w = \frac{4}{3} \pi r^3 \rho_i N \qquad (4\text{-}27)$$

where ρ_i is the density of ice. Combining equation (4-25) and (4-26) with equation (4-27) results in

$$k_s = \frac{3w}{4\rho_i r} Q_s \qquad (4\text{-}28)$$

and

$$k_a = \frac{3w}{4\rho_i r} Q_a \qquad (4\text{-}29)$$

The single scattering albedo, ω, at any level in the cloud is given by

$$\omega = \frac{k_s}{k_s + k_a + k_G} \qquad (4\text{-}30)$$

Therefore, from the computed values of k_s, k_a, and k_G, ω may be determined as a function of the depth in the clouds. This is one of the basic parameters that enters into the cirrus radiance computations. Another of the basic parameters that must be specified with the depth in the cloud is the temperature. For each case considered, the temperatures used for the cloud models were those determined by the nearby radiosonde measurement.

All that remains to be determined before the computation of the radiation may be performed are the scattering phase functions. Using the approximations outlined in Chapter Three, two phase functions were obtained. One of these functions was that corresponding to the channel having a wavenumber of 899.3 cm^{-1}, while the other phase function was computed for radiation having a wavenumber of 740 cm^{-1}. A different phase function for each of the latter channels is not necessary since very little variation occurs over the small wavenumber range. The variation of the absorption and scattering coefficients is of a much greater magnitude and was computed for each of the four channels used.

Using the computed values of the single scattering albedo, ω, along with the cloud temperature variation and the scattering phase function, the thermal emission and transmission for the 120 cloud models were computed. Figure 4.10 shows some typical results of the radiance due to self-emission as a function of the thickness of a cloud for clouds whose bases are located at 300 mb. Each quadrant of the figure corresponds to one of the four channels. The results for the three ice concentrations are shown by the three solid curves. It can be readily observed that the radiances increase with ice concentration and generally, but not always, increase with the thickness. At large ice concentrations there is a peak at small thicknesses followed by a gradual decrease in the radiance for larger thicknesses. Again at even larger thicknesses, the radiance increases.

This variation in the radiance can be explained by the fact that there is a competition of two opposing tendencies. As the thickness of the cloud layer is increased there is a tendency for the radiance to increase because of the larger radiating mass. However, the transmission through the cloud layer tends to decrease with increasing thickness, thereby attenuating the radiation as it passes through the remainder of the cloud from its source area. For small cloud thicknesses the transmissivity does not change sufficiently fast to overcome the increase in the radiance due to the increase in the radiating mass. At larger thicknesses the decrease in transmissivity begins to dominate, resulting in a decrease in the radiance. Again, at very large thicknesses the transmissivity does not decrease very fast while the radiating mass continues to increase. There is then a slight increase in the radiance at this point. Also shown in the figure by the dashed curves are the blackbody radiances corresponding

to the temperature of the cloud tops. A radiance greater than the blackbody value means only that radiation from warmer lower layers is transmitted through the cloud with a resulting radiance that is greater than that which would be emitted by a blackbody at the colder cloud top temperature.

Figure 4.11 shows the transmissivities corresponding to the same clouds as described in figure 4.10. For the ice concentration of .1 g/m^3, a layer 1 1/2 kilometers thick is opaque to radiation in all of the channels, while for an ice concentration of .001 g/m^3, clouds up to 5 kilometers thick transmit as much as 50 percent or more.

D. Choice of Cirrus Models that Best Fit SIRS Observations Over Cirrus Clouds

Computations of radiances at satellite level were made using the numerical results for the 120 cloud models. These radiances were then compared with those observed by the SIRS radiometer for the two selected cloud cases in order to study the cloud characteristics that could account for the observed radiances. Table 4.1 is a list of the locations and times of occurrence of the satellite and radiosonde measurements for the two cloud cases and the single cloudless case.

The computations for the cloud cases were performed by first computing the upward intensities at the bases of the clouds due to radiation that is emitted from the earth and the atmosphere below. If $I^{\uparrow}(p_L)$ denotes the intensity at the cloud base at a pressure p_L, then

$$I^{\uparrow}(p_L) = B(p_0)\tau(p_L, p_0) + \int_{p=p_0}^{p_L} B(p)\frac{d\tau(p_L, p)}{dp}dp \qquad (4\text{-}31)$$

TABLE 4.1

LOCATIONS AND TIMES OF OCCURRENCE OF MEASUREMENTS

Location of Radiosonde	Time of Radiosonde	Location of Satellite Measurements	Time of Satellite Measurements
*Flint, Mich. 43.0°N. 83.7°W.	1800Z April 24, 1969	43.24°N. 79.41°W	1612:19Z April 24, 1969
St. Ste. Marie, Michigan. 46.5°N, 84.4°W	1800Z April 24, 1969	46.68°N. 80.89°W.	1613:23Z April 24, 1969
Fort Worth, Tex. 32.8°N. 97.1°W.	1800Z April 22, 1969	32.66°N. 97.45°W.	1736:35Z April 22, 1969

*Clear sky case.

where B(p) is the value of the Planck function at the pressure p, $\tau(p,p')$ is the transmissivity between the pressures p and p' and p_0 is the pressure at the surface of the earth. Since all the transmissivities had been computed from the fixed pressure p=0, equation (4-31) is not directly applicable. As a result of equation (4-24)

$$\tau(0,p) = \tau(0,p_1)\,\tau(p_1,p)$$

or

$$\tau(p_1,p) = \frac{\tau(0,p)}{\tau(0,p_1)} \qquad (4\text{-}32)$$

Substitution of the result of equation (4-32) and its derivative with respect to p into equation (4-31) results in

$$I^{\uparrow}(p_1) = \frac{B(p_0)\tau(0,p_0)}{\tau(0,p_1)} + \int_{p=p_0}^{p_1} \frac{B(p)}{\tau(0,p_1)} \frac{d\tau(0,p)}{dp}\,dp \qquad (4\text{-}33)$$

If $\tau_c(p_U,p_L)$ is made to represent the transmissivity through a cloud that extends from the pressure p_U to the pressure p_L and e_c denotes the radiance due to the emission from the cloud itself, then the intensity that results at the top of the cloud at the pressure p_U, denoted by $E(p_U)$, is given by

$$E(p_0) = e_c + I^{\uparrow}(p_1)\,\tau_c(p_0,p_1) \qquad (4\text{-}34)$$

In a manner similar to the computation of the intensity at the base of the cloud the intensity at the satellite level, $I^{\uparrow}(0)$, is computed from the relation

$$I^{\uparrow}(0) = E(p_0)\tau(0,p_0) + \int_{p=p_0}^{0} B(p) \frac{d\tau(0,p)}{dp}\,dp \qquad (4\text{-}35)$$

It is this value that is to be compared with the observed radiances.

For the case that the field of view does not contain any clouds, the intensity at the satellite level is computed from the relation

$$I^{\uparrow}(0) = B(p_0)\tau(0,p_0) + \int_{p=p_0}^{0} B(p)\frac{d\tau(0,p)}{dp}\,dp \qquad (4\text{-}36)$$

Before making the computations of the radiances for the cloud cases, the radiances for the clear case were determined in order to test the correspondence of the computations with the observed radiances. Table 4.2 shows such comparisons for the four channels for the case at Flint, Michigan. Differences between the observed and computed radiances are what one could reasonably expect considering the possible errors that could occur in the temperature sounding and in the observed radiances themselves. On the basis of this comparison, it was decided that any cloud model that yielded a radiance value that was within 1 erg/cm^2/sec/ster/cm^{-1} of the value observed by the corresponding channel of the SIRS radiometer would be considered a cloud solution for that channel. This criterion is not a crucial one as will be seen in the results that follow.

The procedure for determining which of the model clouds yielded the observed radiances was to plot, for each combination of cloud base pressure and wavelength, a series of curves which gave the variation of the computed radiances with the ice concentration for layers of constant thickness. The thicknesses were chosen in .5 kilometer intervals from 0.5 kilometers to 5.0 kilometers. On the same graph the range of radiance corresponding to the observed values plus and minus 1 erg/cm^2/ster/sec/cm^{-1} was shaded in. For each cloud thickness one could then pick out a maximum and a minimum ice concentration that would satisfy the criterion for a cloud solution. In this way, boundary curves of the ice concentration versus the thickness were drawn. Any point within these boundary curves

TABLE 4.2

RADIANCE COMPARISON FOR A CLEAR SKY*

Wavenumber cm^{-1}	Observed Radiance $erg/cm^2/sec/ster/cm^{-1}$	Computed Radiance $erg/cm^2/sec/ster/cm^{-1}$	Difference $erg/cm^2/sec/ster/cm^{-1}$
706.3	51.67	52.12	+0.45
714.3	63.30	63.99	+0.69
750.0	91.67	92.98	+1.31
899.3	93.01	93.01	0

*Viewed areas was near Flint, Michigan.

would then represent a possible cloud solution for the channel. Superposition of the boundary curves for all four channels will show if one or more of the cloud models give a solution for all channels. This procedure was followed for all four cloud base pressures. The results for the St. Ste. Marie cloud case is shown in figure 4.12 where only the regions of overlap were plotted.

It is readily apparent from this graph that almost any geometric thickness will yield a solution when combined with an appropriate ice concentration. A careful examination of these regions showed that while the ice concentration and thickness varied over wide limits, the product of the two did not. Since the visible optical thickness is proportional to this product, one may conclude that the cloud solutions are restricted to a fairly small range in the visible optical thickness. The optical thickness is defined by

$$\tau_o = k Z \tag{4-37}$$

where k is the extinction coefficient and Z is the geometric thickness. According to equation (4-28) and (4-29), this may be written

$$\tau_o = \frac{3w}{4\rho_i r}\left(Q_s + Q_a\right) Z \tag{4-38}$$

For radiation in the visible wavelength region and ice crystals of the size assumed, it is a fairly good approximation to set $(Q_s + Q_a)$ equal to two. As a result

$$\tau_o = \frac{3}{2}\,\frac{wZ}{\rho_i r} \tag{4-39}$$

For crystals which have an equivalent sphere radius of 40μm

$$\tau_o \simeq 40.7\, w Z \qquad (4\text{-}40)$$

where w is in g/m^3 and Z is in km. For a typical cirrus cloud of 1 kilometer in thickness having an ice concentration of .03 g/m^3 (Feigelson, 1964), τ_o is approximately equal to 1.2. Substitution of the coordinates, w and Z, of points within the regions plotted in figure 4.12, into the above equation yields values of the optical thickness that range from .19 to .27. Also, the albedos that would result for such clouds would be quite low. This can be shown using the theoretical curves in figure 4.13.

To see how consistent these smaller values of the optical thickness are with observations, satellite photographs of the SIRS-viewed area taken at the same time as the SIRS observations were studied. They showed cirrus to be present in the northern position of the field of view, while in the southern half it appeared to be clear. The cirrus in the northern portion seemed to be moderately thin. However, ground observers at St. Ste. Marie reported that cirrostratus covered the entire sky. Other observers north of the region at Great Whale in Canada reported cirrostratus that appeared to be thickening while south of the region at Flint, Michigan, were reports of clear skies. It is quite possible that cirrostratus will not appear in the satellite photographs and still be seen from the ground. According to a recent study made by Allied Research Associates for the Goddard Space Flight Center (1968), in only 28 percent of the observations in which ground observers reported cirrus was cirrus also reported from satellite photographs.

In the second cloud case (Fort Worth, Texas) no single cloud model yielded a solution for all four of the channels. However, if the window channel (899.3 cm^{-1}) was excluded, regions of solution similar to those obtained in the first case were found.

In considering the possible causes of this discrepancy it is helpful to compare the observed radiances with those computed for clear-sky conditions as shown in Table 4.3. Note that the differences between the clear and cloudy values are much the same in the two cases for the first three channels but are markedly different for the window channel. If the difference for the window channel in the second case had been larger by about 3 or 4 ergs/cm^2/ster/sec/cm^{-1}, the boundary curves corresponding to the window channel would have overlapped those of the other channels. This suggests exploration of the possibility that the radiance computed for the window channel was too low. If the surface temperature used in the computations was too low, this would reduce the value of the computed radiance. It is generally known that the radiating temperature of the surface can be as much as several degrees warmer than the air above it. It is this warmer surface temperature that enters into the boundary term of the computed fluxes. In particular, in barren areas such as deserts, the radiation surface temperature can be many degrees higher than the air temperature above the surface. Over oceans, the temperature of the surface is generally fairly close to the air temperature. A temperature difference of 1°C could change the boundary term in the window by about one percent.

A comparison of the surfaces (Williams, 1958) in the two cloud cases shows some rather marked differences. In the St..Ste. Marie area, the surface is almost completely covered with forests and numerous small lakes while in the Fort Worth area the land is generally used for the growing of crops. At the time the satellite measurements were made at St. Ste. Marie, the deciduous type of trees which comprise fifty percent of the

TABLE 4.3

RADIANCE COMPARISONS FOR THE CLOUDY CASES*

Wavenumber cm^{-1}	Observed Radiance $erg/cm^2/sec/ster/cm^{-1}$	Computed Clear Sky Radiance $erg/cm^2/sec/ster/cm^{-1}$	Difference $erg/cm^2/sec/ster/cm^{-1}$
706.3	50.92	52.51	+1.59
714.3	61.28	62.69	+3.41
750.0	84.08	92.36	+8.28
899.3	81.10	90.85	+9.75

*Viewed area was near St. Ste. Marie.

Wavenumber cm^{-1}	Observed Radiance $erg/cm^2/sec/ster/cm^{-1}$	Computed Clear Sky Radiance $erg/cm^2/sec/ster/cm^{-1}$	Difference $erg/cm^2/sec/ster/cm^{-1}$
706.3	53.35	55.43	+2.08
714.3	67.35	70.72	+3.37
750.0	100.54	108.48	+7.94
899.3	116.15	118.69	+2.54

*Viewed area was near Fort Worth, Texas.

forests, had not leafed-out; the balance of the forest is largely coniferous. The radiating surface in a forest is largely the crowns of the trees, which can be expected to be nearly at air temperature.

At the time of the satellite measurements over Fort Worth, the ground would have appeared fallow due to the recent planting of the principal crop of cotton. Also, at this time, the diurnal temperature range at Fort Worth is probably considerably higher than that at St. Ste. Marie. Under these conditions the radiation temperature of the surface near local noon could be a few degrees higher than the reported air temperature. This comparison suggests that it is quite possible that the surface air temperature was an underestimate of the radiative temperature at Fort Worth whereas it was a satisfactory estimate at St. Ste. Marie.

Figure 4.14 shows typical transmissivity curves for the SIRS channels while figure 4.15 shows curves of the weighting function $d\tau(0,p)/d \ln p$. The later curves indicate the levels of the atmosphere that contribute most to the radiance. From these curves and in particular those of the weighting function, it is clear that the window channel is extremely sensitive to the surface temperature, while the channel at 750.0 cm^{-1} is also affected to a smaller extent. If the value of the surface temperature at Fort Worth is too low, as suggested above, the computations in the window and 750.0 cm^{-1} channels are in doubt. Since the weighting functions for the other two channels show that the radiances are not affected very much by the surface temperature, cloud solutions deduced for these two channels alone were determined. Figure 4.16 shows the solutions obtained, which are similar to those obtained for case 1. However, the regions are less well defined because of the use of only two of the channels. Optical thicknesses of the cloud solutions yielded values that ranged from .09 to .46.

Again, photographs of the field of view of the SIRS observations do not show cirrus. A station to the north of the area at the Texas-Oklahoma border reported filaments of cirrus that were scattered and not increasing while reports south of the area at Waco and reports to the west at Abilene indicated a veil of cirrostratus covering the entire sky. Again, this appears to be another case where cirrus was not capable of being detected in satellite photographs.

CHAPTER FIVE

CONCLUSIONS

The principal result of this research was the development of methods for computing the emission, scattering and absorption in ice crystal clouds. Over the past years methods have been developed for treating the transfer of radiation through clouds composed of spherical water drops. In all of these methods, the angular patterns of the radiation scattered from the water drops are described by the Mie theory, which is an exact treatment of the scattering of electromagnetic waves by homogeneous spheres. Such a solution as this for the ice crystal shapes is not possible. Even for such symmetric shapes as circular cylinders, solutions exist only for special orientations of the cylinder with respect to the incident radiation.

However, many investigators have reasoned that if the ice crystals were randomly oriented in space, which seemed to be a reasonable assumption, then the scattering patterns from the ice crystals would, on the average, resemble that for spheres. As a consequence of such reasoning, the radiation in ice crystal clouds was computed by replacing the ice crystals by equivalent spheres. However, this assumption has not been investigated in detail. Even if it were established that the ice crystals were randomly oriented, it would not automatically follow that the scattering patterns for the crystals would be equivalent to that for spheres. Other considerations must be taken into account.

Based upon the analysis of the optical phenomena that are associated with ice crystal clouds and the studies of the hydrodynamic properties of falling crystals, it was concluded that ice crystals in clouds are not

randomly oriented in space. Because of their Reynolds numbers, the crystals fall so that their long axes tend to align with the horizontal. Aside from this restriction, it appears that the axes of the crystals can take any orientation. Thus, the crystals are randomly oriented in any horizontal plane, rather than in space.

In order to study the conditions under which it may be possible to replace the ice crystals by equivalent spheres in the computations of the radiation that is scattered, the ice crystals were approximated by circular cylinders of comparable dimensions. Computations of the scattering pattern for a distribution of cylinders in random orientation with principal axes horizontal were compared with those for equivalent spheres. The comparison showed that the scattering of radiation from ice crystals could be sufficiently approximated by equivalent spheres as long as certain conditions are met. The first of these are that the mean dimensions of the crystal be at least two or three times larger than the wavelength of the radiation, while the second requires that the absorption coefficient in the ice be large enough to make the contribution from refraction negligible. The water vapor band around 6.3 μm and the CO_2 band around 15 μm satisfy these conditions. However, radiation in the visible portion of the spectrum does not, because of the importance of the refracted component. Refraction depends strongly upon the shape of the crystals even when they are randomly oriented.

The conclusions drawn for the case that the crystals are randomly oriented in only horizontal planes would apply equally well if the crystals were randomly oriented in all three dimensions. The only difference is that the mean equivalent sphere radius for the former case is dependent upon the angle of incidence of the radiation, while in the

latter case it is independent of the direction of incidence. Since the variation of the mean radius with incident angle is fairly small in the former case, a single mean radius is sufficiently accurate.

In order to treat the transfer of visible radiation through clouds of hexagonal ice crystals, a method was developed which is based upon the results of geometric ray optics. In this method, a sufficiently large number of equally spaced, parallel rays are mathematically traced through the prisms to determine the contribution to the scattering due to refraction and reflection, while the forward diffracted contribution is approximated by the Kirchhoff formula. Results for a distribution of prisms that are randomly oriented either in space or only in horizontal planes show the expected strong intensity of the radiation in the forward direction due to diffraction as well as a prominent relative maximum at an angle corresponding to the well-known halo occasionally seen around the sun or moon. This halo would not be present in an approximation by equivalent spheres.

Making use of the scattering patterns discussed above for both the visible and infrared portion of the spectrum, a technique was developed for treating the transfer of radiation in cloud layers containing many ice crystals. Based upon a matrix method developed by Twomey, et al. (1966) for problems of the scattering of light by clouds, the technique is capable of treating the radiation thermally emitted by the cloud as well as that coming from sources outside of the cloud.

These methods were then applied to model cirrus clouds in order to study the effects that the various physical characteristics of the clouds have upon the radiation emitted or scattered. For radiation in the 15 μm CO_2 band the results of the computations lead to the conclusions that

cirrus clouds do not radiate as blackbodies but rather at a much lower emissivity. For any cirrus cloud having a thickness of from 1 to 2 kilometers and an ice concentration less than .01 g/m^3, the radiance at the top of the cloud due to self-emission would be less than half of that of a blackbody at the cloud top temperature.

As a practical application of these results, the computations for the model clouds were used in conjunction with radiance measurements made over cirrus clouds by the SIRS-A instrument aboard the Nimbus III spacecraft in order to see if it would be possible to deduce the properties of the cirrus clouds present. As it turned out, only the visible optical thickness could be approximated. The ice concentration and the geometric thickness could not be determined separately. Since the optical thickness is proportional to the product of the ice concentration and the geometric thickness for an assumed ice crystal size, an independent determination of one of these parameters would yield an estimate of the other one. The SIRS-B radiometer has additional channels in the 20μm region of the spectrum, which is a region of moderate water vapor absorption. For this reason, it could be an excellent wavelength to obtain information of the geometric thickness of the cloud layers. The amount of radiation absorbed would depend upon the total path length of water vapor in the cloud encountered by the radiation, which in turn would depend upon the geometric thickness of the cloud.

An important result of these studies is that clouds which are optically thin, though visible from the ground, could have an important effect upon the radiation emitted to space. Many of these clouds may not be visible in satellite photographs.

With the development of the theoretical tools for treating the transfer of radiation in clouds composed of spherical water drops and ice crystals, many studies can be performed to aid in the interpretation of satellite data as well as helping to gain an understanding of the radiative processes at work within real clouds.

CHAPTER SIX

APPLICATION OF THE COMPUTATIONAL METHODS TO FUTURE RESEARCH

A. Computation of the Radiative Transfer in Clouds in Different Spectral Regions

The computations discussed in the previous chapter in connection with the effect that cirrus clouds have on the observed SIRS radiances, have a more general application than presented there. Although the computations were performed in the 11-15 μm portion of the spectrum, they can readily be applied to other spectral regions. While the use of geometric optics and Kirchhoff diffraction was dictated by the ratio of the size of the particles to the wavelengths and by the absorption coefficients involved, other spectral regions may necessitate the use of the more general Mie equation for the determination of the phase function. However, once the phase function is obtained, the general computational methods can be applied.

For example, another very useful computation would be the determination of the degree to which cirrus clouds transmit radiation in the water vapor band at 6.3 μm, one of the most important bands utilized by satellite radiometers. Although middle and lower level clouds appear to behave as blackbodies, high cirrus clouds might not because of their much lower concentration of water vapor. In particular, thin or even moderately thick cirrus clouds could transmit a significant amount. It is generally assumed by many that after correcting for the water vapor transmission in the atmosphere above the clouds, the equivalent blackbody temperature of the radiation emerging upward from the cloud is the same as the cloud top temperature. This will not be the case if radiation is able to penetrate a cloud from lower levels and not be absorbed before leaving the cloud

top. Then, the equivalent blackbody temperature will correspond to a level lower than the cloud top. Such computations as those suggested might help to settle this question.

In the same manner, other spectral regions that are in current use in the various satellite radiation instruments can be studied to see what effect, if any, clouds have on the radiation received by the satellite. One would then be in a better position to interpret the data obtained.

A computation of the transfer of radiation over a sufficiently large number of spectral regions would provide an estimate of the total solar and terrestrial long wave radiation transmitted, reflected, absorbed, or emitted by clouds. One could then study the effects of different cloud conditions and try to determine what cloud parameters appear to have the most influence on the eventual radiation that is transferred by the clouds.

B. Application to a Proposed Earth Radiation Budget Measurement (ERB)

An investigation of the Earth Radiation Budget (ERB) from a satellite has been proposed for the Nimbus F spacecraft by the National Environmental Satellite Center of the ESSA and the Eppley Laboratory, Incorporated. Such an experiment, which is expected to provide the first extensive set of total radiation budget measurements from a satellite, will measure (1) the incoming solar radiation (solar constant and its variance), (2) terrestrially reflected (short wave) radiation, and (3) terrestrially emitted (long wave) radiation. The emitted and reflected radiation from the earth are to be measured in two ways. The first of these is by measuring the total radiation over the entire disk of the earth viewed by the satellite instrument. The second will provide a series of measurements from relatively small areas at a number of zenith and azimuth angles by means of a scanning radiometer. The objective of the second

method is to develop models of the angular variation of the outgoing radiance to permit the determination of the synoptic scale features of the earth's heat budget. By approximating the angular variation of the outgoing radiance, one could estimate the total outgoing heat flux by making a measurement at only one angle. Integration of these results over many synoptic scale areas and comparison with the fluxes determined by the first method will serve as a check on the consistency of the measurement.

The data that will be obtained by the scanning radiometer will be grouped into a number of categories, depending upon the basic earth-atmosphere feature. Important in these groupings will be the general cloud conditions which prevail at the time of the measurement. A reflection category will be decided upon by satellite pictures. Since many sets of observations in the same category will include measurements at the same zenith and azimuth angles, it will be possible to determine the variability of the magnitudes of the angular patterns. The resulting statistically determined patterns for each category will then be used with theoretical models to derive semi-empirical models of the angular radiance.

For the cases when clouds nearly fill the field of view of the radiometers, the theoretical computations provided by the methods discussed in the previous chapters will be used. For example, the solar radiation reflected from clouds will be measured close to or in the principal plane (plane containing the sun, viewed spot, and the satellite) and at other azimuth planes no more than 20° or so from the principal plane. It is in the principal plane that the greatest angular variations are expected. By finding the theoretical cloud model that gives the best

agreement with observations in the principal and nearby planes, one could extend the observations to all azimuth planes. In this way, semi-empirical models of the complete angular variation of the radiance may be developed. Once this is accomplished for all reflection categories, the heat flux from a synoptic scale area could be estimated from only a single measurement.

C. Suggestions for Other Research

The possibility of determining some of the physical properties of clouds from a satellite should be explored. By applying the methods of computation that have been discussed, studies can be made in many spectral regions to learn what cloud properties appear to have the most influence on the radiation field. From this, methods for deducing the cloud properties may be developed. For example, by utilizing two wavelengths, one inside the absorption band (like the oxygen A band at 0.76 μm) and one just outside of it, it should be possible to estimate the optical thickness as well as the altitude of the cloud top. The reflected solar radiation of the wavelength inside the band would be compared with the reflected radiation of the wavelength outside the band; the wavelength outside the band acting as a reference. The ratio of the two measurements would then be a measure of the amount of absorption that has taken place, which should depend upon both the optical thickness of the cloud and the cloud top altitude, if the absorption in the band is a function of altitude. The absolute measurement of the wavelength outside the band would mainly be a function of the optical thickness. It would therefore seem possible to deduce both the optical thickness and the cloud top altitude from these two measurements. Such an attempt at this has already been

made (Saiedy, Jacobowitz, and Wark, 1967). Utilizing pairs of wavelengths in other spectral regions might yield other cloud properties such as its water content, mean particle (water drop or ice crystal) size, etc.

As mentioned in the previous chapter, a measurement of the radiance in the 20 μm water vapor band together with measurements in the 15 μm CO_2 band, such as those used in the SIRS-A instrument, could be used to determine the geometric thickness of a cirrus layer as well as its optical thickness. Radiation in the 20 μm region of the spectrum is absorbed moderately by water vapor present in the cloud. This makes it a particularly useful wavelength region in measuring the geometric thickness. Since the total path length of the radiation in the water vapor is highly dependent upon the geometric thickness, the greater the geometric thickness the more will the radiation be absorbed and therefore the smaller the measured radiance. This wavelength region is included in the SIRS-B channels aboard the Nimbus IV spacecraft. Therefore, since the data will be readily available, it should be a simple matter to test the above ideas.

Since it takes four quantities, in general, to completely describe the polarization of a radiation field, it may be possible to enlarge the number of useful independent measurements for any given set of wavelengths. Such independent data could possibly be used to describe more fully the scattering and absorption properties of a cloud medium. Therefore, inclusion of polarization into the theoretical computations of the transfer of radiation by clouds should be made. Howell and Jacobowitz (to be published) have made some progress along these lines.

The previous suggestions have all been related to the development of methods for deducing the physical characteristics of the cirrus clouds

either by looking at special spectral intervals or including polarization in the measurements. However, in order to properly test the methods developed, one must make extensive measurements of the cloud characteristics and relate them to the radiation measurements.

For example, an experiment should be conducted in which the optical thickness, geometric thickness, altitude of the cloud base and vertical temperature distribution are measured. The optical thickness could be determined by measuring the attentuation of a laser beam that is directed upward from the ground through the cirrus layer to an aircraft above the layer. At the same time another aircraft could measure the thickness of the layer as well as the location of the cloud base. It could also make measurements of the vertical temperature distribution within the cloud.

All of these measurements should be made when the area is being viewed by one or more satellites so that the radiation measured by the satellites can be related to the physical characteristics of the clouds that were measured.

Such measurements as those suggested have already been made to some extent. This "cloud truth" program was conducted from May 4 through May 17, 1970, in which data of the height, temperature, and distribution of the cirrus over the Western United States were collected with the help of many Government agencies. The data obtained are to be compared with the satellite data of all types to learn the proper interpretation of data from all the satellite sensors.

With data from such experiments one could test directly the theoretical predictions presented in this research.

Appendix A

MEAN PATH LENGTH FOR A ONCE-REFRACTED RAY

1. Right Circular Cylinder

We shall derive a relationship for the mean path length encountered by initially unpolarized radiation as it passes through a right circular cylinder, the cylinder being of infinite length so that end effects can be neglected. We shall see later that the results also apply fairly well to finite cylinders as long as their lengths are much greater than their diameters.

Definitions of the quantities that will be used in the derivation follow (see figure A.1).

I_o = energy per unit area normal to the incident radiation.

γ = angle between the incident ray and the axis of the cylinder.

Θ = azimuth angle between the incident ray and the normal at the point of incidence.

ψ = angle between the incident ray and the normal.

ϕ = angle between the refracted ray and the normal.

α = angle between the plane of refraction and a plane cutting the axis of the cylinder at right angles.

a_c = radius of the cylinder.

l = path length of the refracted ray.

ρ = radial polar coordinate.

η = angular polar coordinate.

a = semi-minor axis of an ellipse.

b = semi-major axis of an ellipse.

n = index of refraction of the cylinder.

r_1, r_2 = Fresnel reflection coefficients for polarizations 1 and 2.

$\bar{l}_c$ = mean path length.

$\bar{\bar{l}}_c$ = mean path length for a randomly oriented distribution of cylinders.

A number of equations between some of the above defined quantities can be written down at once. According to Snell's Law we may write,

$$\sin\psi = n \sin\phi \tag{A-1}$$

Geometrical considerations yield

$$\epsilon = \frac{\pi}{2} - \gamma \tag{A-2}$$

$$\cos\psi = \cos\epsilon \cos\theta \tag{A-3}$$

and

$$\sin\alpha = \frac{\sin\epsilon}{\sin\psi} \tag{A-4}$$

The refracted ray lies on the ellipse shown in figure A.1 with semi-minor axis, $a = a_c$ and semi-major axis, $b = a_c/\cos\alpha$.

The equation of such an ellipse in polar coordinates with the origin as indicated in figure A.2 is

$$\frac{(\rho\cos\eta - a)^2}{a^2} + \frac{\rho^2 \sin^2\eta}{b^2} = 1 \tag{A-5}$$

For the refracted ray, $\rho = l$ and $\eta = \phi$, which results in

$$l = \frac{2ab^2\cos^2\phi}{a^2\sin^2\phi + b^2\cos^2\phi} \tag{A-6}$$

Substituting the values of a and b into the above expression we obtain

$$l = \frac{2a_c\sqrt{1-\left(\frac{1-\sin^2\gamma\cos^2\theta}{n^2}\right)}}{1-\frac{\cos^2\gamma}{n^2}} \qquad \text{(A-7)}$$

which gives us the path length as a function of the angles θ and γ for a cylinder of a given radius and index of refraction.

The ratios of the amplitudes of the waves reflected to the amplitude of the incident wave (Fresnel reflection coefficients) as obtained from electromagnetic theory are given by the relations

$$r_1 = \frac{\cos\psi - n\cos\phi}{\cos\psi + n\cos\phi} \qquad \text{(A-8)}$$

and

$$r_2 = \frac{n\cos\psi - \cos\phi}{n\cos\psi + \cos\phi} \qquad \text{(A-9)}$$

for the two polarizations.

As a result, $(1-r_1^2)$ and $(1-r_2^2)$ are the fractions of the incident radiation which will enter the cylinder. Figure A.3 displays these fractions as a function of ψ for n = 1.32.

The energy incident upon a unit length of the cylinder having angles between θ and $\theta + d\theta$ is

$$dI = I_0(a_c\cos\theta\, d\theta) \qquad \text{(A-10)}$$

while the energy that actually enters the cylinder is

$$dI' = dI\left(\tfrac{1}{2}\right)\left[(1-r_1^2)+(1-r_2^2)\right] \qquad \text{(A-11)}$$

Consequently, the mean path length of the radiation in the cylinder is given by

$$\bar{l}_c = \frac{\int l\, dI'}{\int dI'} = \frac{I_0\int_{-\frac{\pi}{2}}^{\frac{\pi}{2}} \frac{l}{2}\left[(1-r_1^2)+(1-r_2^2)\right]a_c\cos\theta\, d\theta}{I_0\int_{-\frac{\pi}{2}}^{\frac{\pi}{2}} \frac{1}{2}\left[(1-r_1^2)+(1-r_2^2)\right]a_c\cos\theta\, d\theta} \qquad \text{(A-12)}$$

According to figure A.3, $(1-\rho_1^2) \simeq (1-\tilde{\rho}) \simeq 1$ over most of the range of incident angles. Therefore, to a high degree of approximation,

$$\bar{l}_c = \frac{\int_0^{\pi/2} l \cos\theta \, d\theta}{\int_0^{\pi/2} \cos\theta \, d\theta}$$

or finally

$$\bar{l}_c = a_c n \left[\frac{\sqrt{n^2-1}}{n^2 - \cos^2\gamma} + \frac{1}{\sin\gamma} \sin^{-1}\left(\frac{\sin\gamma}{\sqrt{n^2-\cos^2\gamma}} \right) \right] \qquad \text{(A-13)}$$

The special case for radiation incident at right angles to the cylindrical axis is obtained by setting γ equal to 90° in the above expression. This gives us

$$\bar{l}_c(\gamma = 90°) = a_c \left[\frac{\sqrt{n^2-1}}{n} + n \sin^{-1}\left(\frac{1}{n}\right) \right] \qquad \text{(A-14)}$$

In the limit that γ approaches zero (grazing incidence) the mean path length is given by

$$\bar{l}_c(\gamma \to 0°) \longrightarrow \frac{2 a_c n}{\sqrt{n^2-1}} \qquad \text{(A-15)}$$

This limit approaches the value 3.06 a_c for the case that n = 1.32. Even if the cylinder is of finite length, such a path length could be realized, as long as the cylinder is sufficiently long to contain the path of the refracted ray. However as n gets closer and closer to 1, $\bar{l}_c(\gamma \to 0)$ increases without limit.

For a distribution of cylinders in random orientation, the mean path length is given by

$$\bar{\bar{l}}_c = \frac{\int_0^{\pi} \bar{l}_c \sin\gamma \, d\gamma}{\int_0^{\pi} \sin\gamma \, d\gamma} \qquad \text{(A-16)}$$

Since the numerator in the expression above is not readily integrable, one must approximate it numerically.

2. Sphere

The mean path length for a sphere can be similarly derived. The definitions of the quantities that will be used in this derivation follow (see figure A.4).

I_o = energy per unit area normal to the incident radiation.

θ = angle between the incident ray and the normal to the sphere at the point of incidence.

ϕ = angle corresponding to θ for the refracted ray.

l = path length of the refracted ray.

a_s = radius of the sphere.

n = index of refraction.

$\bar{l}_s$ = mean path length.

As before we can write down a number of equations between some of the above quantities. They are

$$\sin\theta = n \sin\phi \tag{A-17}$$

and

$$l = 2a_s \cos\phi \tag{A-18}$$

Combining equations (A-17) and (A-18) we obtain

$$l = \frac{2a_s}{n}\sqrt{n^2 - \sin^2\theta} \tag{A-19}$$

The energy incident upon the sphere having angles of incidence between θ and $\theta + d\theta$ is

$$dI = I_0 (2\pi q_s \sin\theta \cos\theta \, d\theta) \tag{A-20}$$

Neglecting the effect of the reflection as before, the mean path length is given by

$$\bar{l}_s = \frac{\int l \, dI}{\int dI}$$

$$= \frac{4 q_s}{3 n} \left[n^3 - (n^2 - 1)^{\frac{3}{2}} \right] \tag{A-21}$$

Appendix B

ANGULAR PATTERN OF RADIATION REFLECTED FROM A CYLINDER

The angular pattern of radiation reflected from the surface of a cylinder will be derived for the special case that the incident radiation is unpolarized and its direction of propagation is at a right angle with the axis of the cylinder. The intensity of the incident beam will be denoted by I_0, while τ will be the angle it makes with the tangent at the point of incidence and θ will be the angle between the reflected and incident rays (see figure B.1). Let h represent the distance along the cylinder from an arbitrary origin.

A finite pencil of radiation will then be characterized by $d\tau$ and dh. Therefore, the flux of energy (energy per unit time) in an incident pencil, d^2E, can be written

$$d^2E = I_0 (a_c \sin\tau \, d\tau \, dh) \tag{B-1}$$

After scattering from the cylinder, the energy is reduced to d^2E', where

$$d^2E' = \frac{1}{2}(r_1^2 + r_2^2) d^2E \tag{B-2}$$

r_1 and r_2 are the Fresnel reflection coefficients corresponding to polarizations 1 and 2. The scattered radiation spreads out into an area, d^2A given by

$$d^2A = r \, d\theta \, dh \tag{B-3}$$

where r is the distance from the axis of the cylinder.

By definition, the reflected intensity, I , is the ratio of the scattered flux, d^2E' , in a pencil of radiation to its cross-sectional area, d^2A . Therefore, we have

$$I = \left(\frac{r_1^2 + r_2^2}{2}\right) I_o \frac{q_c \sin\tau \, d\tau \, dh}{r \, d\theta \, dh}$$

$$= \frac{q_c}{r}\left(\frac{r_1^2 + r_2^2}{2}\right) I_o \, D \qquad \text{(B-4)}$$

where

$$D = \sin\tau \frac{d\tau}{d\theta} \qquad \text{(B-5)}$$

Since $\theta = 2\tau$, equation (B-5) simplifies to

$$D = 1/2 \sin\frac{\theta}{2} \qquad \text{(B-6)}$$

In summary, the angular pattern of the reflected radiation is given by the expression,

$$I = I_o \frac{q_c}{r}\left(\frac{r_1^2 + r_2^2}{4}\right) \sin\frac{\theta}{2} \qquad \text{(B-7)}$$

Appendix C

CONTRIBUTIONS OF END EFFECTS TO THE KIRCHHOFF DIFFRACTION PATTERN FROM RANDOMLY ORIENTED CYLINDERS

The Kirchhoff diffraction pattern for a distribution of cylinders in random orientation was derived in Chapter Three with the approximation that diffraction from the end faces of the cylinder may be neglected. While this approximation would be a very good one for cylinders whose lengths were many times their diameters, the same might not be true for shorter cylinders. As we have seen in Chapter Three, Kirchhoff diffraction depends strongly upon the area of the body causing the diffraction which is projected onto a plane of the incident wave front (shadow area). The end faces of long cylinders in random orientation would have projected areas that would be a small fraction of the total projected area, while in the case of short cylinders, this fraction would not be so negligible.

The contribution that the end faces make to the diffraction pattern can be estimated by considering a somewhat different problem. Imagine that each cylinder is replaced by a body of rectangular shape having a length equal to the length of the original cylinder and having a width and a breadth both equal to the diameter of the cylinder. Also consider that each of the rectangular bodies is so oriented that only one of its principal faces would have a projection upon the plane of the incident wave front (see figure C.1). The choice of this orientation will guarantee that the projected area of the face of the rectangular body is exactly equal to that of the replaced cylinder. Aside from this restriction, the rectangular bodies may have a random orientation. As a result, the Kirchhoff diffraction pattern for this distribution with the end faces neglected will be identical to the patterns obtained for the cylinders with their end faces also neglected.

Therefore, a comparison of the diffraction pattern for the rectangular body which includes the end faces with the pattern when they are neglected is expected to be a reasonable estimate of what would also result for the cylinders.

Following the notation used in Chapter Three, the length of the rectangular body will be equal to ℓ and its width and breadth will both equal $2a_c$. While the length of the projection of the cylinder was previously approximated by $\ell \sin\gamma$, the exact length of the projection of the rectangular body is given by H, where

$$H = \ell \sin\gamma + 2a_c |\cos\gamma| \tag{C-1}$$

Proceeding with the same line of reasoning as in Chapter Three, there is the result,

$$\langle (GD)^2 \rangle = \frac{16}{\ell^4 \sin^4\theta} M \sin^2 N \tag{C-2}$$

where

$$M = \frac{\ell H}{2} \sin\theta \tag{C-3}$$

and

$$N = k a_c \sin\theta \tag{C-4}$$

or

$$\langle (GD)^2 \rangle = \frac{8H q_c^2}{k \sin\theta} E^2(k q_c \sin\theta) \qquad \text{(C-5)}$$

which is valid for angles θ , such that $\frac{kH}{2} \sin\theta >> 1$

This expression is identical to the one derived for the cylinders except that l is replaced by H. Averaging equation (C-5) over all γ ,

$$\langle \overline{(GD)^2} \rangle = \frac{8 q_c^2}{k \sin\theta} E^2(k q_c \sin\theta)\left(l \overline{\sin\gamma} + 2 q_c \overline{|\cos\gamma|}\right) \qquad \text{(C-6)}$$

It can be readily shown that,

$$\overline{\sin\gamma} = \frac{\pi}{4} \qquad \text{(C-7)}$$

and

$$\overline{|\cos\gamma|} = \frac{1}{2} \qquad \text{(C-8)}$$

Substituting equations (C-7) and (C-8) into (C-6) and letting $b = \frac{l}{q_c}$,

$$\langle \overline{(GD)^2} \rangle = \frac{2\pi l q_c^2}{k \sin\theta} E^2(k q_c \sin\theta)\left(1 + \frac{4}{\pi b}\right) \qquad \text{(C-9)}$$

Finally making use of equation (C-15), the diffracted intensity versus θ results. It is given by

$$I_n(\theta) = I_{no}(\theta)\left(1 + \frac{4}{\pi b}\right) \qquad \text{(C-10)}$$

where

$$I_{no}(\theta) = \frac{I_0}{n^2} \frac{k l q_c^2}{2\pi \sin\theta} E^2(k q_c \sin\theta) \qquad \text{(C-11)}$$

$I_{no}(\theta)$ is the result for the intensity when the ends are neglected. It is therefore clear that the shape of the angular pattern remains the same; only the magnitude is changed by the factor, $(1 + \frac{4}{\pi b})$.

Equation (C-10) may also be written,

$$I_r(\theta) = \frac{I_0}{r^2} \frac{k\, l_{eff}\, a_s^2}{2\pi \sin\theta} E^2(k a_c \sin\theta) \qquad (C\text{-}12)$$

where

$$l_{eff} = l\left(1 + \frac{4}{\pi k}\right) \qquad (C\text{-}13)$$

This shows that inclusion of end effects is equivalent to increasing the value of l to produce an effective l .

The radii of the equivalent spheres may now be found from the expression,

$$\begin{aligned} \pi a_s^2 &= 2\overline{a_c H} \\ &= 2a_c\left(l\overline{\sin\gamma} + 2a_c\overline{|\cos\gamma|}\right) \qquad (C\text{-}14) \\ &= \frac{a_c l \pi}{2}\left(1 + \frac{4}{\pi k}\right) \end{aligned}$$

or

$$a_s = \sqrt{\frac{a_c l}{2}\left(1 + \frac{4}{\pi k}\right)} \qquad (C\text{-}15)$$

The smooth curve derived from (C-10) is given by (see Chapter Three)

$$\tilde{I}_c(\theta) = \frac{I_0}{r^2} \frac{k a_c}{4\pi k} \frac{1}{\sin^3\theta}\left(1 + \frac{4}{\pi k}\right) \qquad (C\text{-}16)$$

and that for the equivalent sphere previously derived is given by

$$\tilde{I}_s(\theta) = \frac{I_0}{r^2} \frac{1}{\pi} \frac{a_s}{k} \frac{1}{\sin^3\theta} \qquad (C\text{-}17)$$

Substituting equation (C-15) into (C-17),

$$\tilde{I}_s(\theta) = \frac{I_0}{r^2} \frac{1}{\pi} \frac{a_c\sqrt{\frac{1}{2}\left(1 + \frac{4}{\pi k}\right)}}{k} \frac{1}{\sin^3\theta} \qquad (C\text{-}18)$$

The ratio, $\tilde{I}_c(\theta)/\tilde{I}_s(\theta)$ is then given by

$$\frac{\tilde{I}_c(\theta)}{\tilde{I}_s(\theta)} = \sqrt{\frac{b}{\delta}\left(1+\frac{4}{\pi b}\right)} \qquad \text{(C-19)}$$

For very long bodies where $b >> 1$, equation (C-19) reduces to the expression found when the ends were neglected.

For small θ, we have similar to equation (3-46),

$$\tilde{I}_c(0) = \frac{I_0}{\lambda^2}\,\frac{2}{3\pi^2}\,k^2 b_{eff}^2\, a_c^4 \cdot (1.25) \qquad \text{(C-20)}$$

where

$$b_{eff} = \frac{l_{eff}}{a_c} = b\left(1+\frac{4}{\pi b}\right) \qquad \text{(C-21)}$$

Also, similar to equation (3-50)

$$\tilde{I}_s(0) = \frac{I_0}{\lambda^2}\,\frac{k^2 b_{eff}^2\, a_c^4}{16} \cdot (1.25) \qquad \text{(C-22)}$$

Therefore,

$$\frac{\tilde{I}_c(0)}{\tilde{I}_s(0)} = \frac{32}{3\pi^2} \qquad \text{(C-23)}$$

which is the ratio previously derived when the ends were not included.

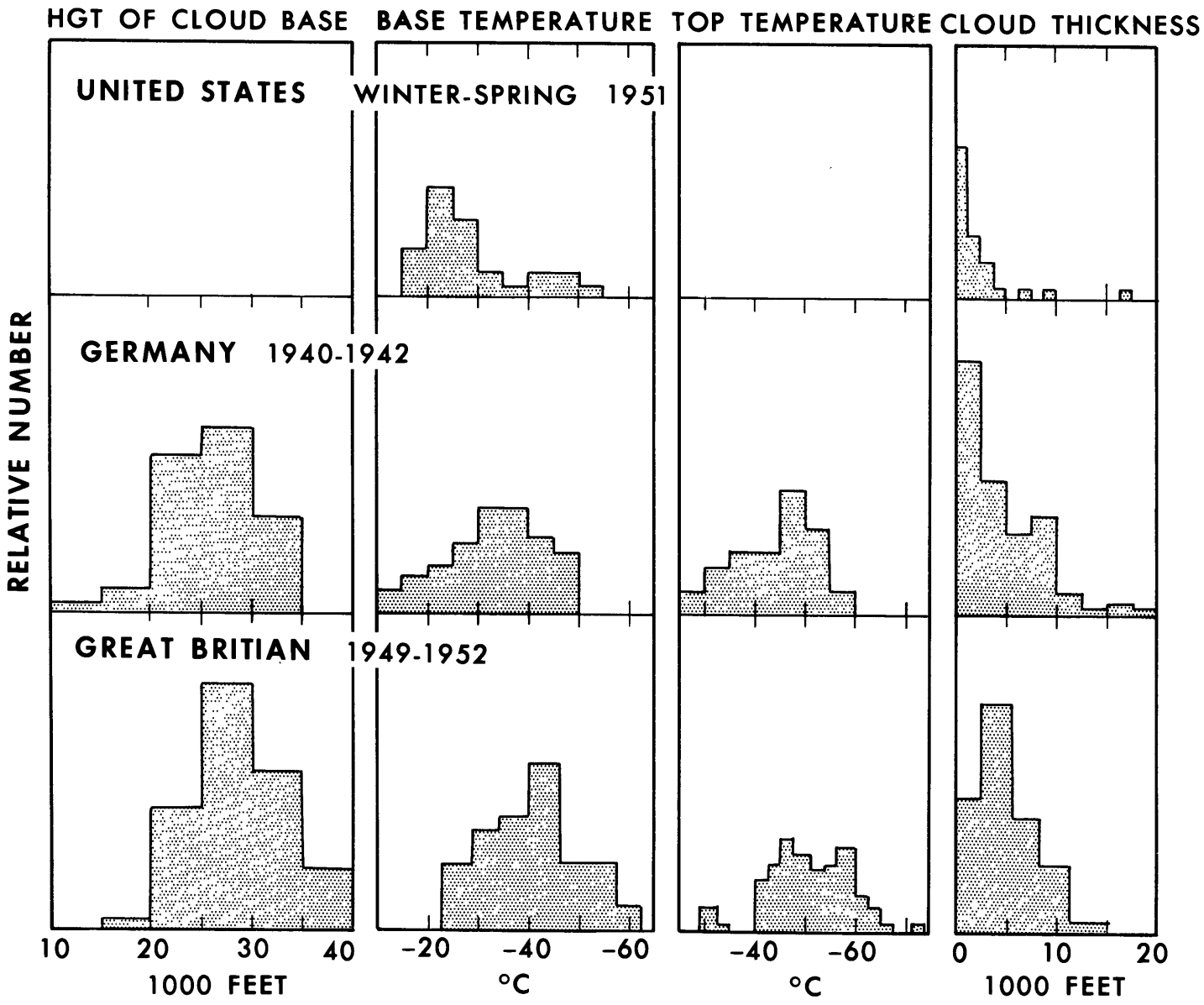

Figure 2.1--Summary of cirrus cloud observations (after Kampe and Weickmann, 1957).

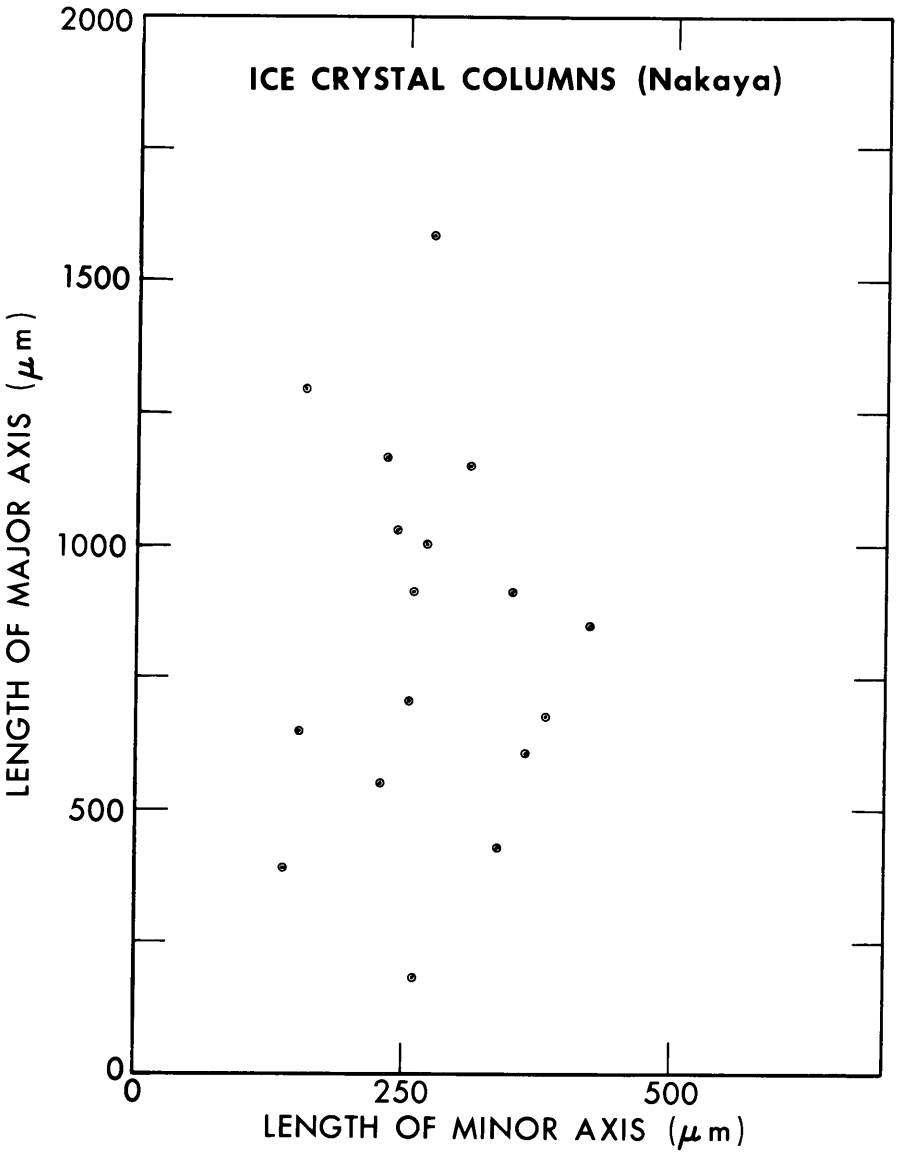

Figure 2.2--Lengths of major and minor axes of ice crystal columns collected by Nakaya.

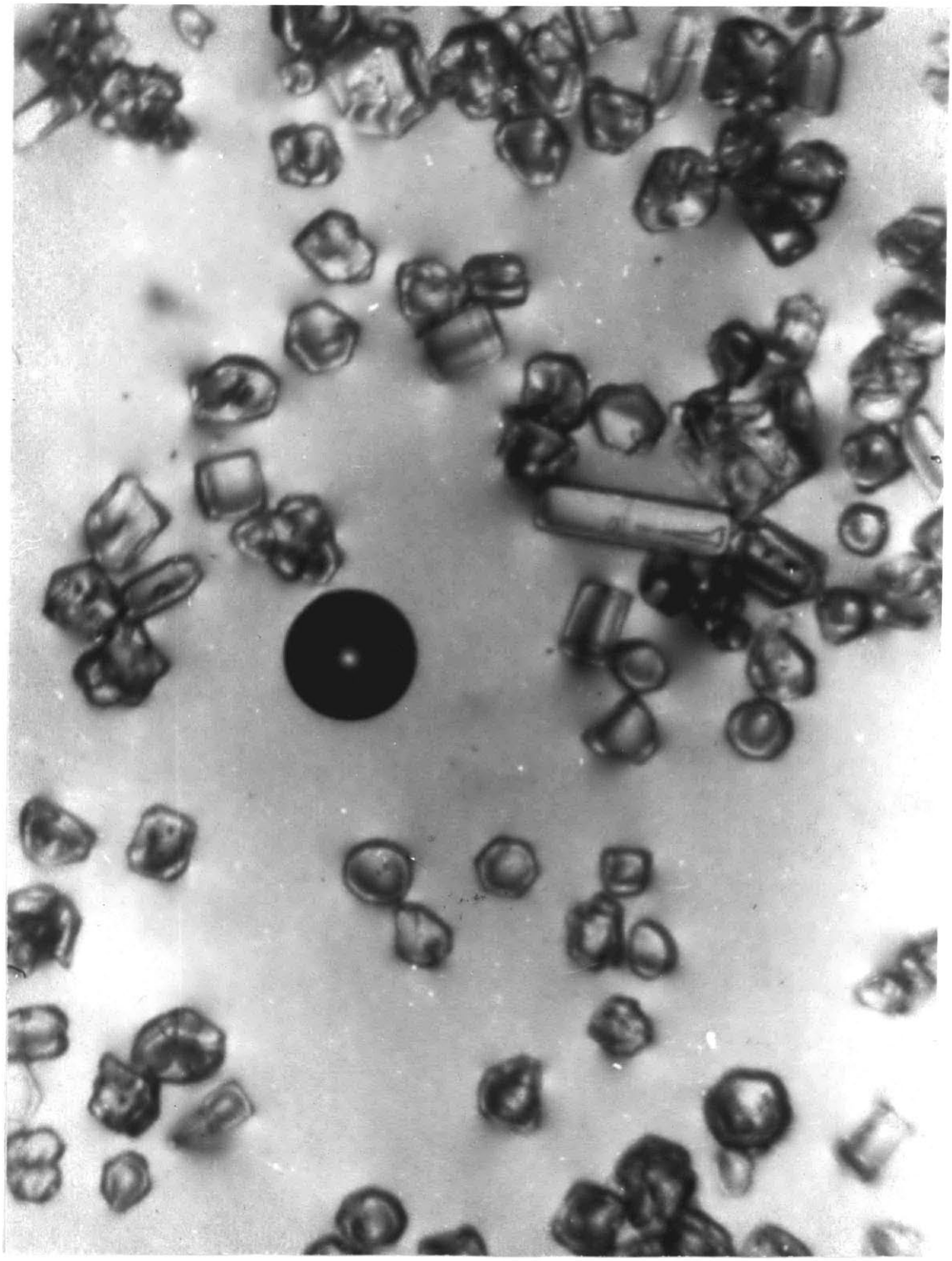

Figure 2.3--Ice crystals in a cirrostratus cloud at -47°C. (photo by Weickmann)

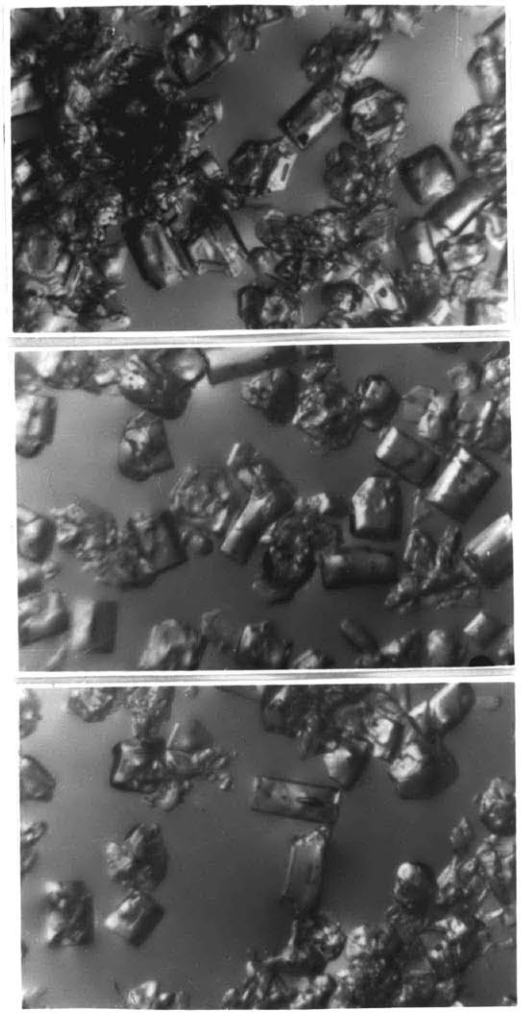

Figure 2.4--Ice crystals in a cirrostratus cloud at -26°C. (photo by Weickmann)

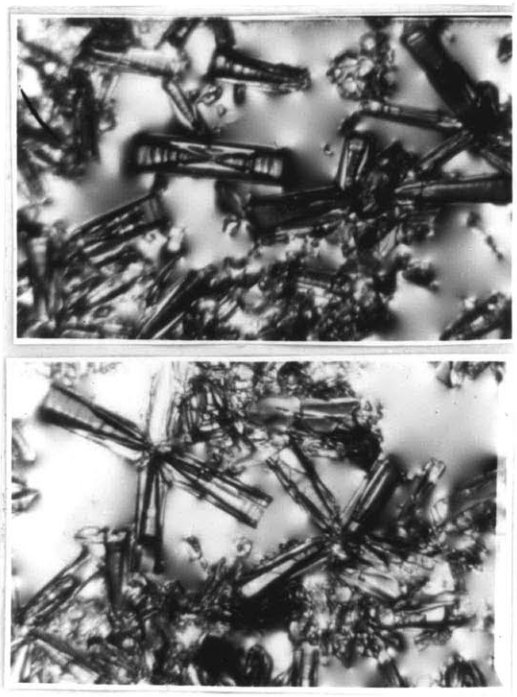

Figure 2.5--Ice crystals in a cirrocumulus bank at -37°C to -47°C. (photo by Weickmann)

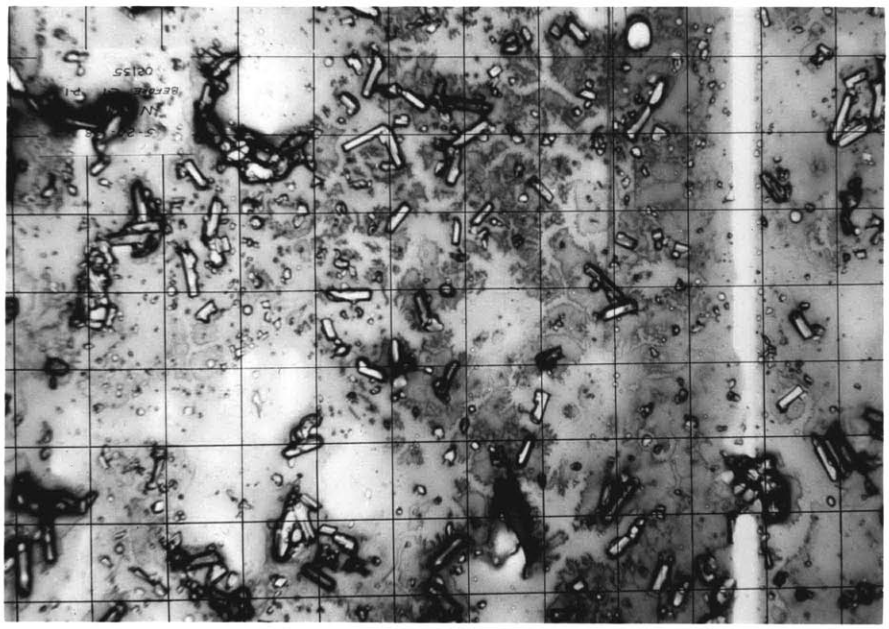

Figure 2.6--Ice crystals collected aboard an X-21 A Laminar Flow Control Aircraft (photo by Mee and Williamson, 1965).

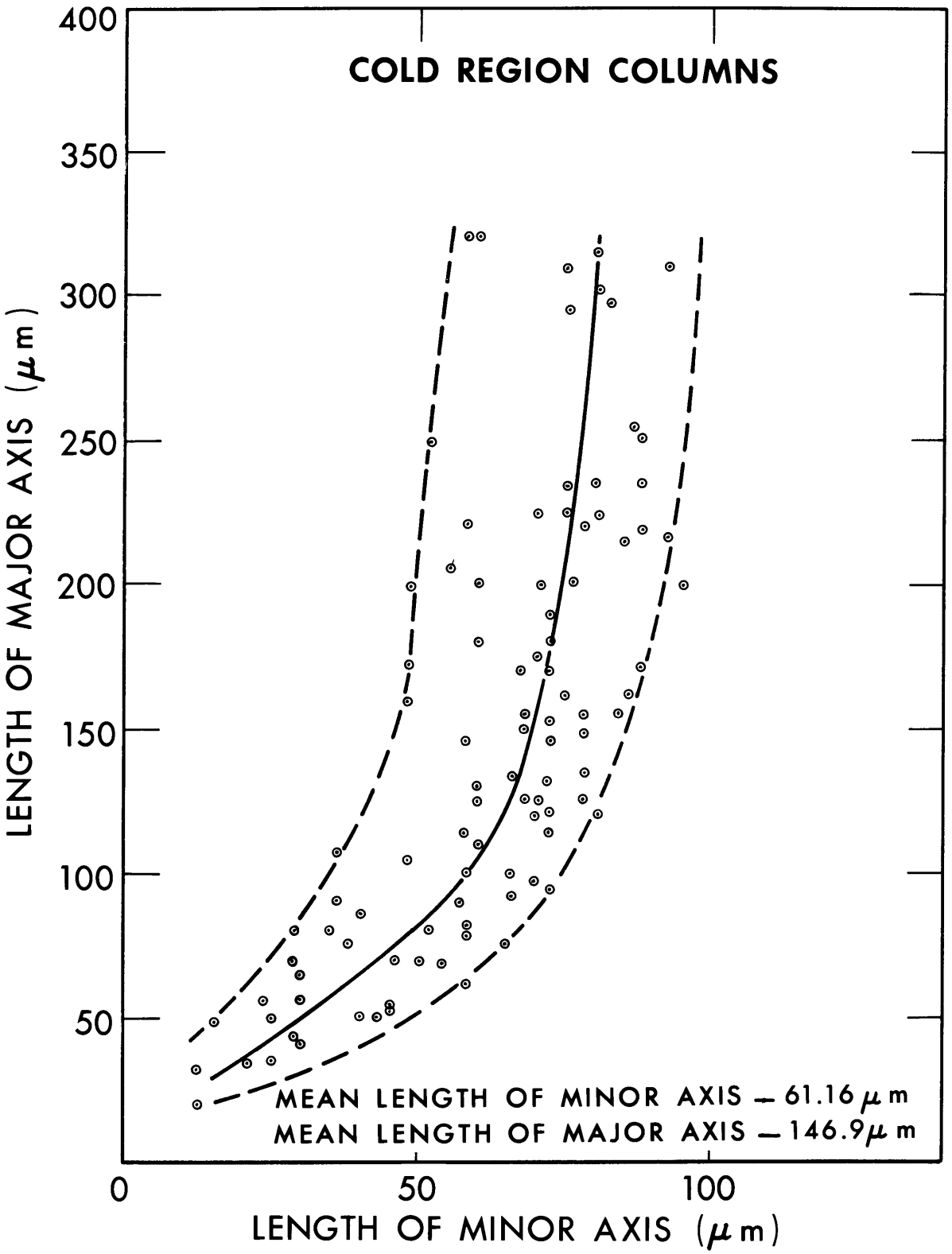

Figure 2.7--Lengths of major and minor axes of "cold region columns." Dashed lines give the approximate mean curve and boundary limits (after Ono, 1969).

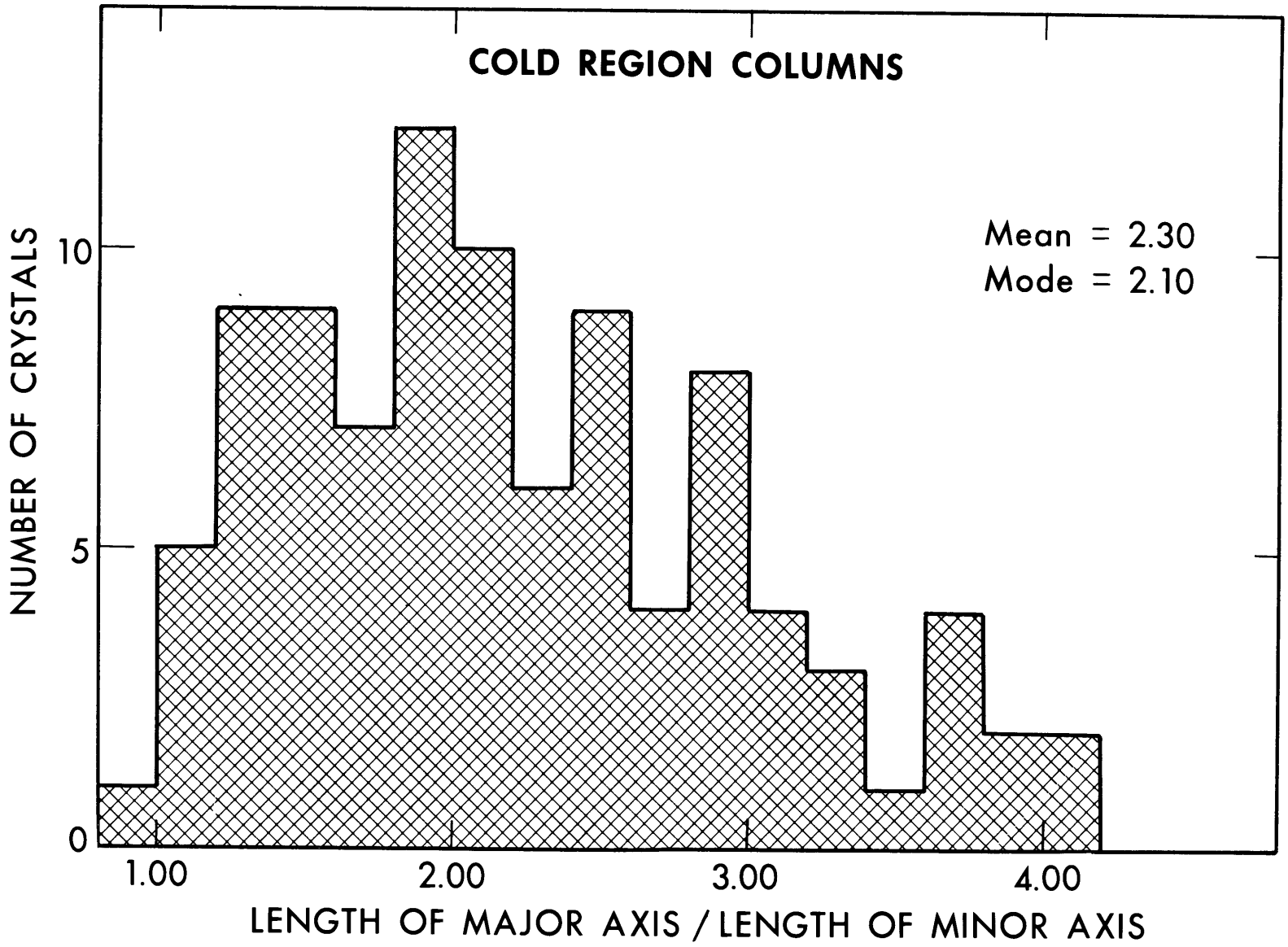

Figure 2.8--Histogram of the ratios of the lengths of the major to that of the minor axis of the crystals plotted in figure 2.7.

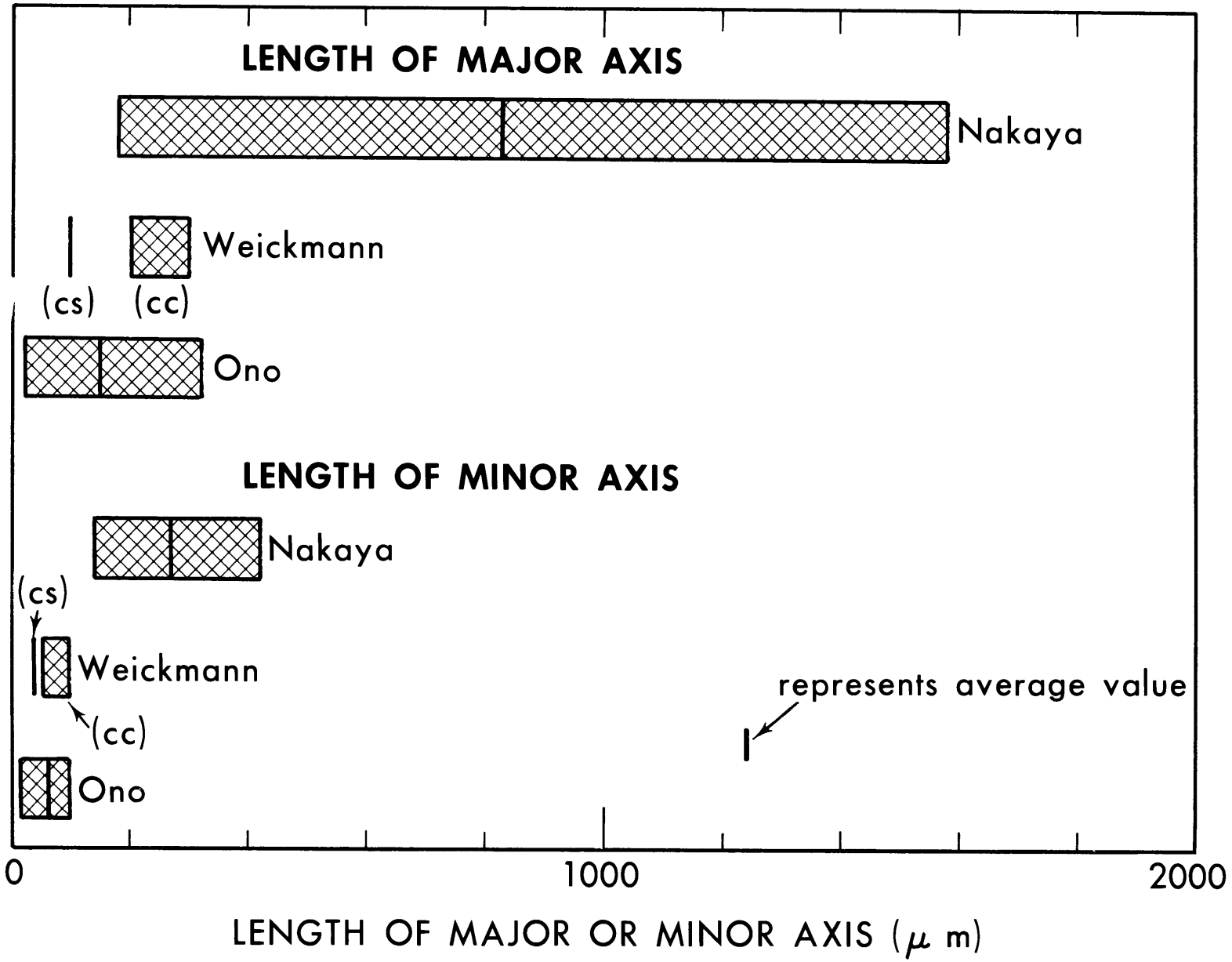

Figure 2.9--Comparison of the lengths of the axes of the crystals collected by Nakaya, Weickmann, and Ono.

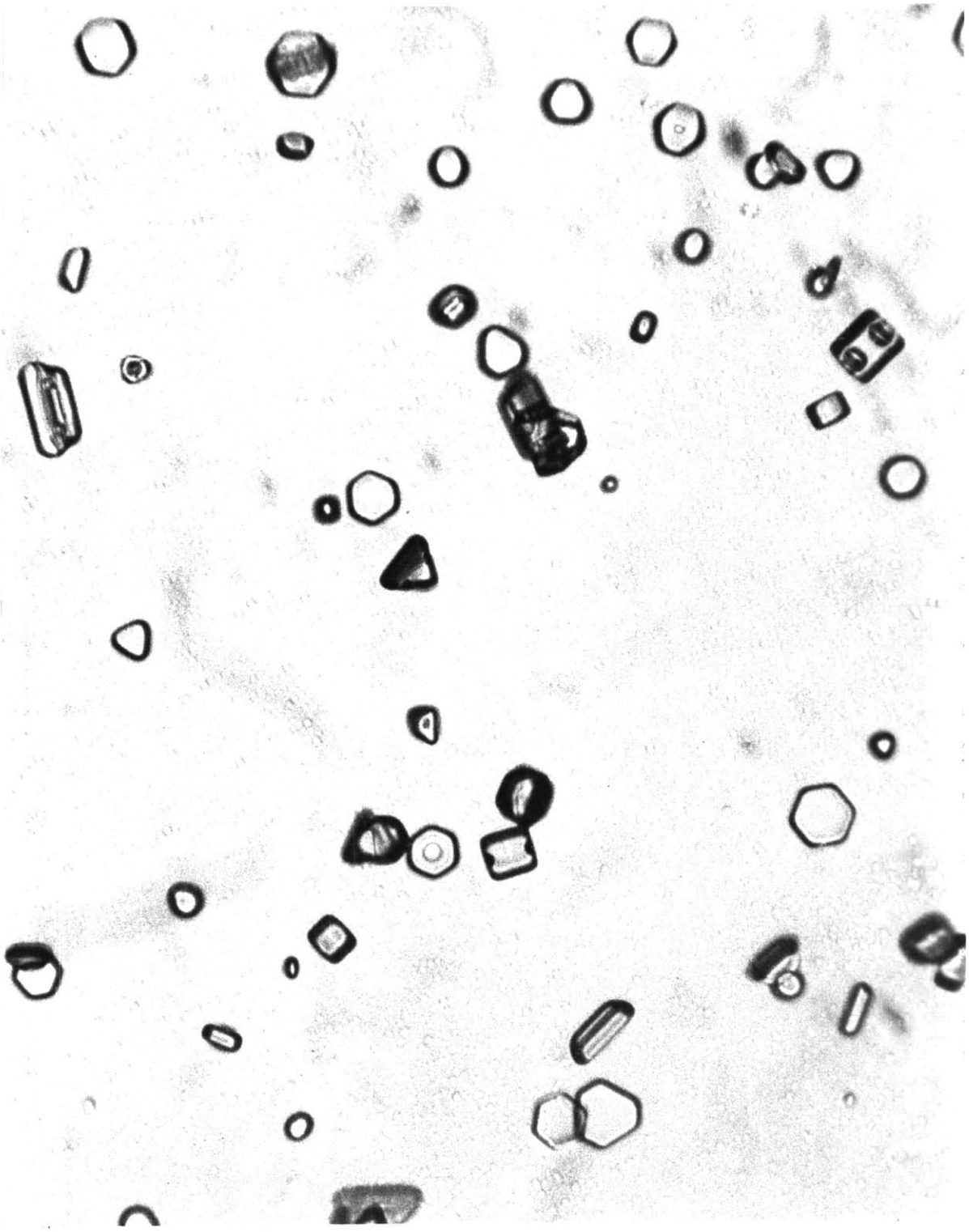

Figure 2.10--Ice crystals grown at water saturation at a temperature of -3.3°C (photo by Kampe, Weickmann, and Kelly, 1951).

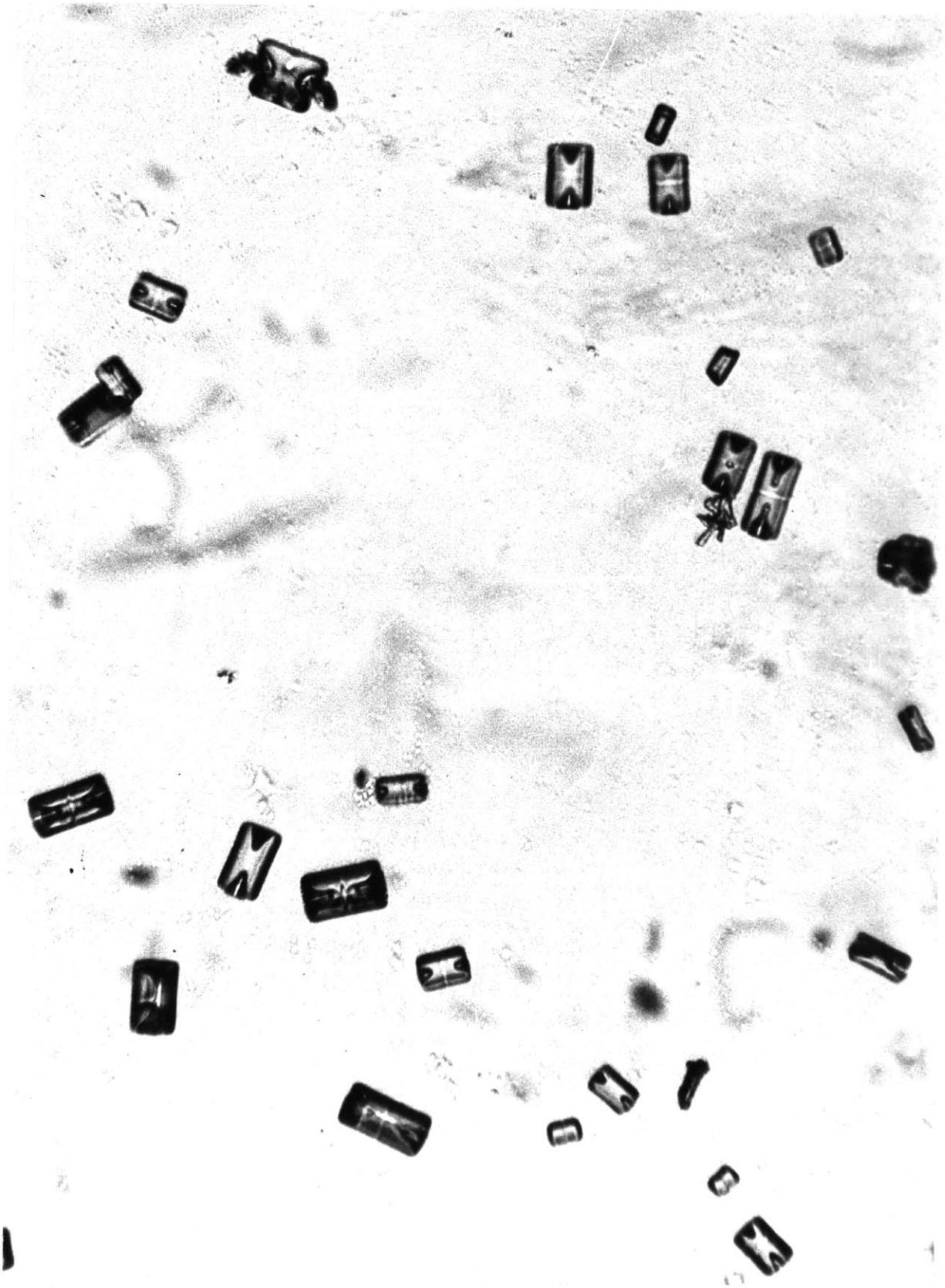

Figure 2.11--Ice crystals grown at water saturation at a temperature of -7.5°C (photo by Kampe, Weickmann, and Kelly, 1951).

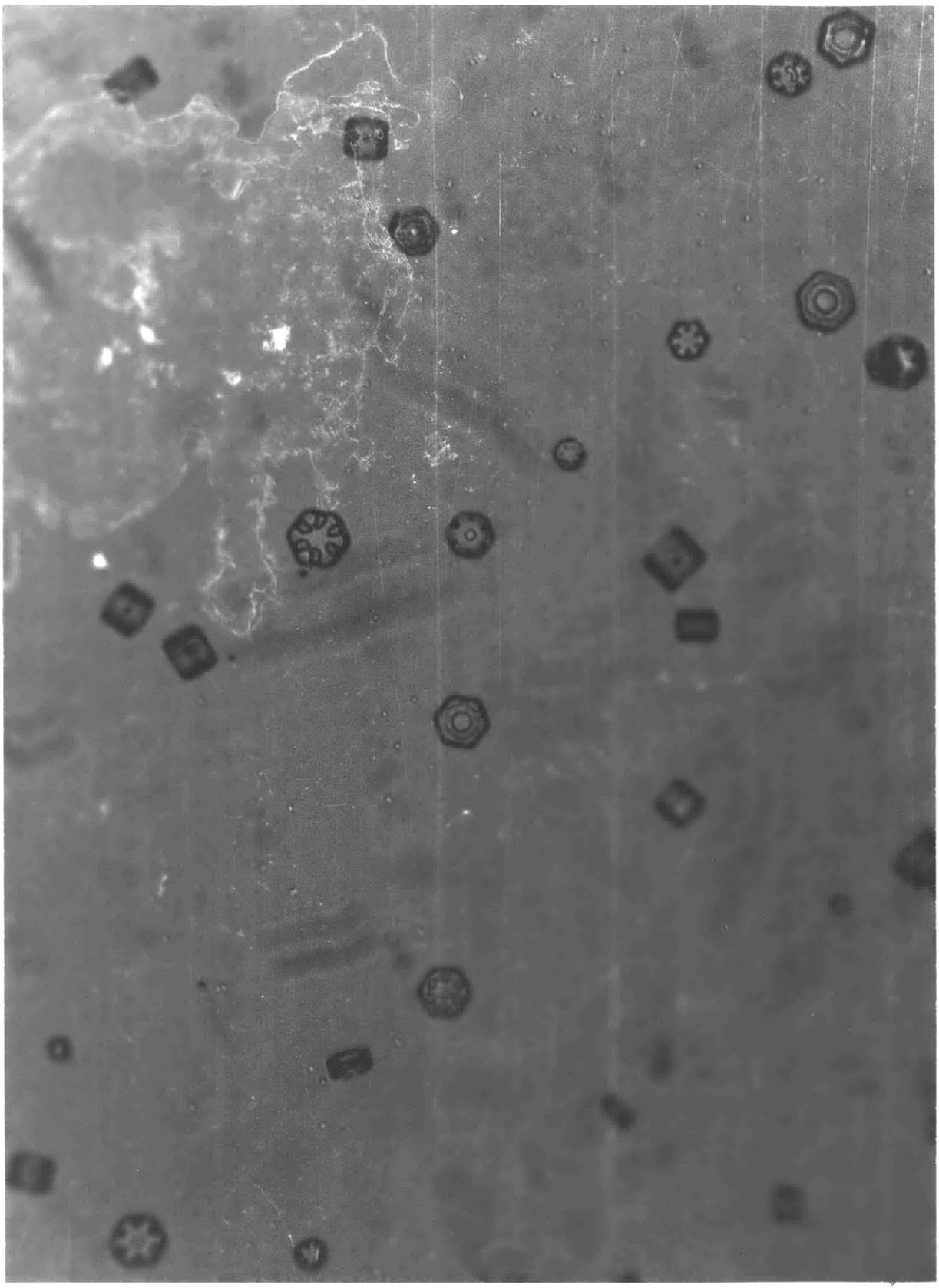

Figure 2.12--Ice crystals grown at water saturation at a temperature of -9°C (photo by Kampe, Weickmann, and Kelly, 1951).

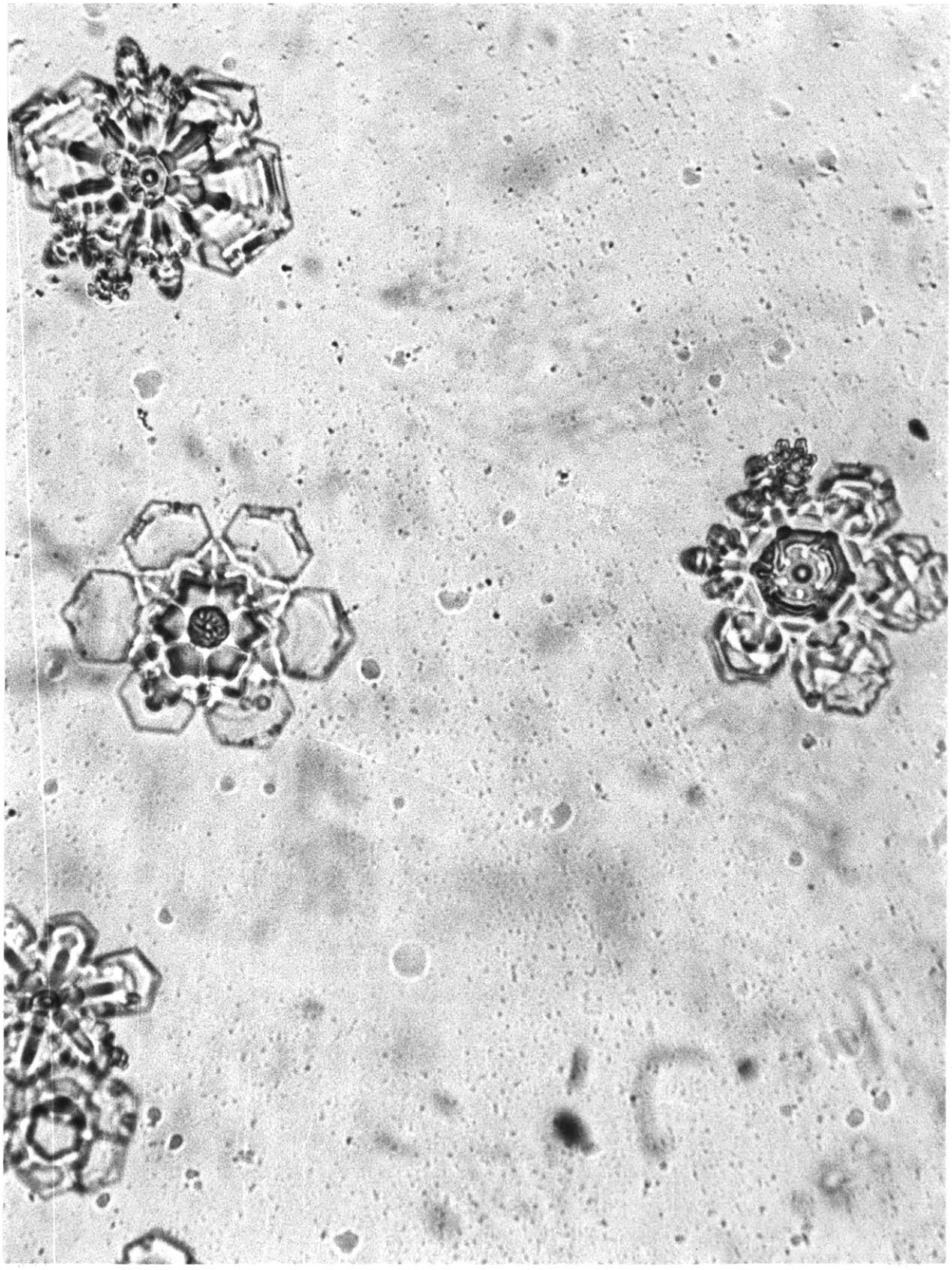

Figure 2.13--Ice crystals grown at water saturation at a temperature of -18°C (photo by Kampe, Weickmann, and Kelly, 1951).

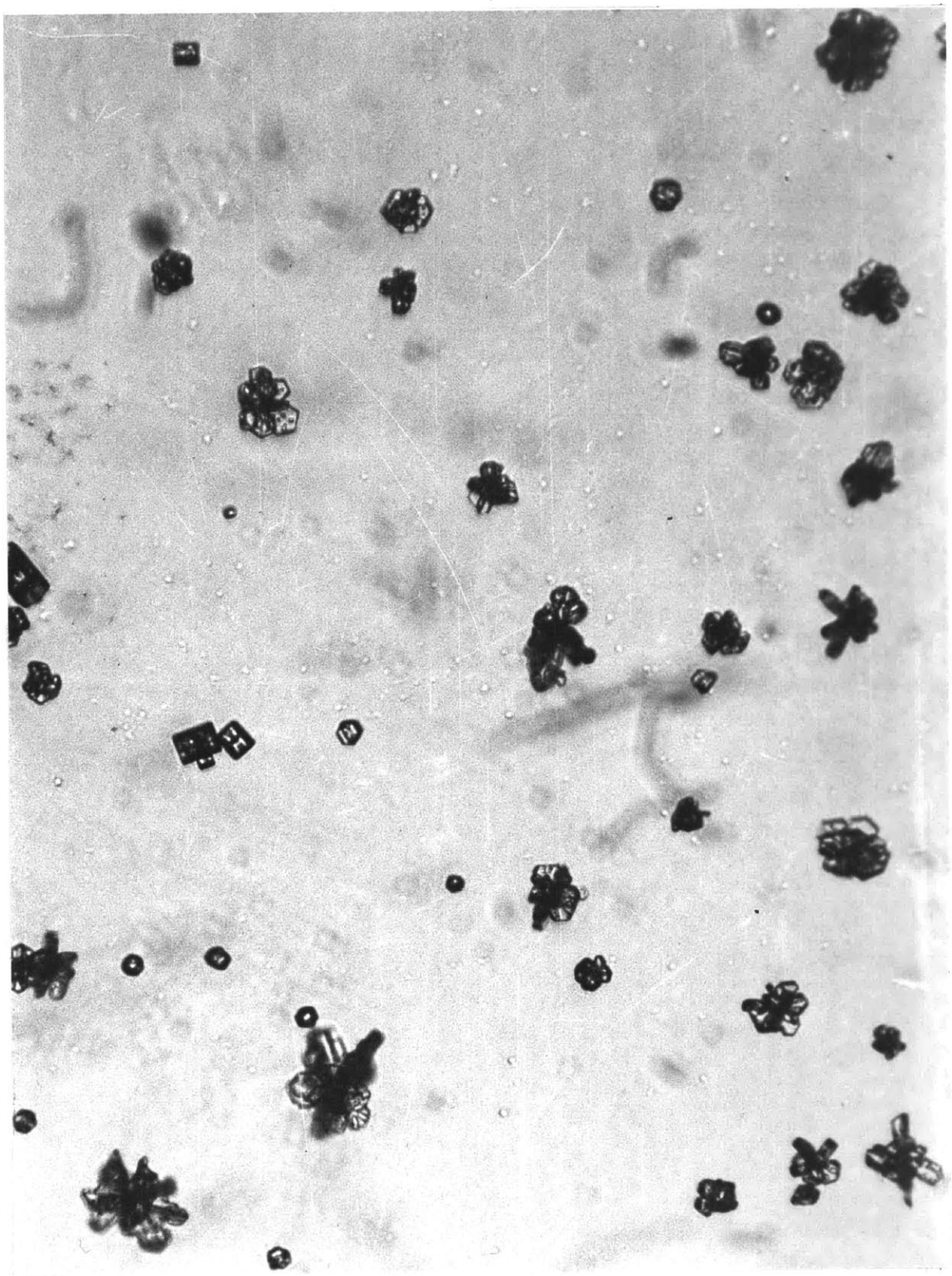

Figure 2.14--Ice crystals grown at water saturation at a temperature of -29°C (photo by Kampe, Weickmann, and Kelly, 1951).

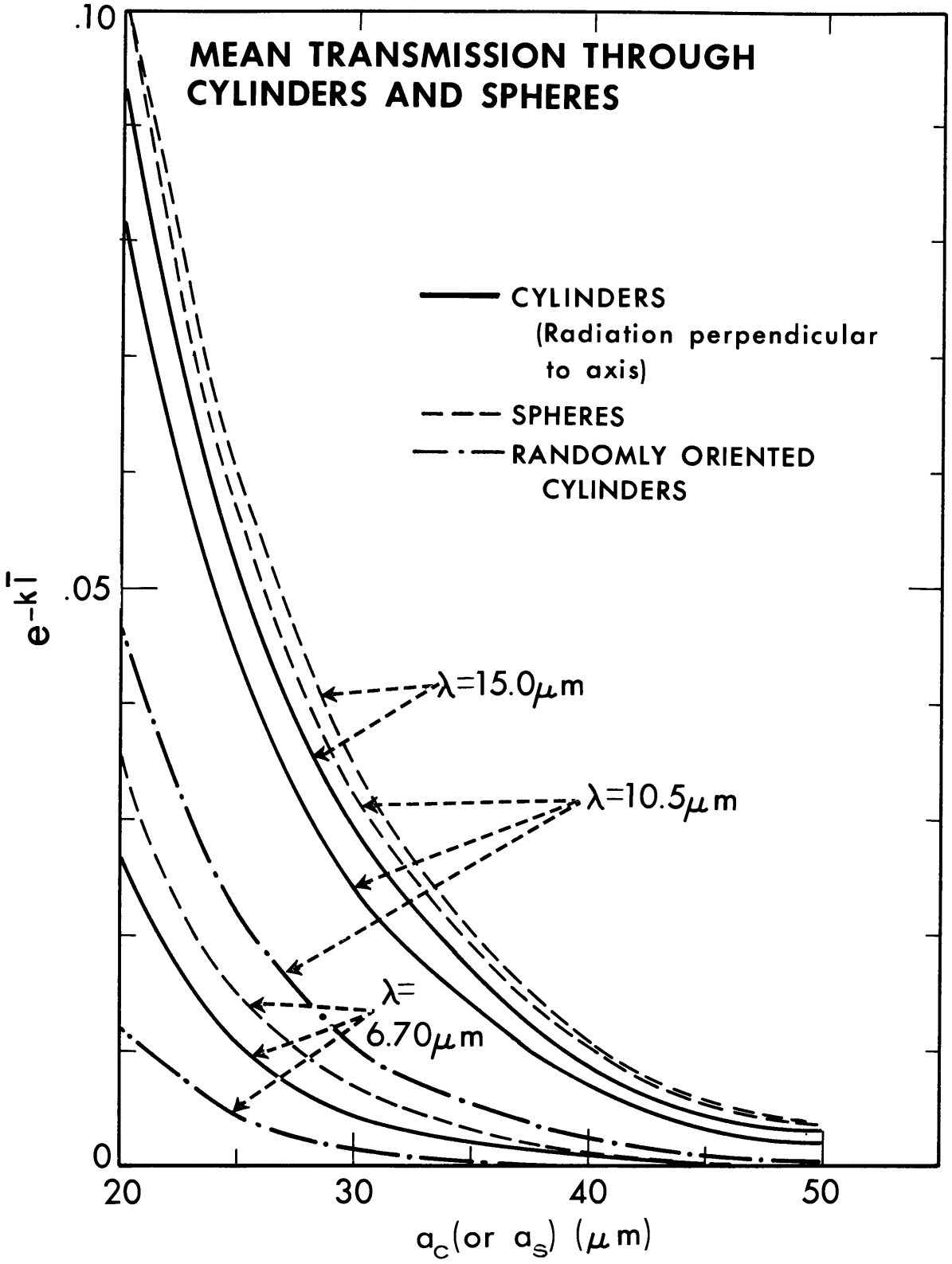

Figure 3.1--Mean transmissivities through cylinders and spheres, $e^{-k\bar{l}}$, for the wavelengths indicated. The index of refraction n = 1.32.

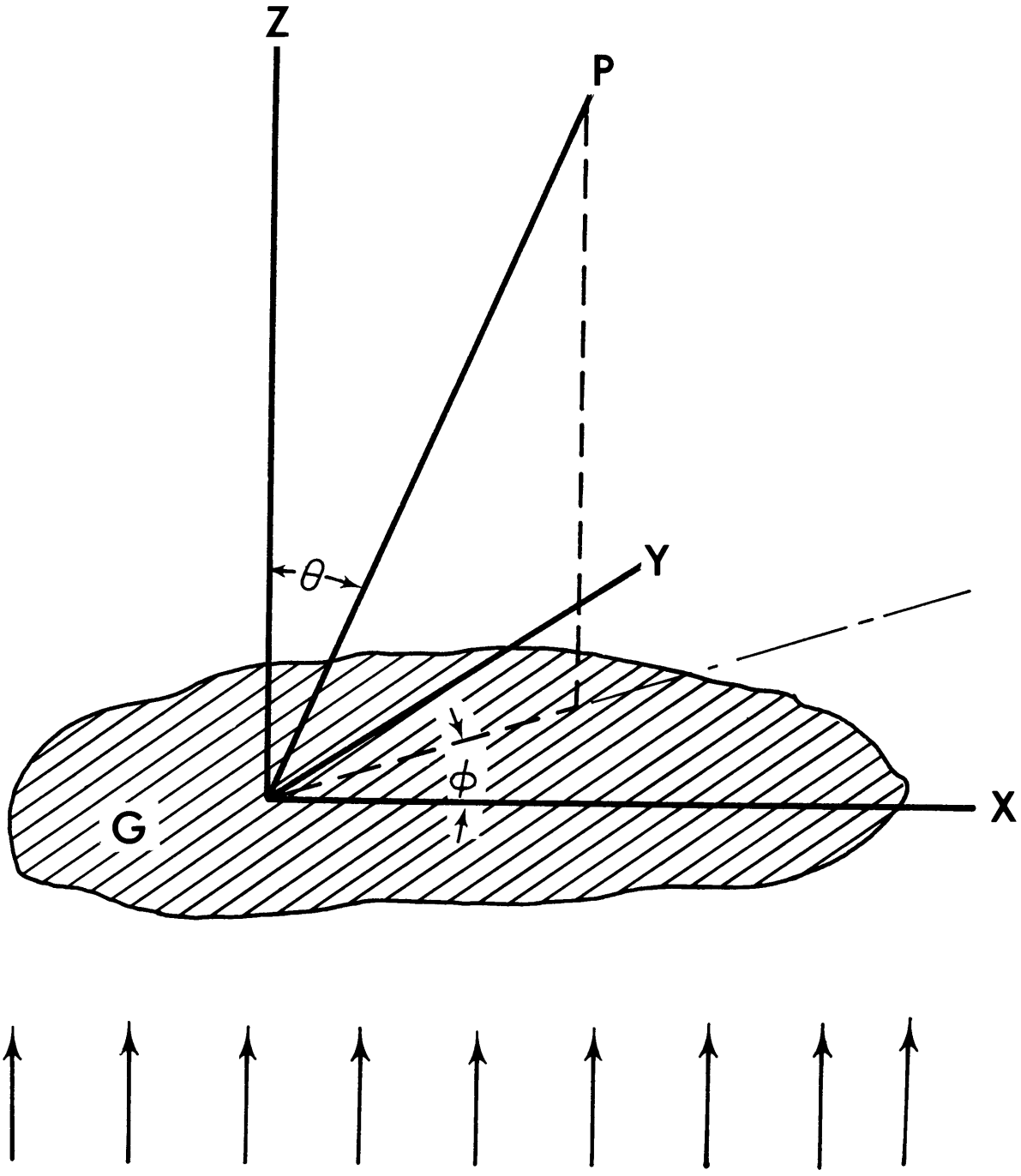

Figure 3.2--Geometry for diffraction by a large body.

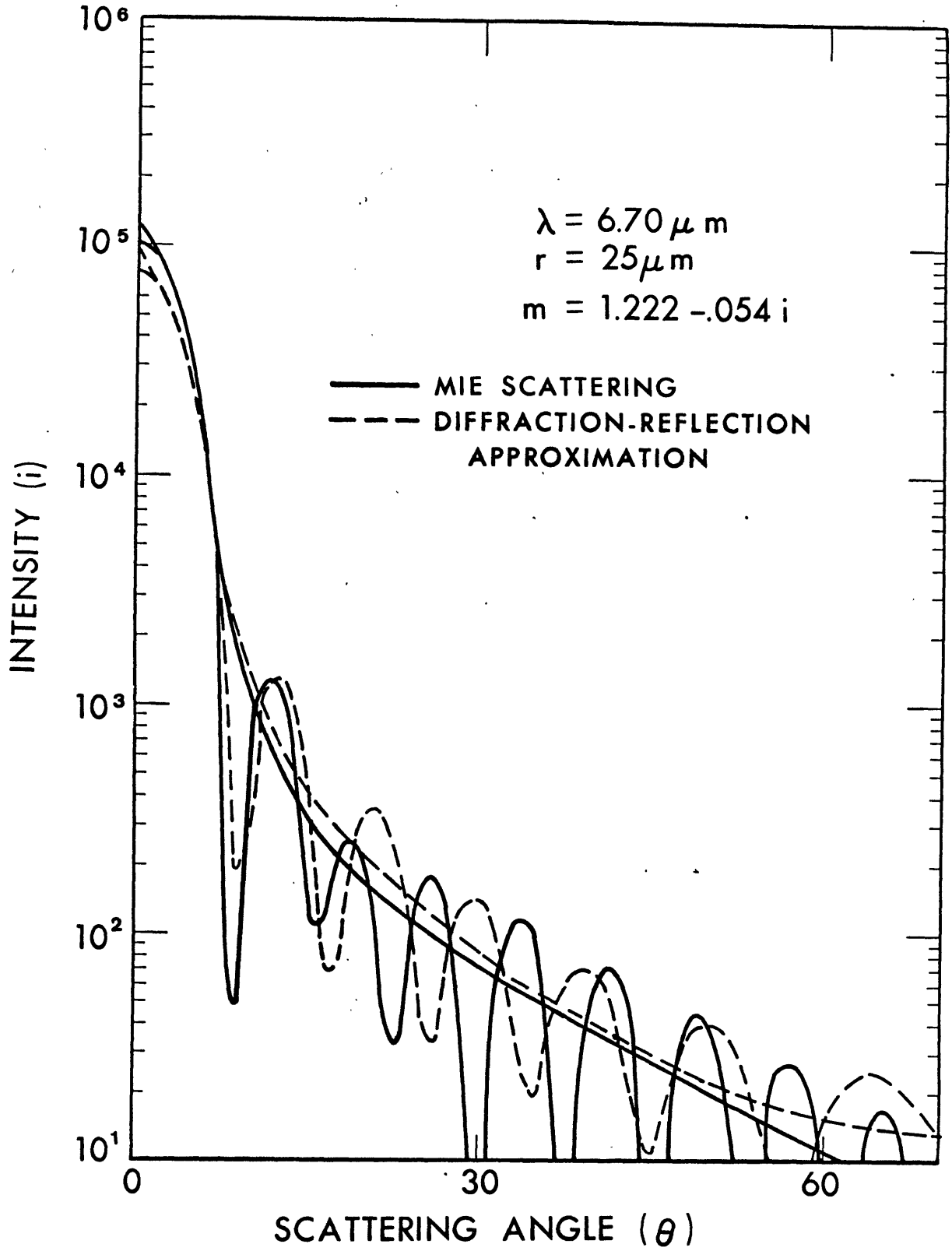

Figure 3.3--Intensity i versus the scattering angle θ for spheres computed according to the Mie theory and the diffraction-reflection approximation. Smooth curves are included.

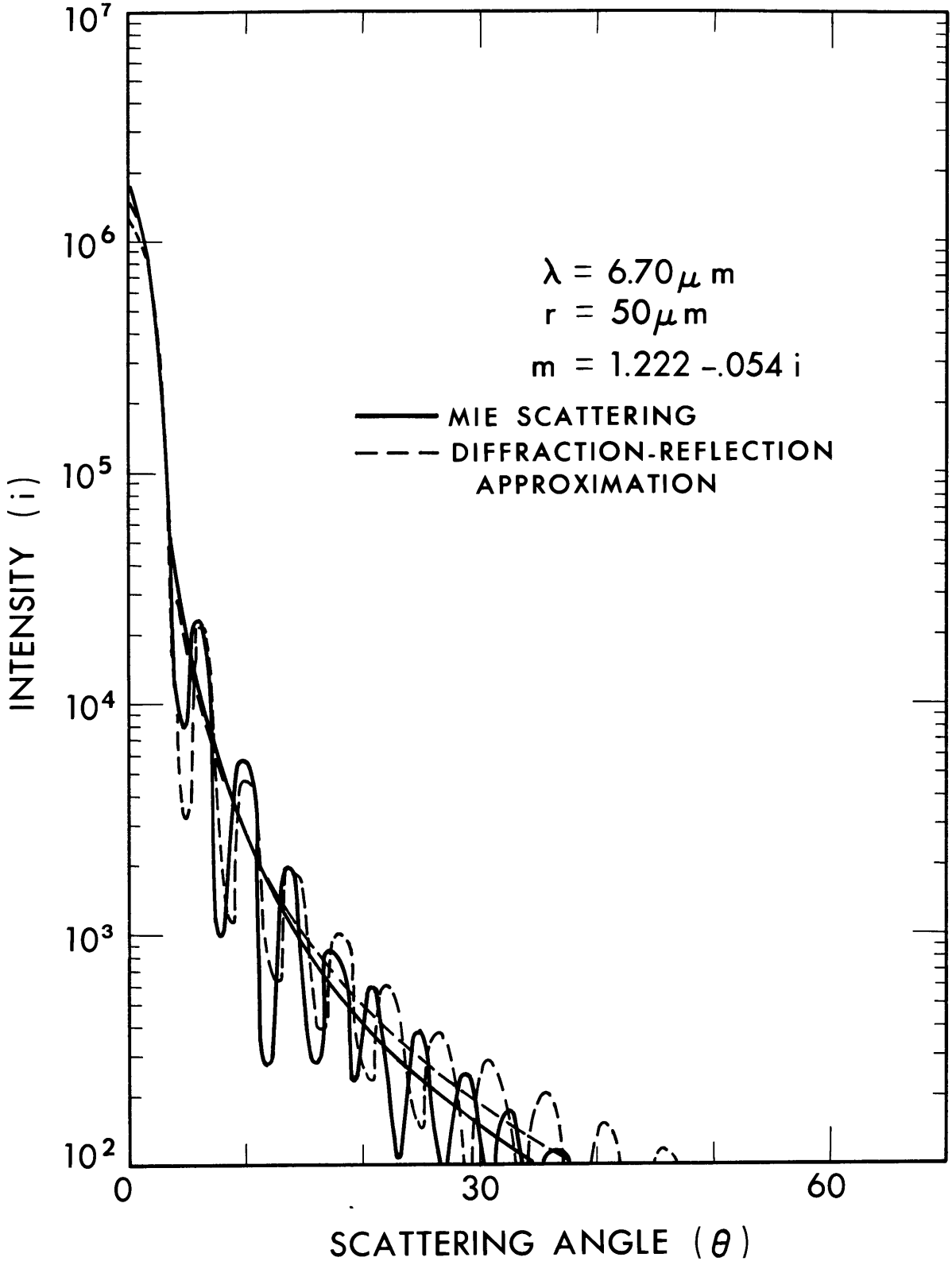

Figure 3.4--Intensity i versus the scattering angle θ for spheres computed according to the Mie theory and the diffraction-reflection approximation. Smooth curves are included.

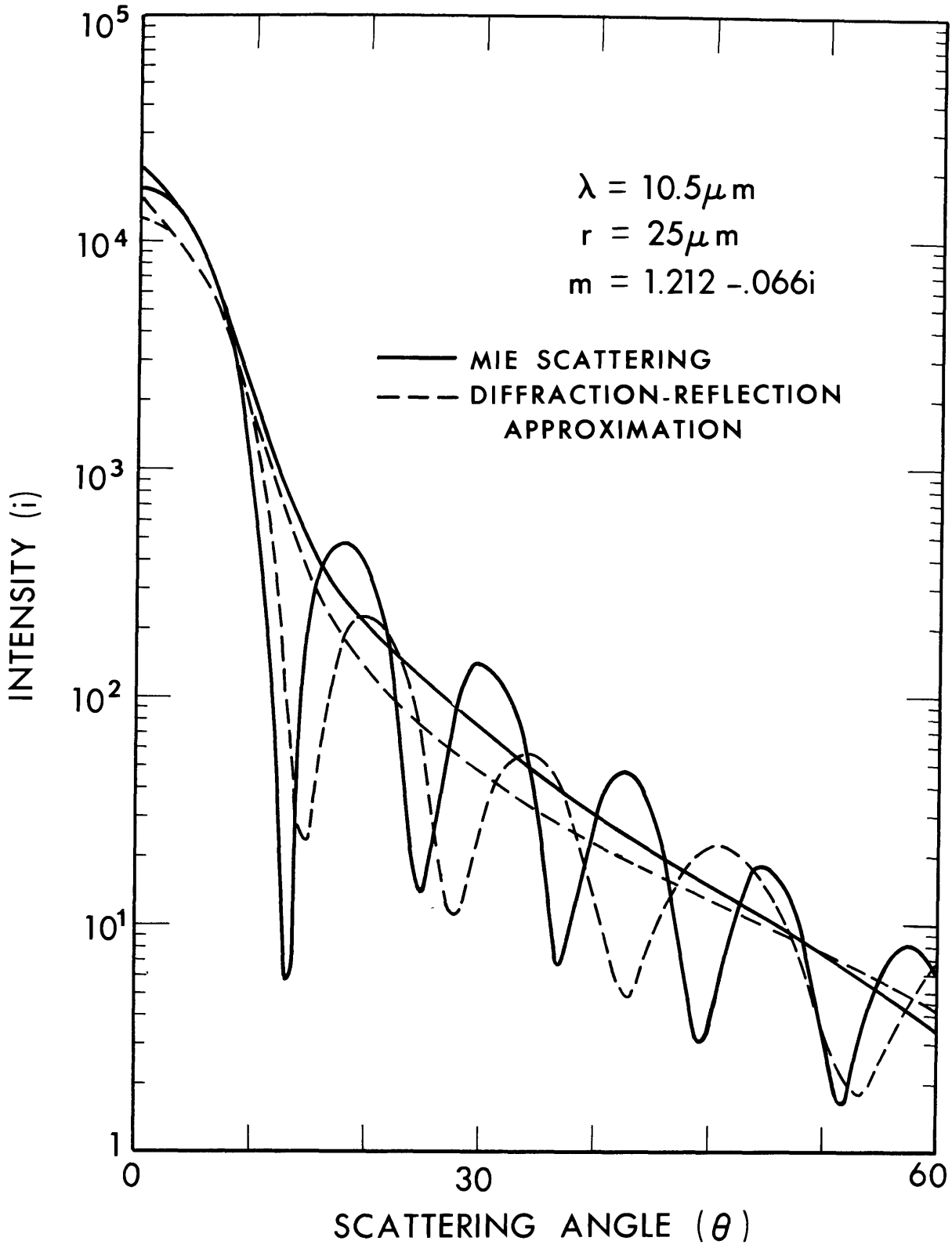

Figure 3.5--Intensity i versus the scattering angle θ for spheres computed according to the Mie theory and the diffraction-reflection approximation. Smooth curves are included.

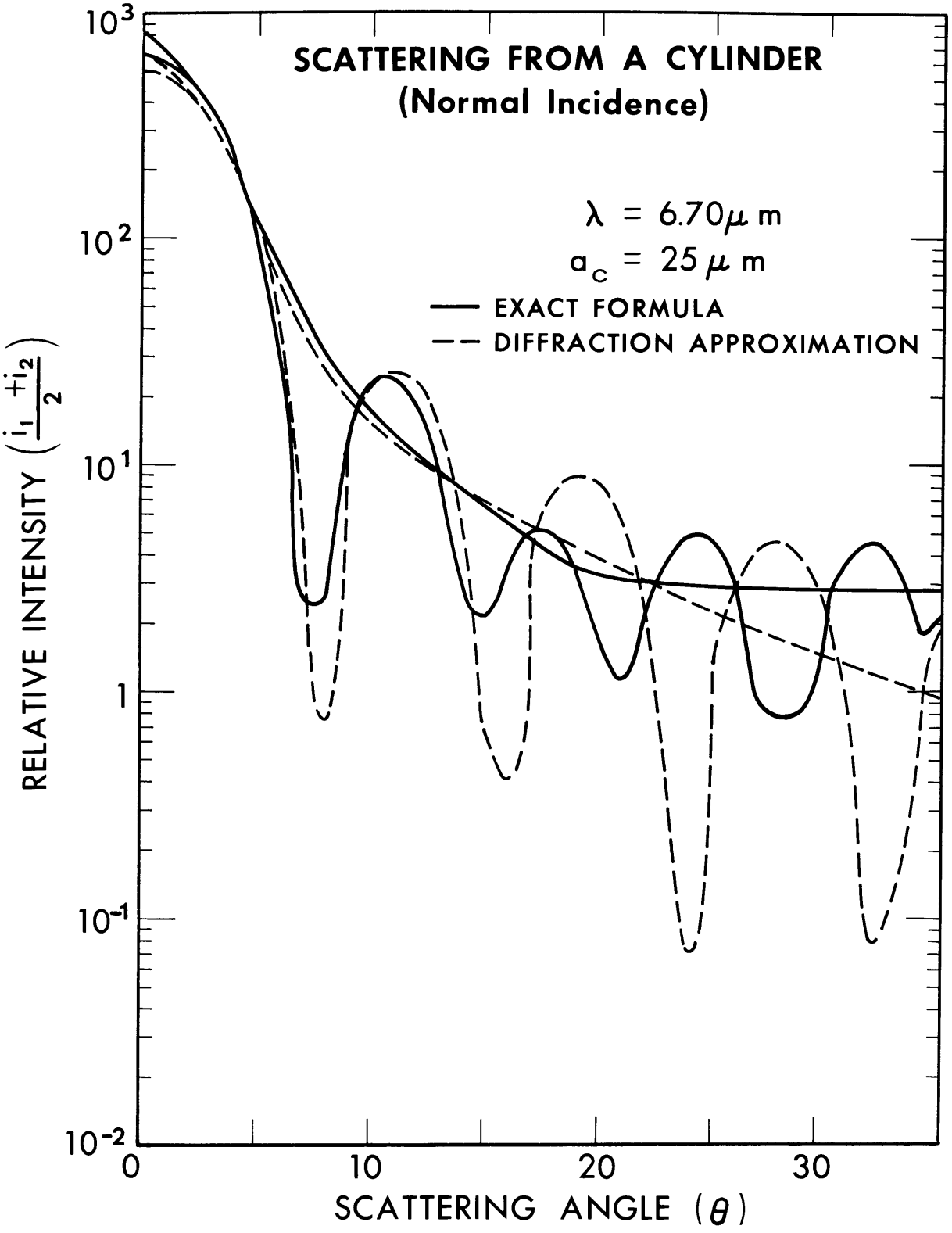

Figure 3.6--Average of the intensities i_1 and i_2 versus the scattering angle θ for radiation incident normally upon a cylinder according to the exact formula and the diffraction approximation.

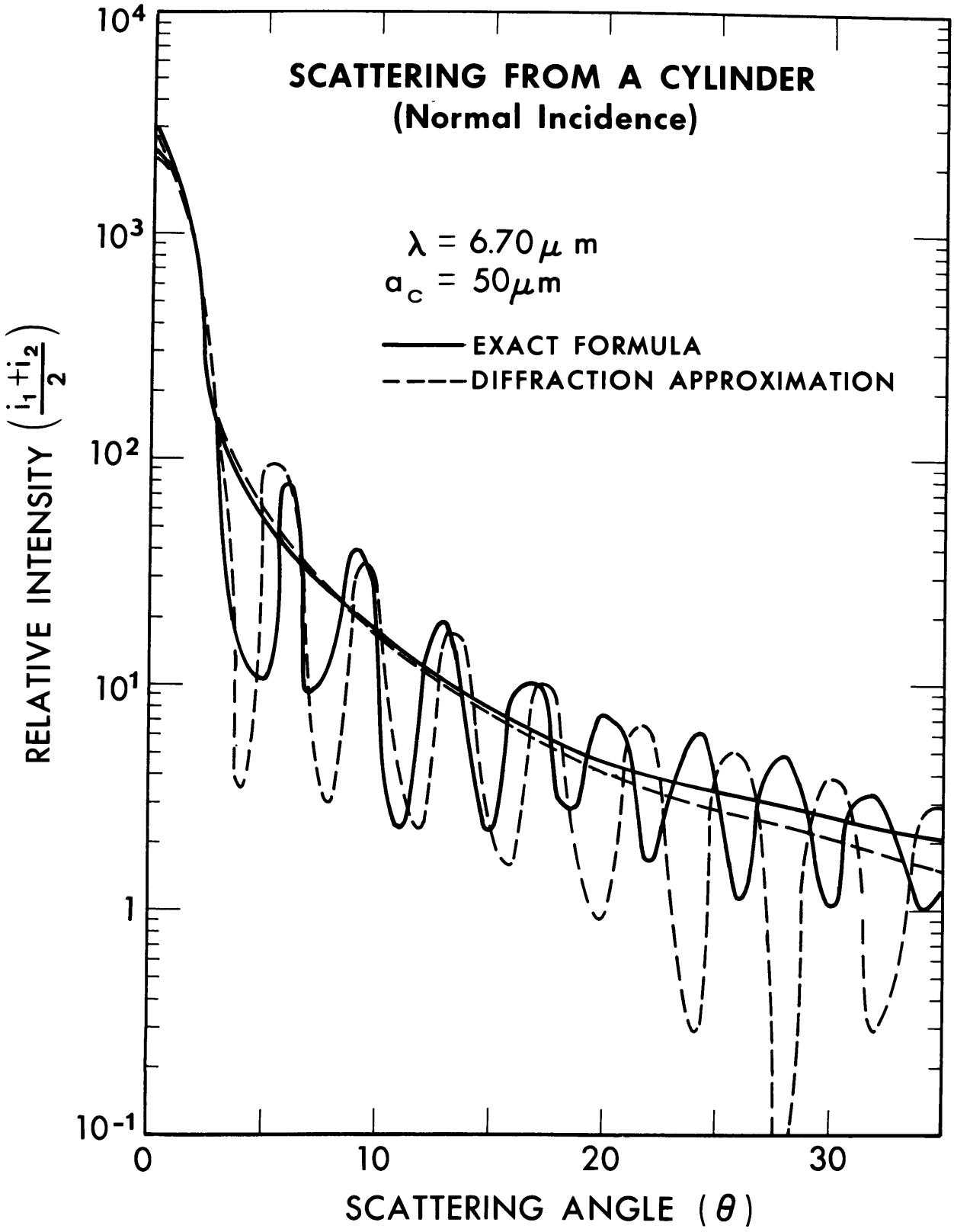

Figure 3.7--Average of the intensities i_1 and i_2 versus the scattering angle θ for radiation incident normally upon a cylinder according to the exact formula and the diffraction approximation.

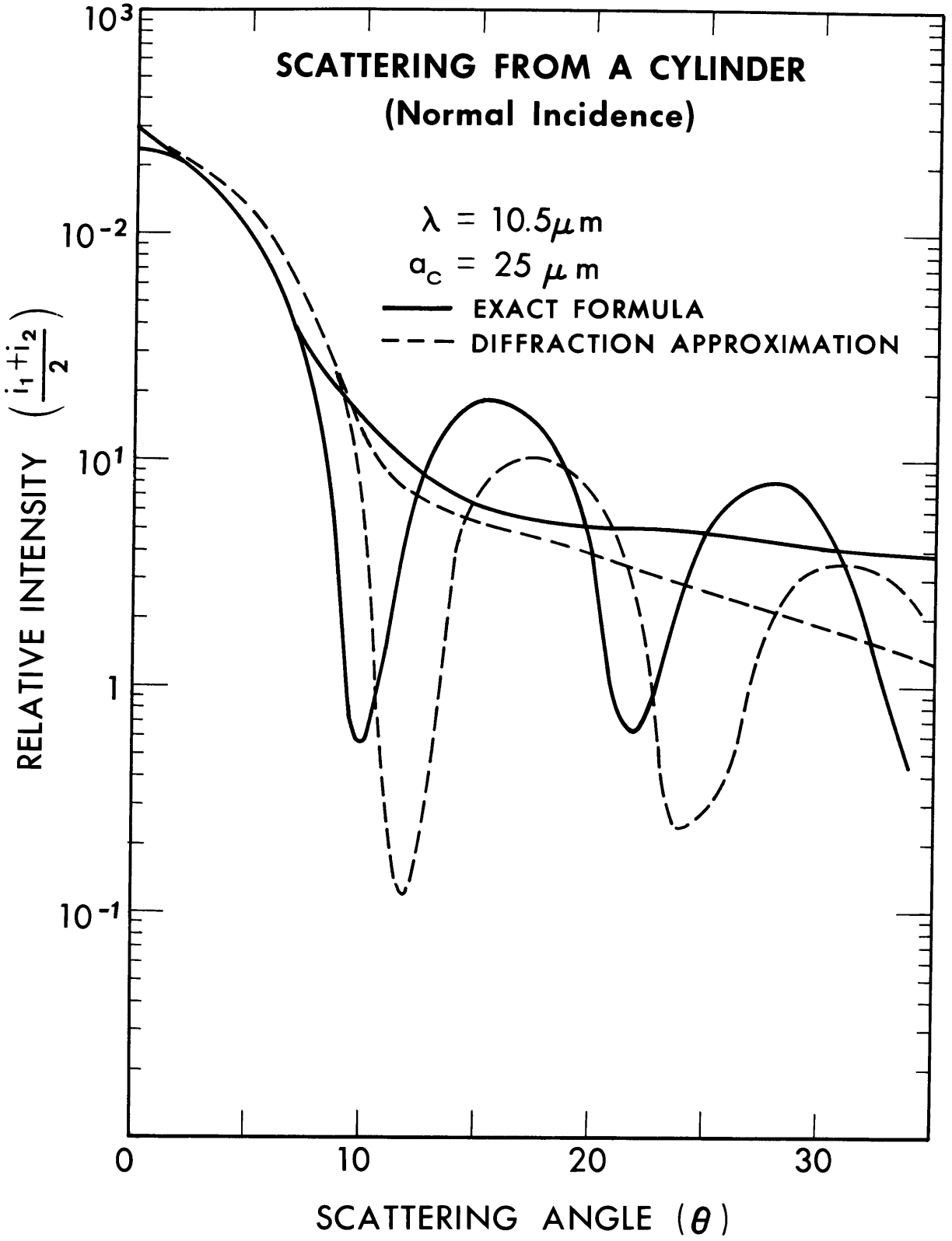

Figure 3.8--Average of the intensities i_1 and i_2 versus the scattering angle θ for radiation incident normally upon a cylinder according to the exact formula and the diffraction approximation.

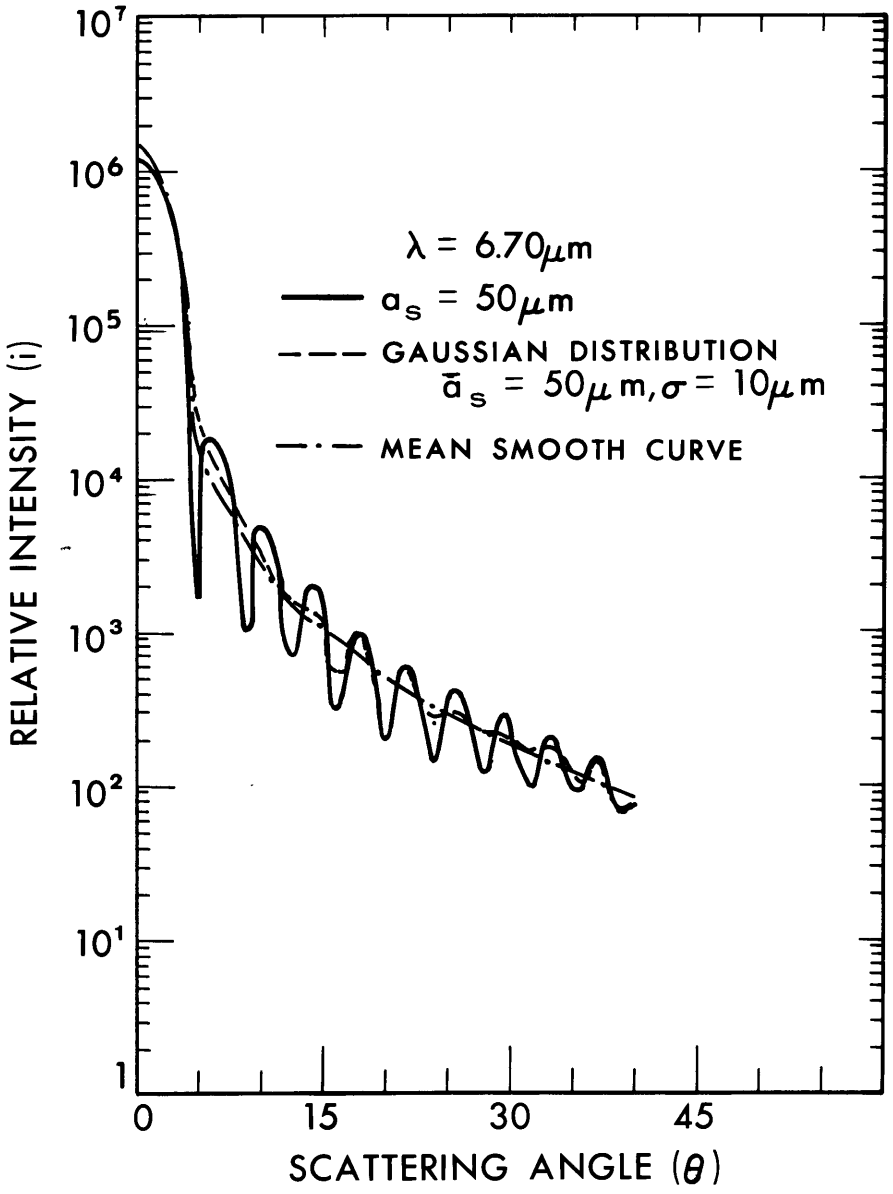

Figure 3.9--Relative intensity i versus the scattering angle θ for a sphere and a Gaussian distribution of spheres. The mean smooth curve for the sphere is included.

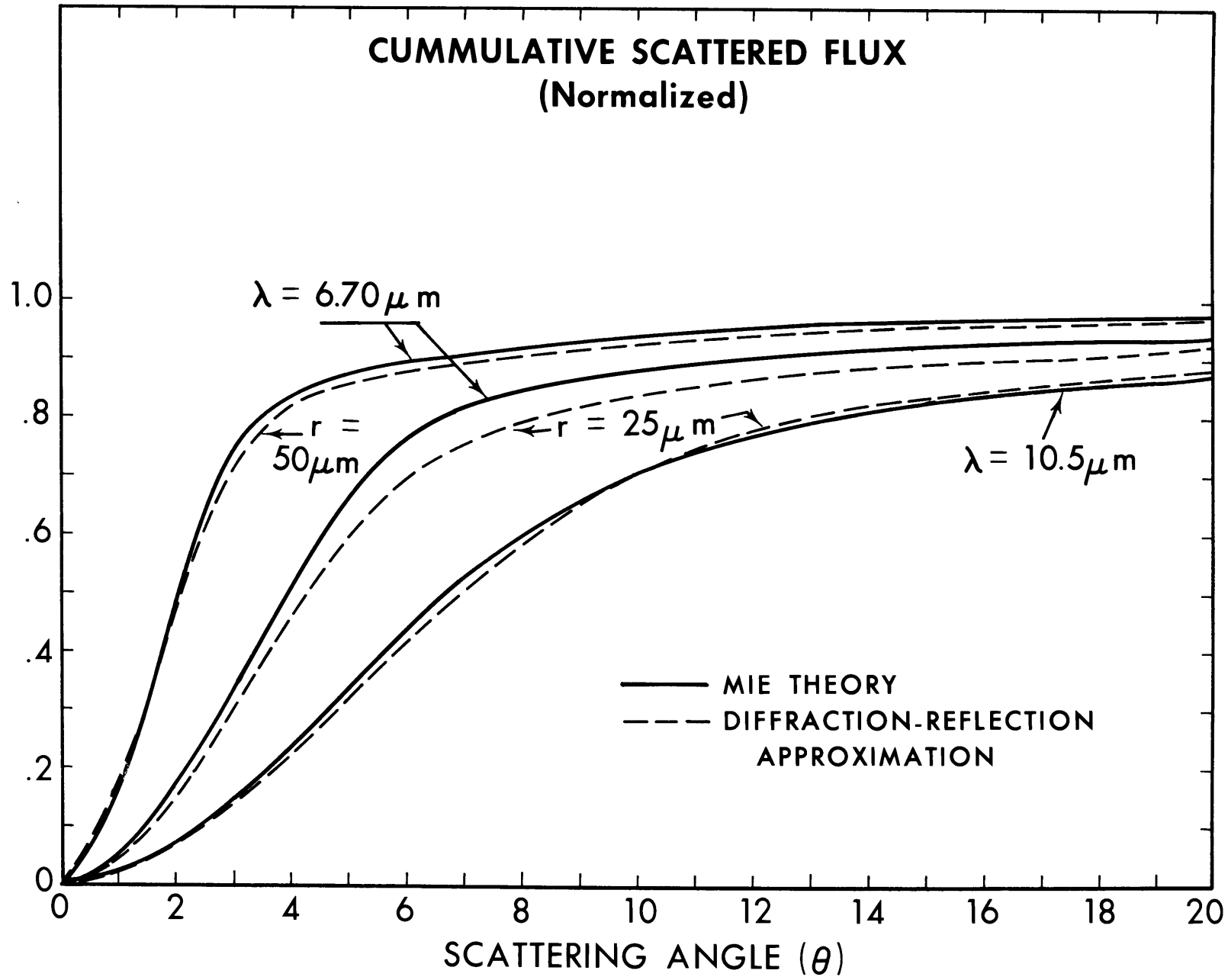

Figure 3.10--Cumulative scattered fluxes for the scattering functions computed according to the Mie theory or by the diffraction-reflection approximation.

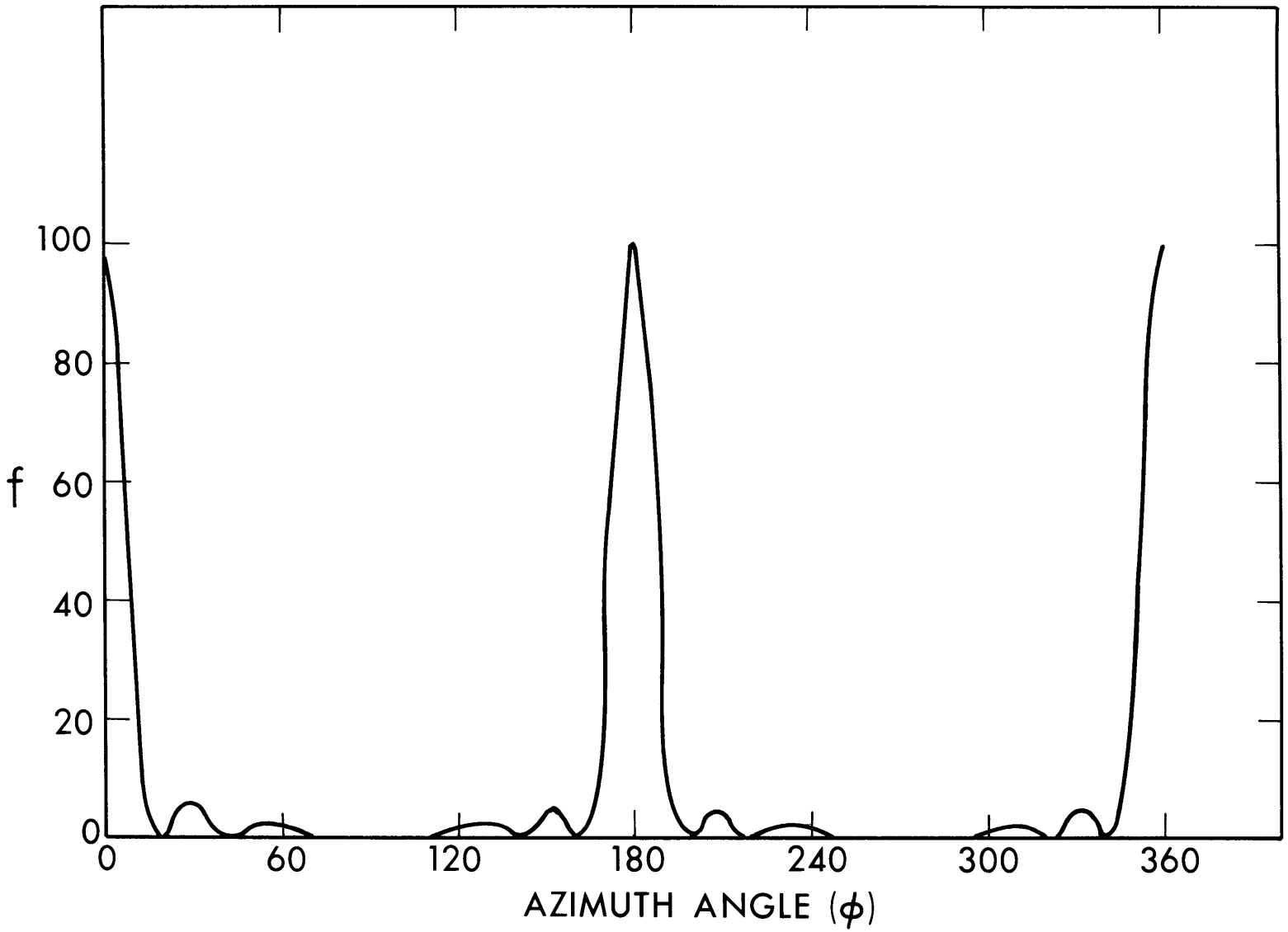

Figure 3.11--The function f versus the azimuthal angle ϕ.

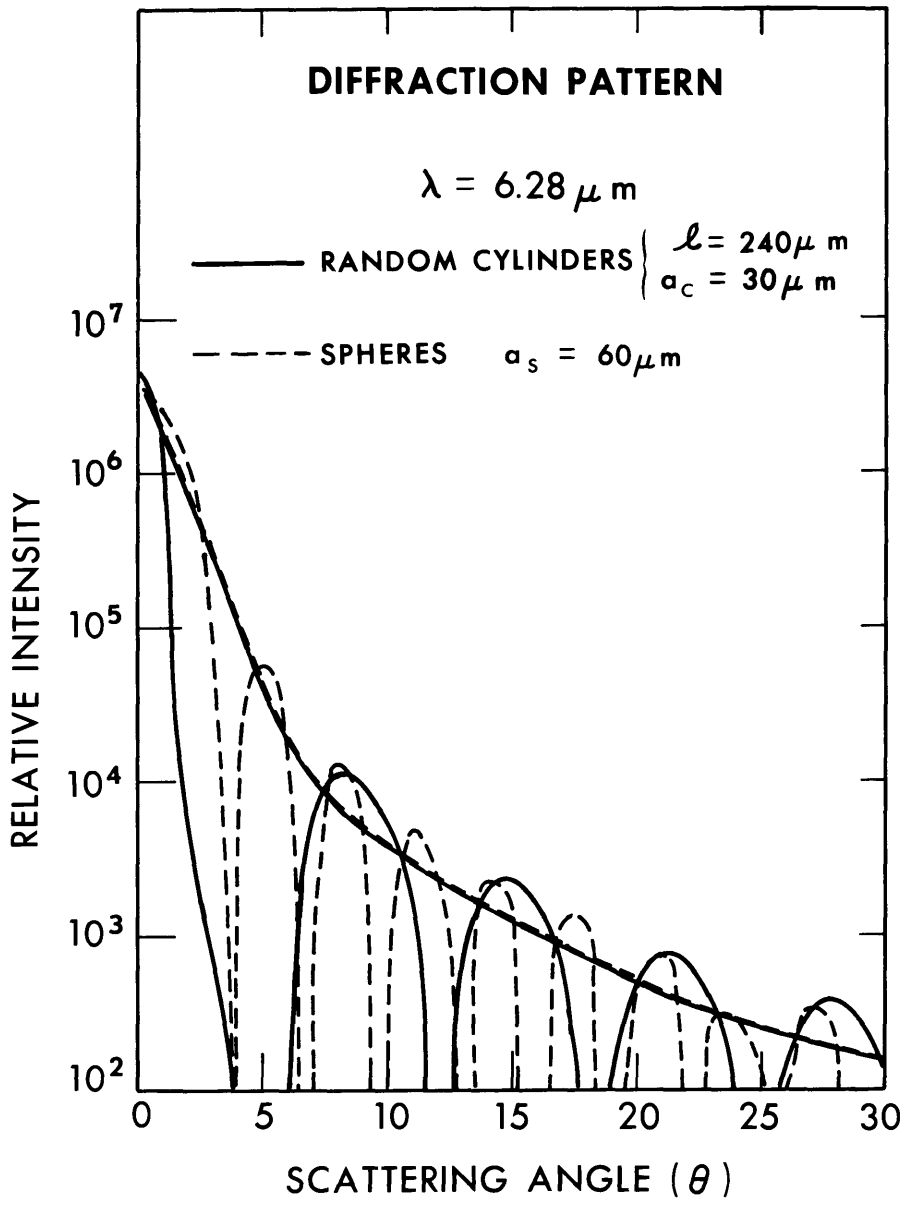

Figure 3.12--Diffraction patterns for randomly oriented cylinders and equivalent spheres.

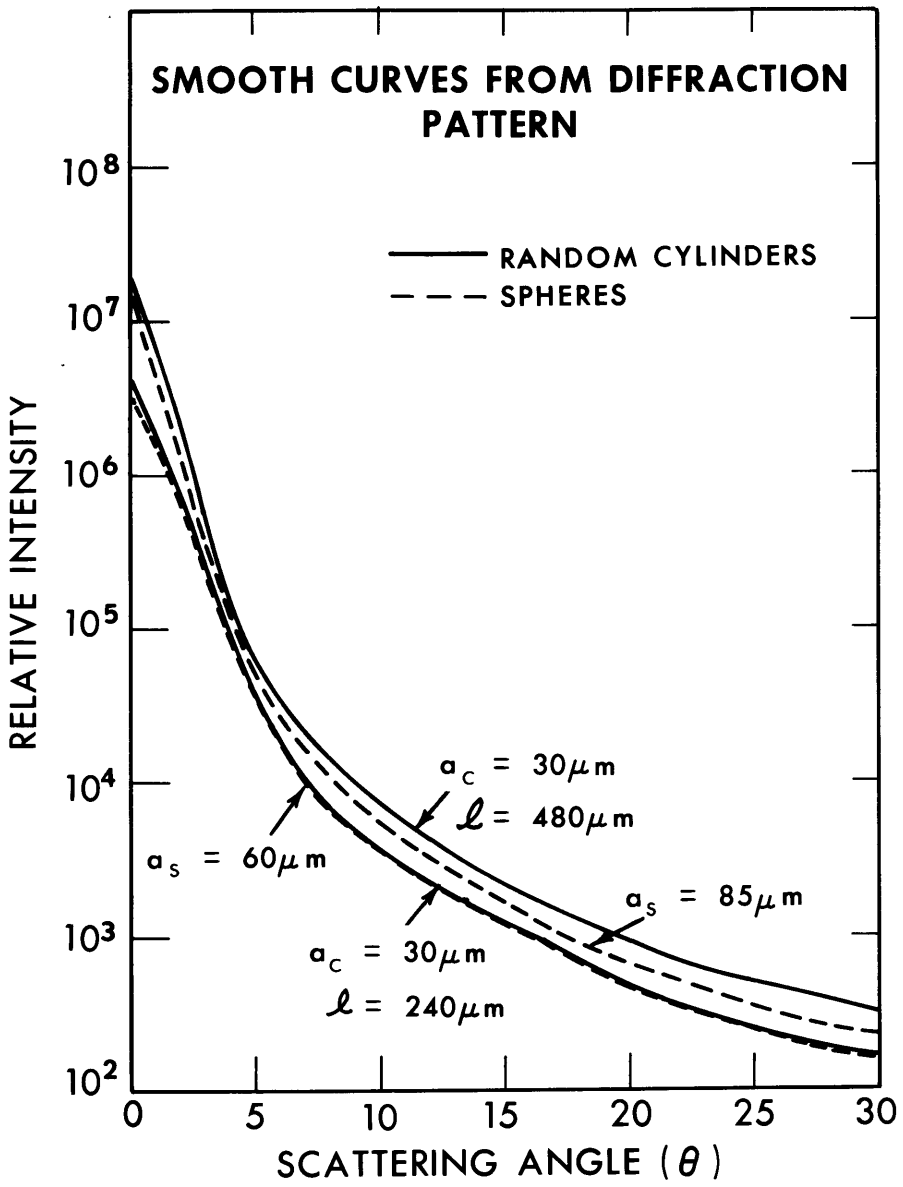

Figure 3.13--Smooth curves of the diffraction pattern for randomly oriented cylinders and equivalent spheres; λ = 6.28 μm

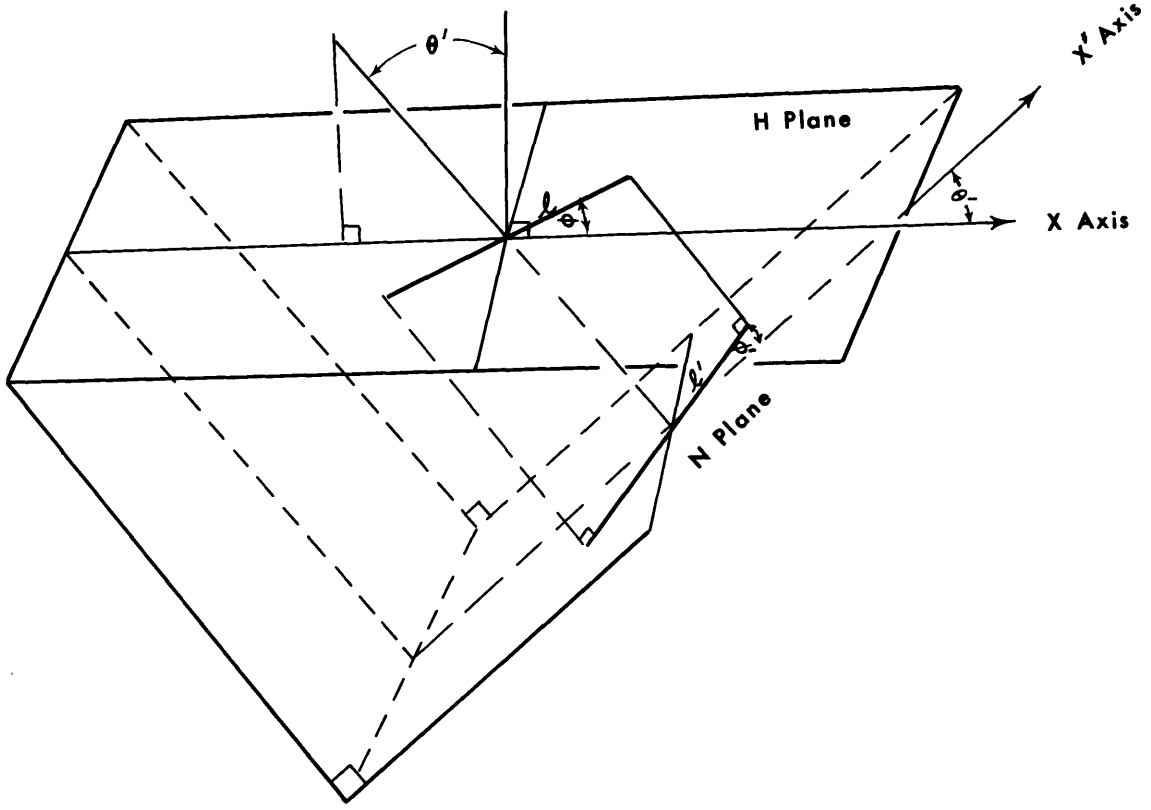

Figure 3.14--Geometry for scattering in the H- and N-planes.

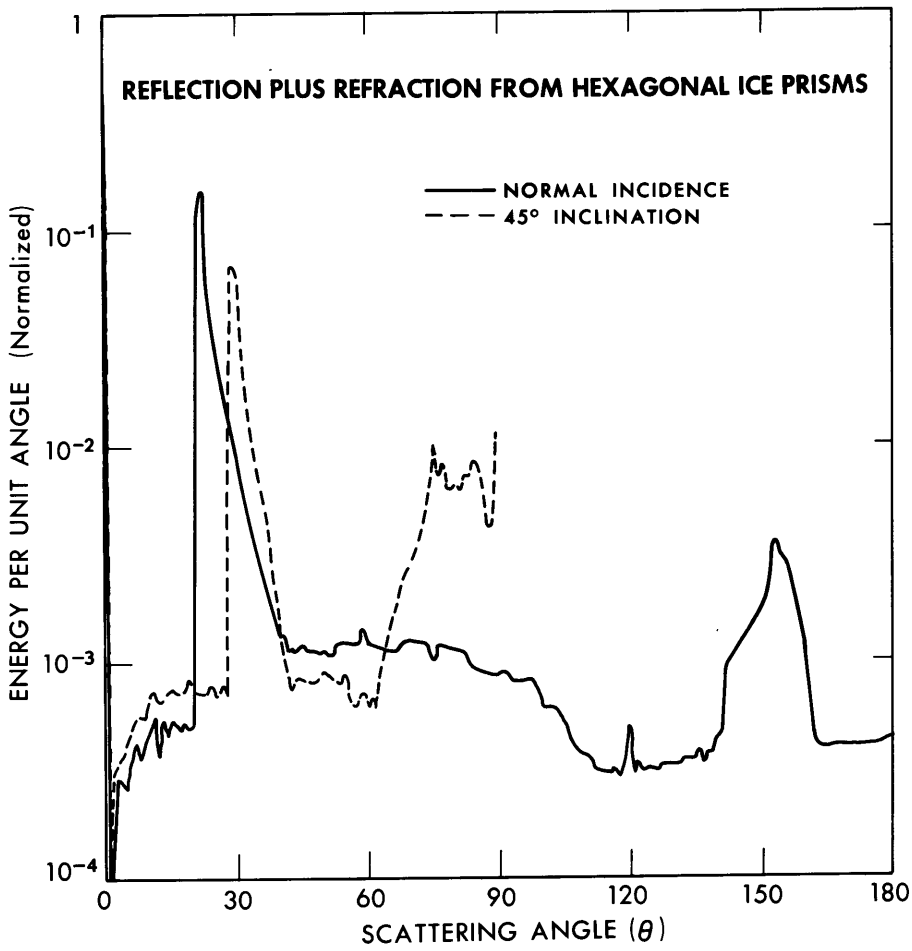

Figure 3.15--Energy per unit angle reflected plus refracted from hexagonal ice crystals versus the scattering angle θ.

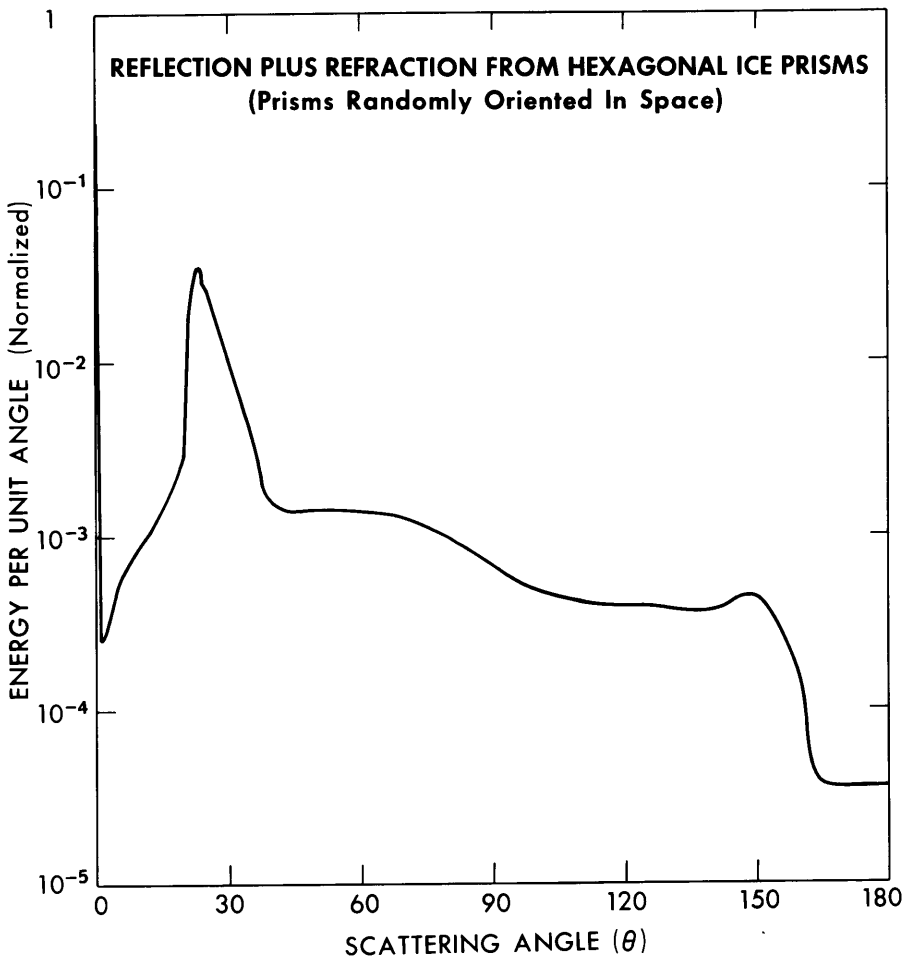

Figure 3.16--Energy per unit angle reflected plus refracted from randomly oriented hexagonal ice prisms versus the scattering angle θ.

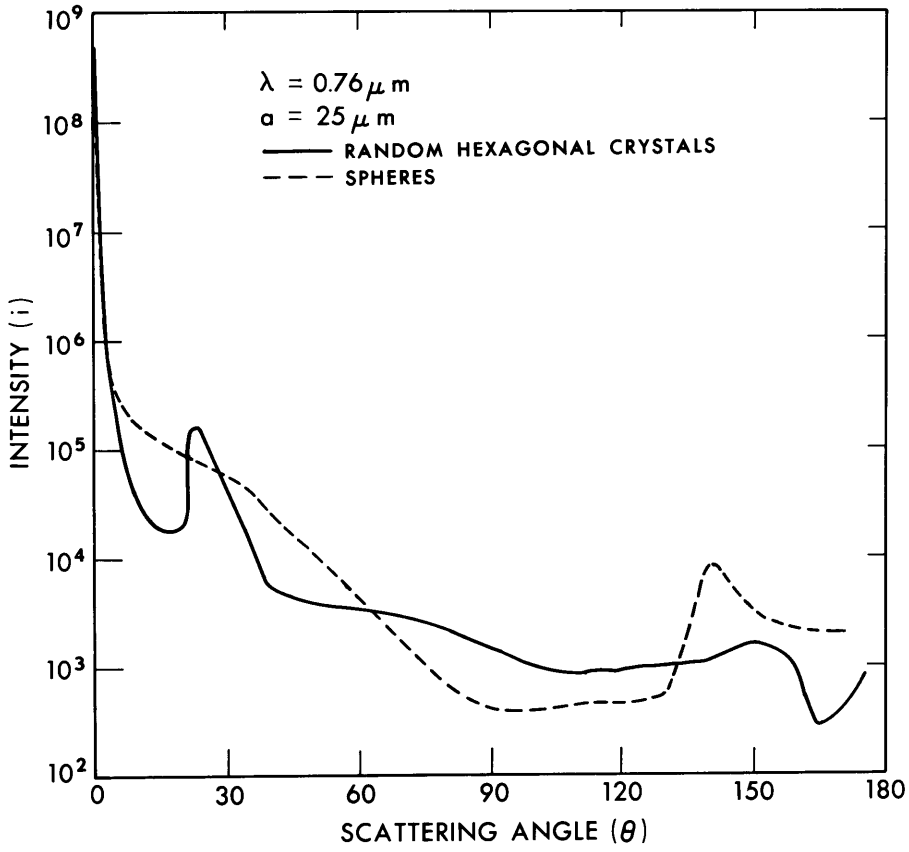

Figure 3.17--Total intensity, i, for randomly oriented hexagonal prisms compared with that for spheres versus the scattering angle θ.

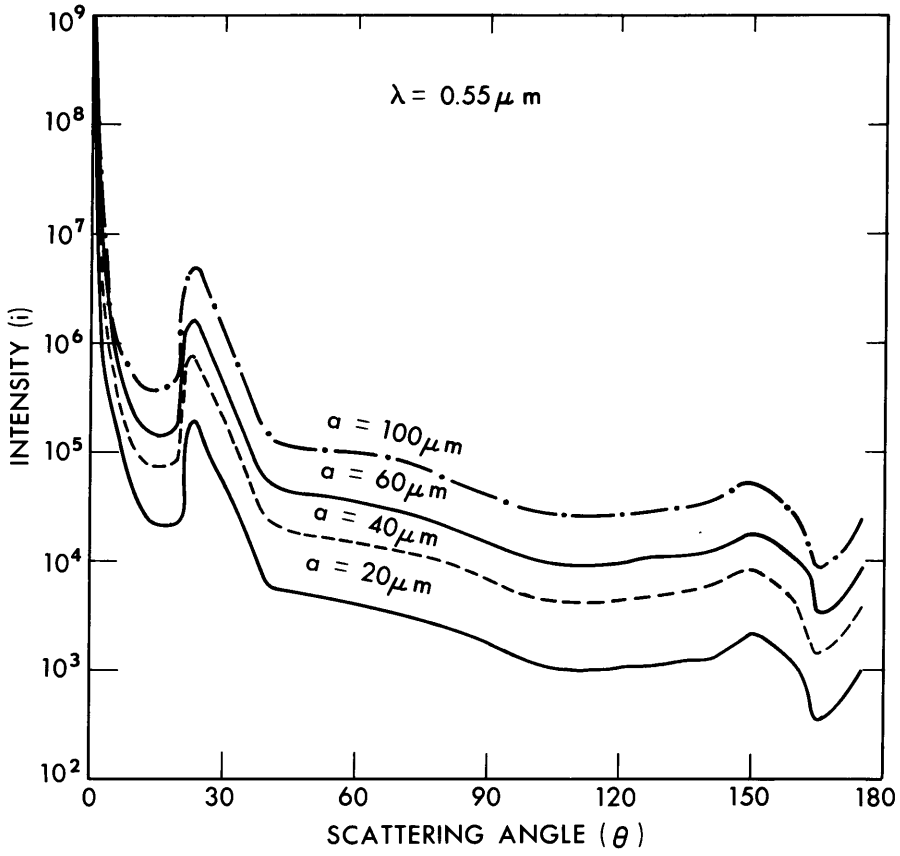

Figure 3.18--Intensity, i, from randomly oriented hexagonal crystals for different equivalent sphere radii versus the scattering angle θ.

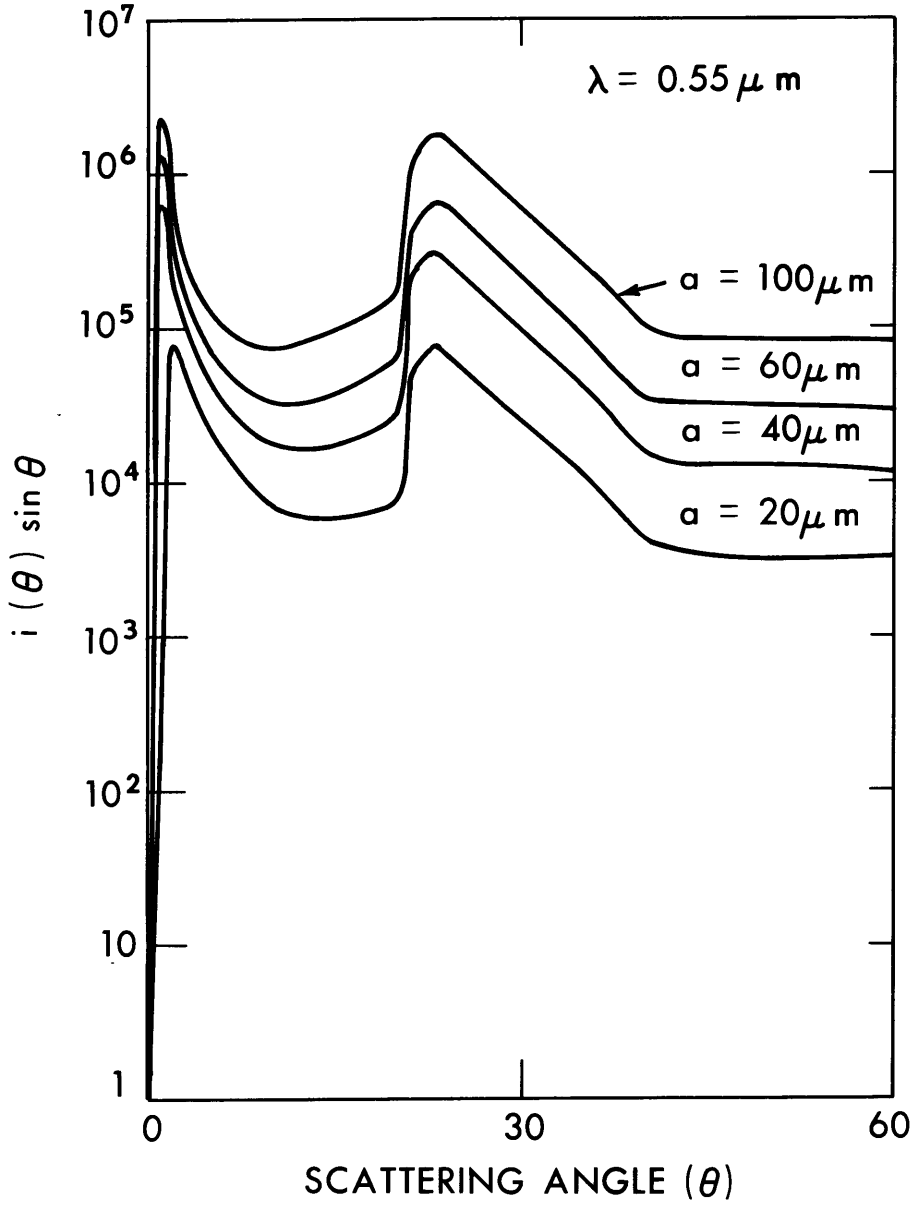

Figure 3.19--i(θ) sin θ for the same crystals as those in figure 3.18 versus the scattering angle θ .

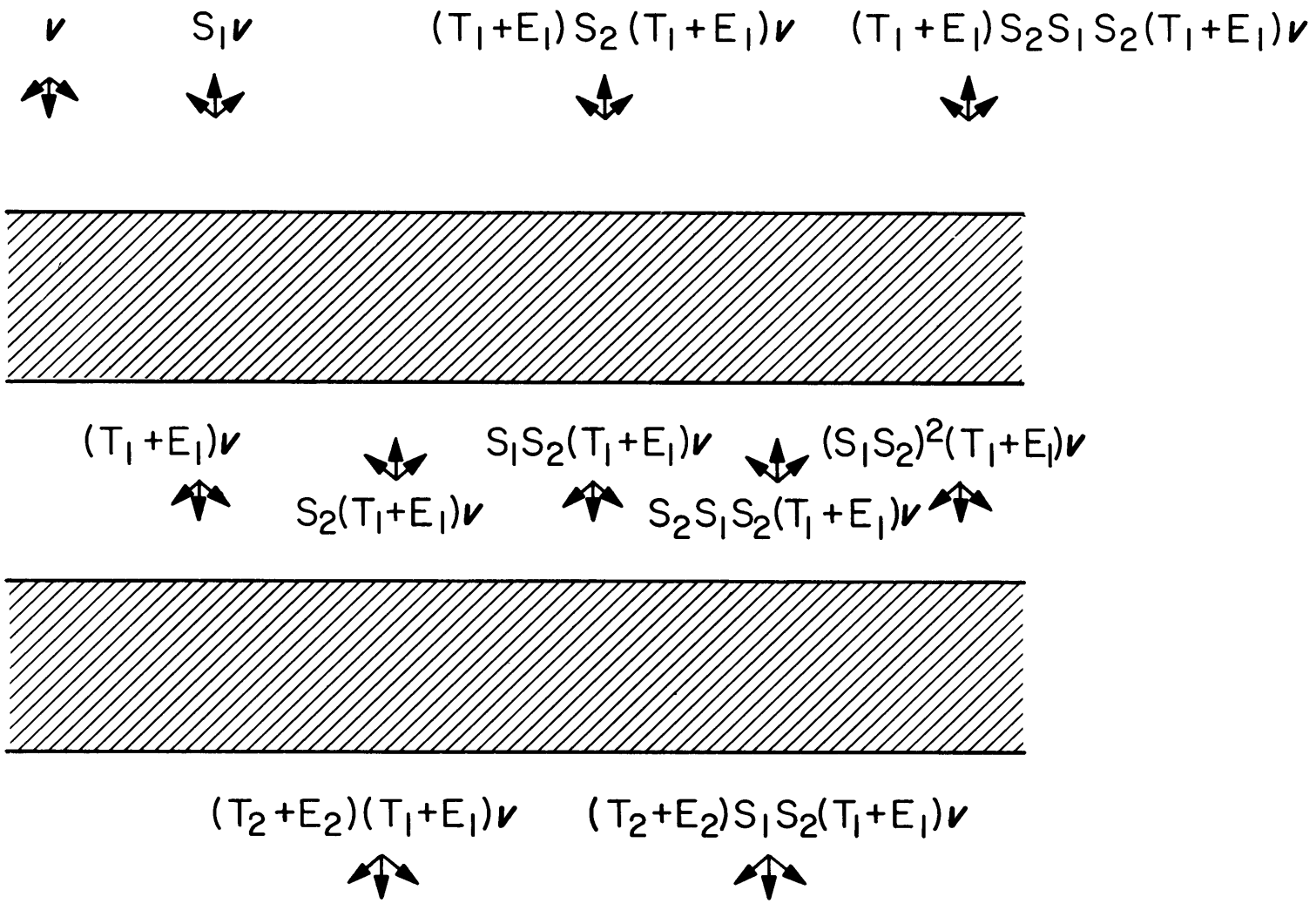

Figure 4.1--Schematic of the addition of layers method for computing the reflection and transmission.

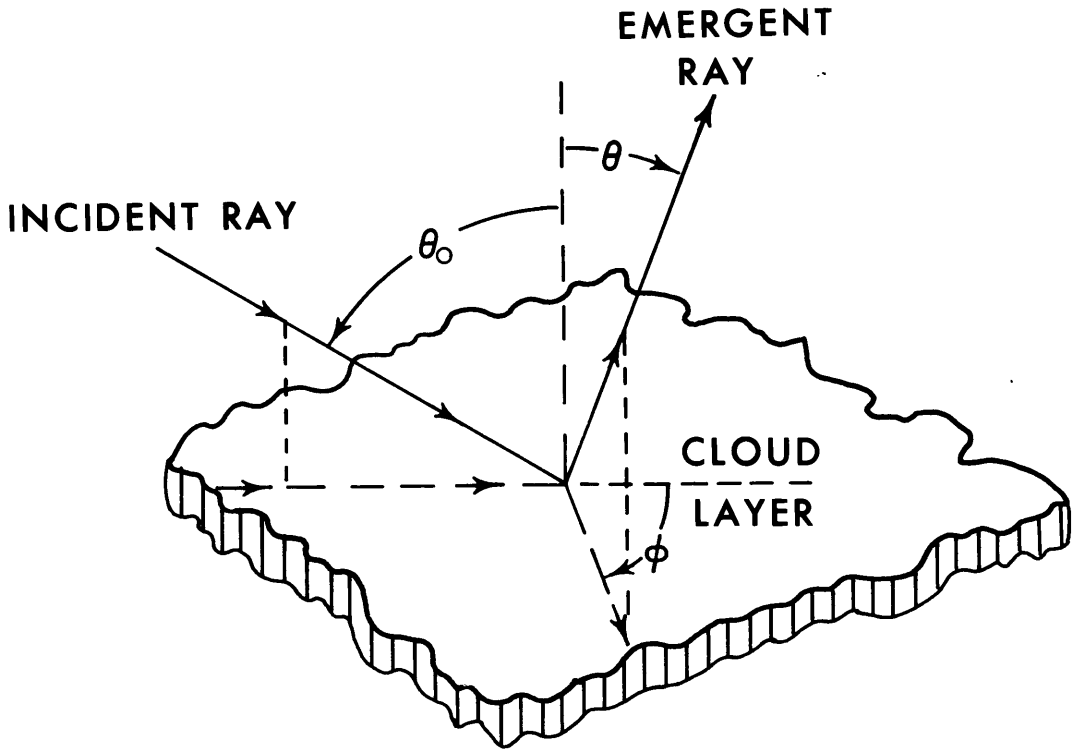

Figure 4.2--Geometry of scattering from a cloud layer.

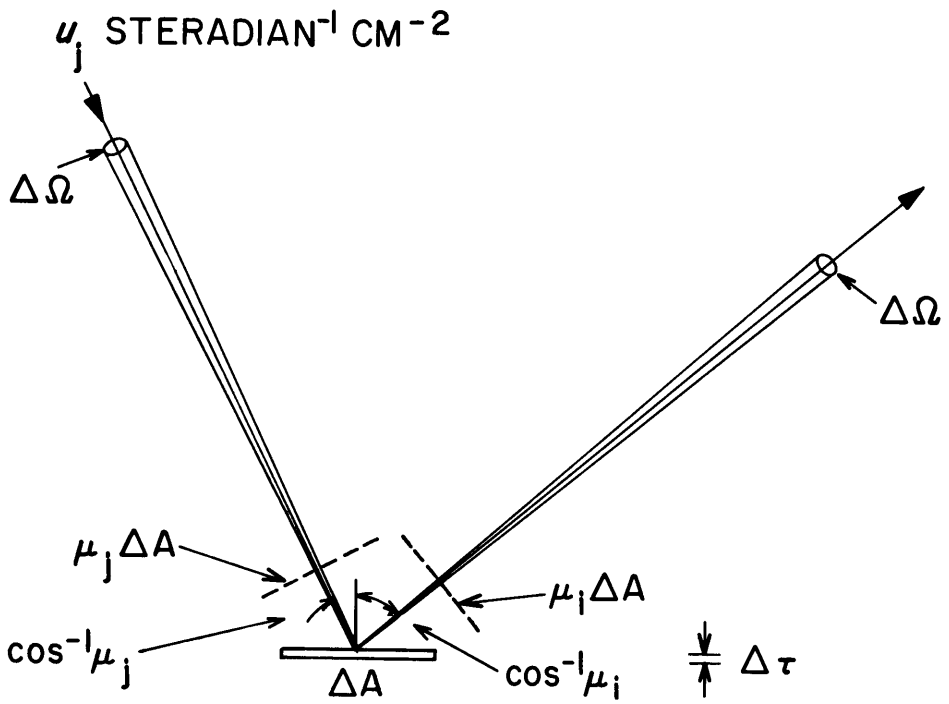

Figure 4.3--Geometry of scattering from an infinitesimal layer.

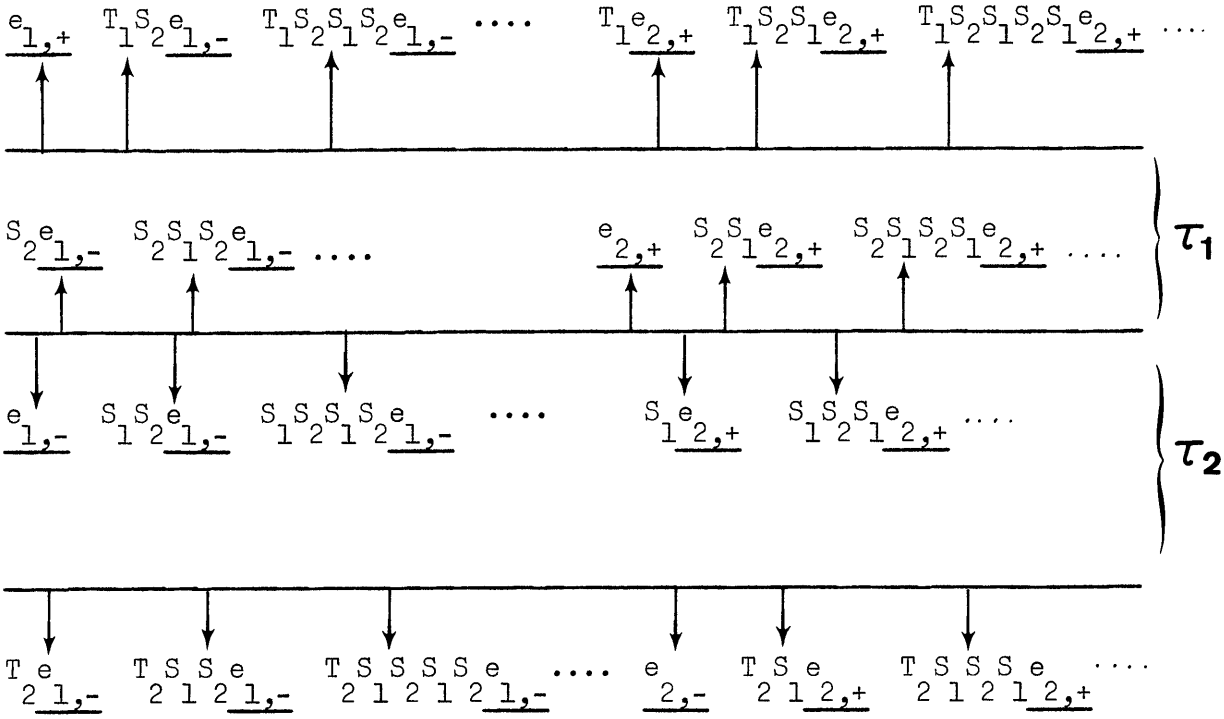

Figure 4.4--Schematic of the addition of layers method for computing the emission.

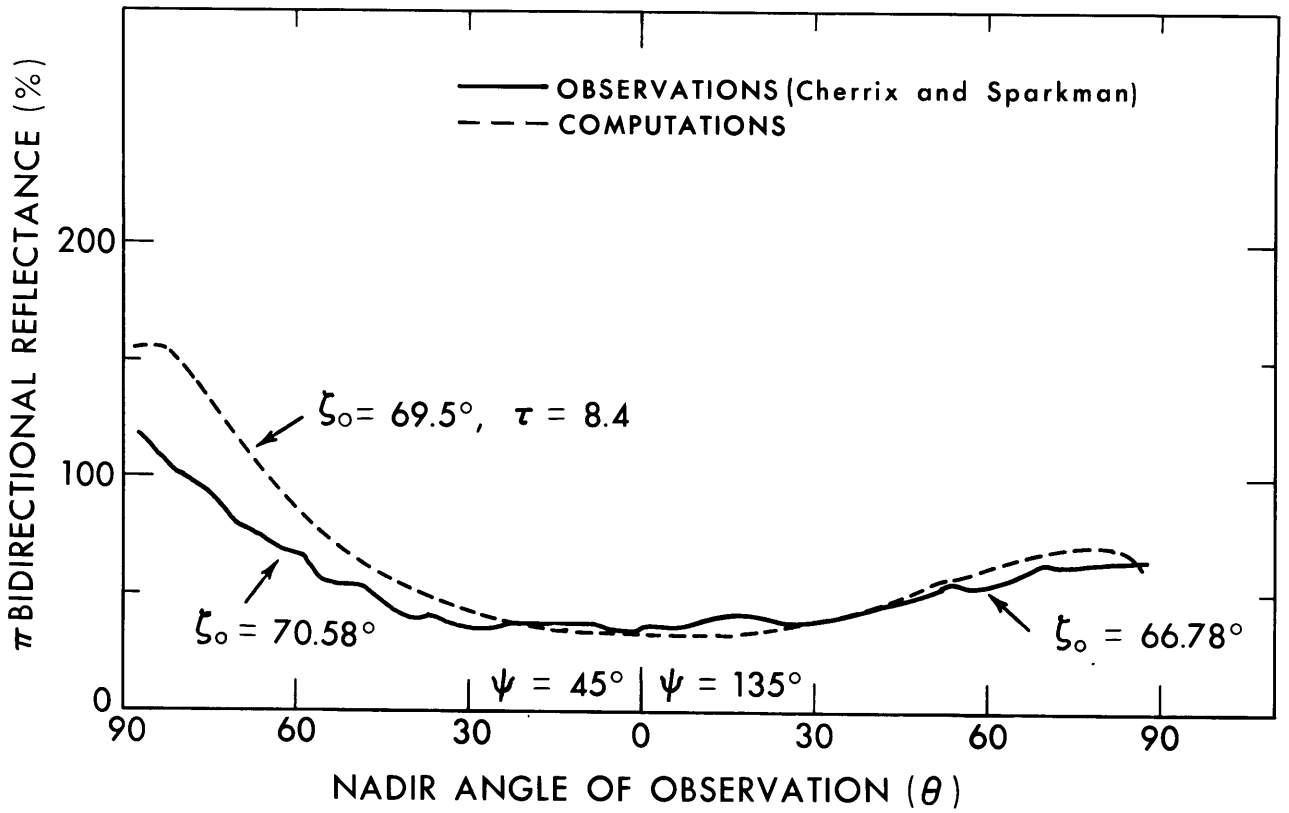

Figure 4.5-- π Bidirectional reflectance versus the nadir angle of observation θ as derived by theory as compared with actual observations. ζ_o is the solar zenith angle, ψ is the azimuth plane, and τ is the optical thickness of the cloud model.

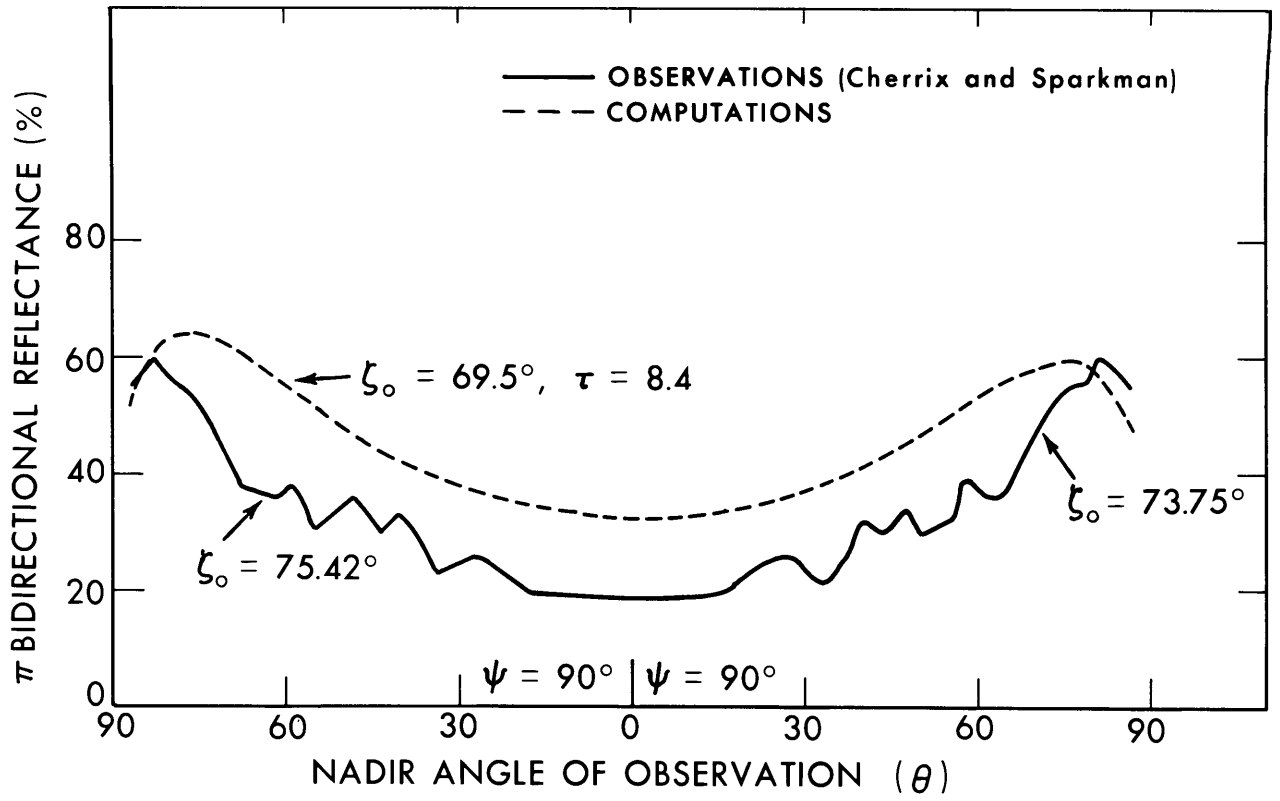

Figure 4.6--Π Bidirectional reflectance versus the nadir angle of observation θ as derived by theory as compared with actual observations. ζ_0 is the solar zenith angle, φ is the azimuth plane, and τ is the optical thickness of the cloud model.

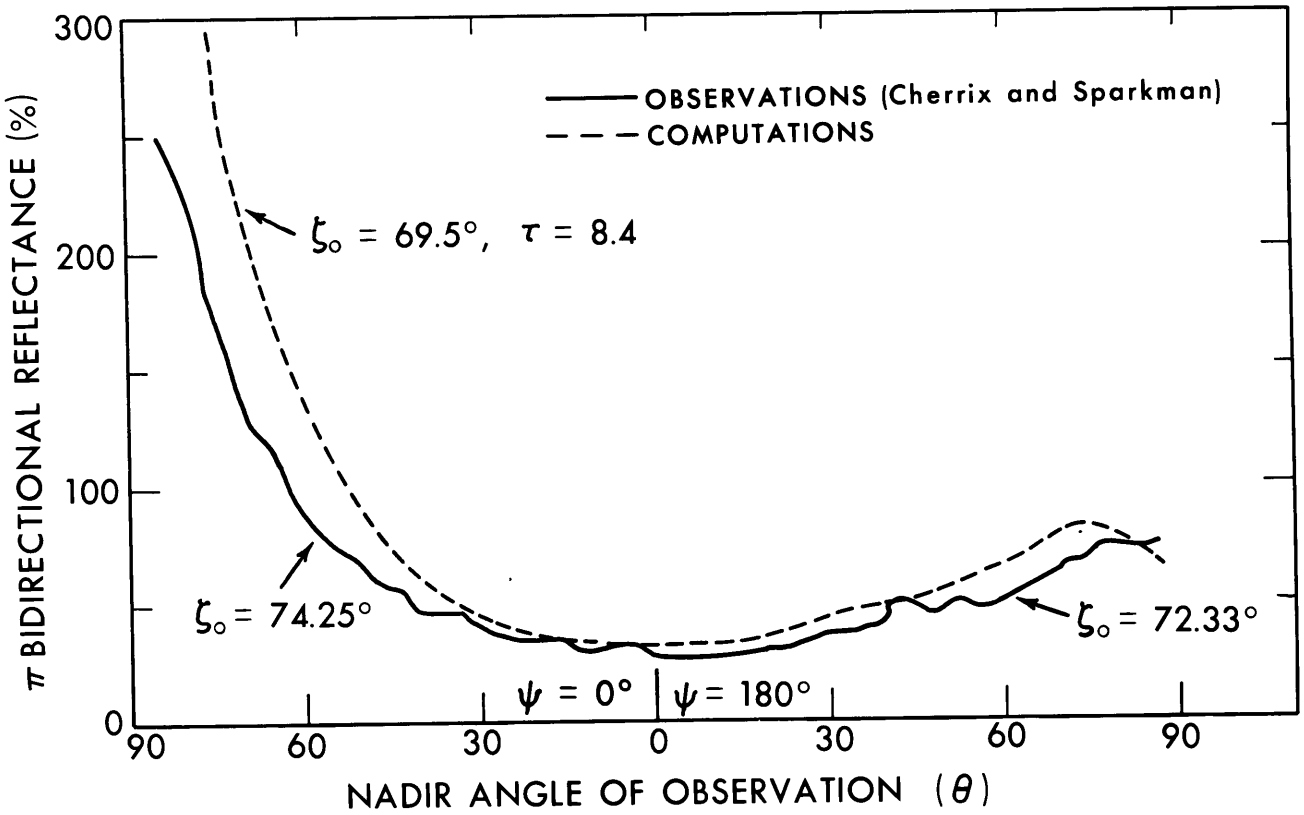

Figure 4.7-- π Bidirectional reflectance versus the nadir angle of observation θ as derived by theory as compared with actual observations. ζ_0 is the solar zenith angle, ψ is the azimuth plane, and τ is the optical thickness of the cloud model.

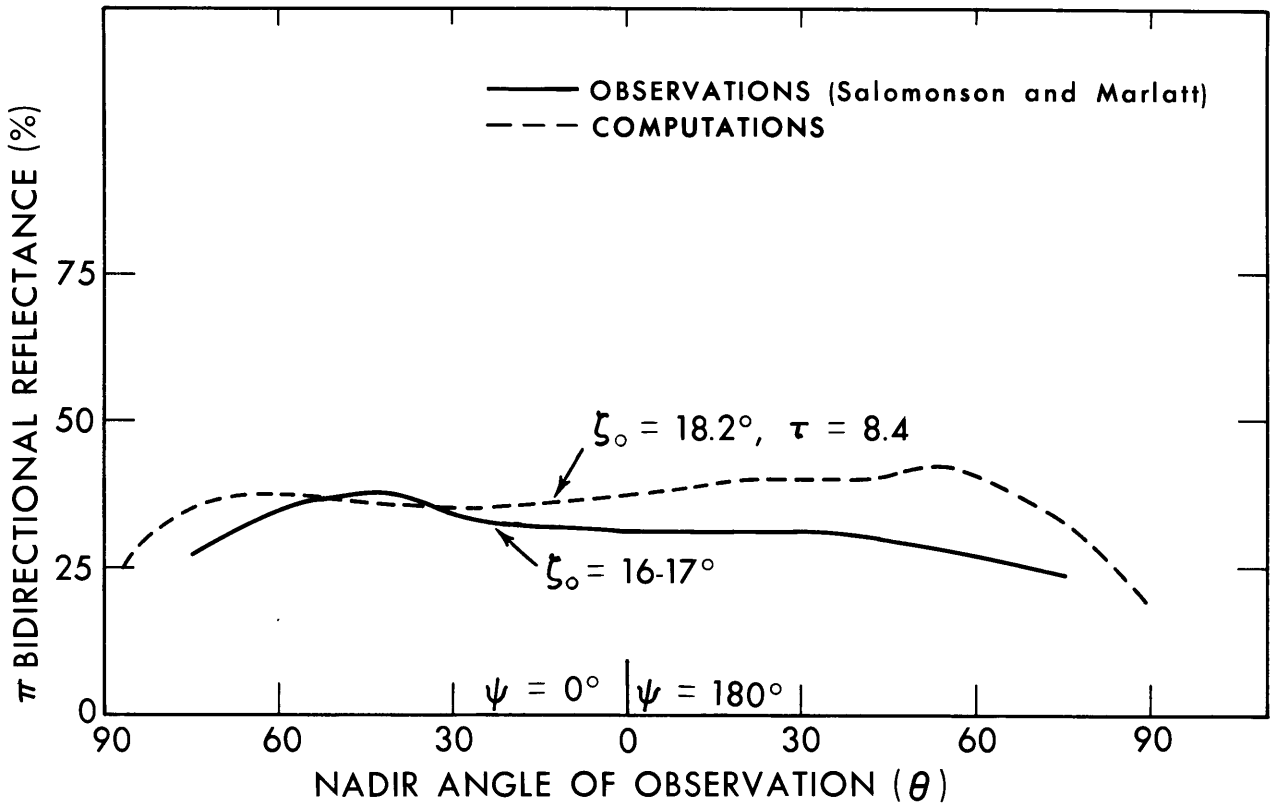

Figure 4.8-- π Bidirectional reflectance versus the nadir angle of observation θ as derived by theory as compared with actual observations. ζ_0 is the solar zenith angle, ψ is the azimuth plane, and τ is the optical thickness of the cloud model.

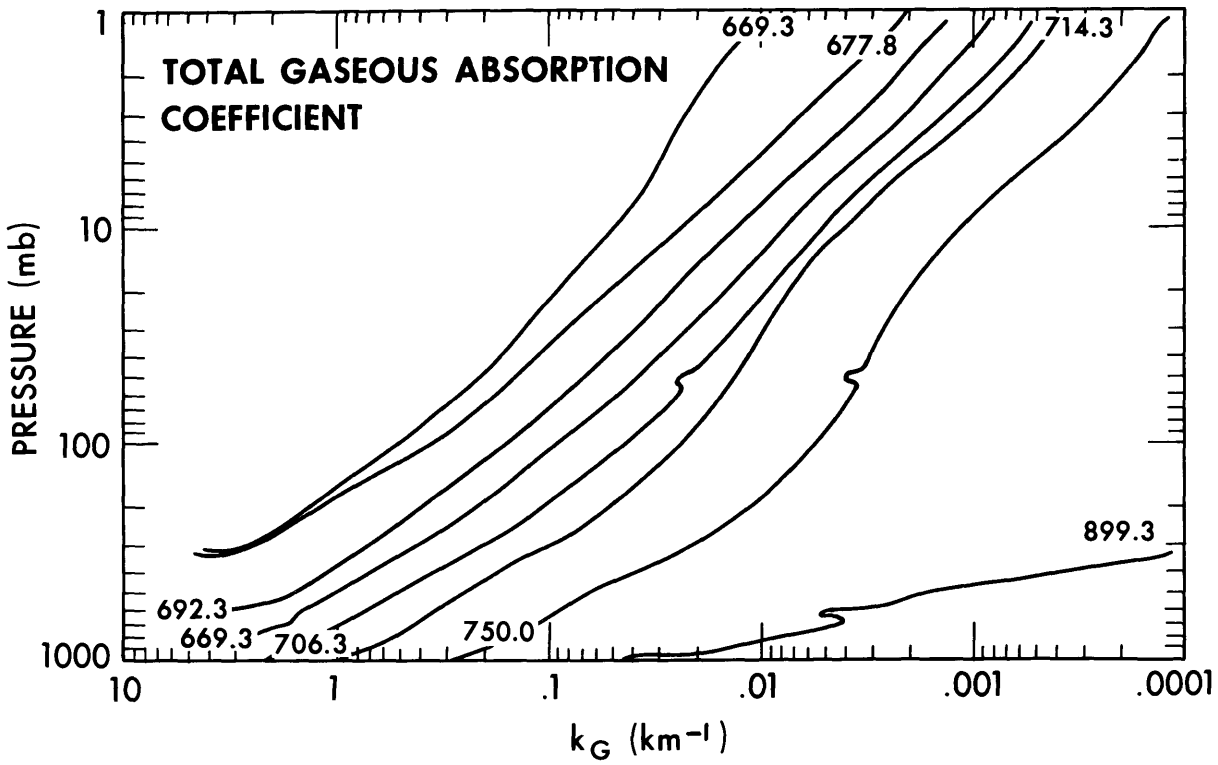

Figure 4.9--Total gaseous absorption coefficient, k_G, versus the pressure p.

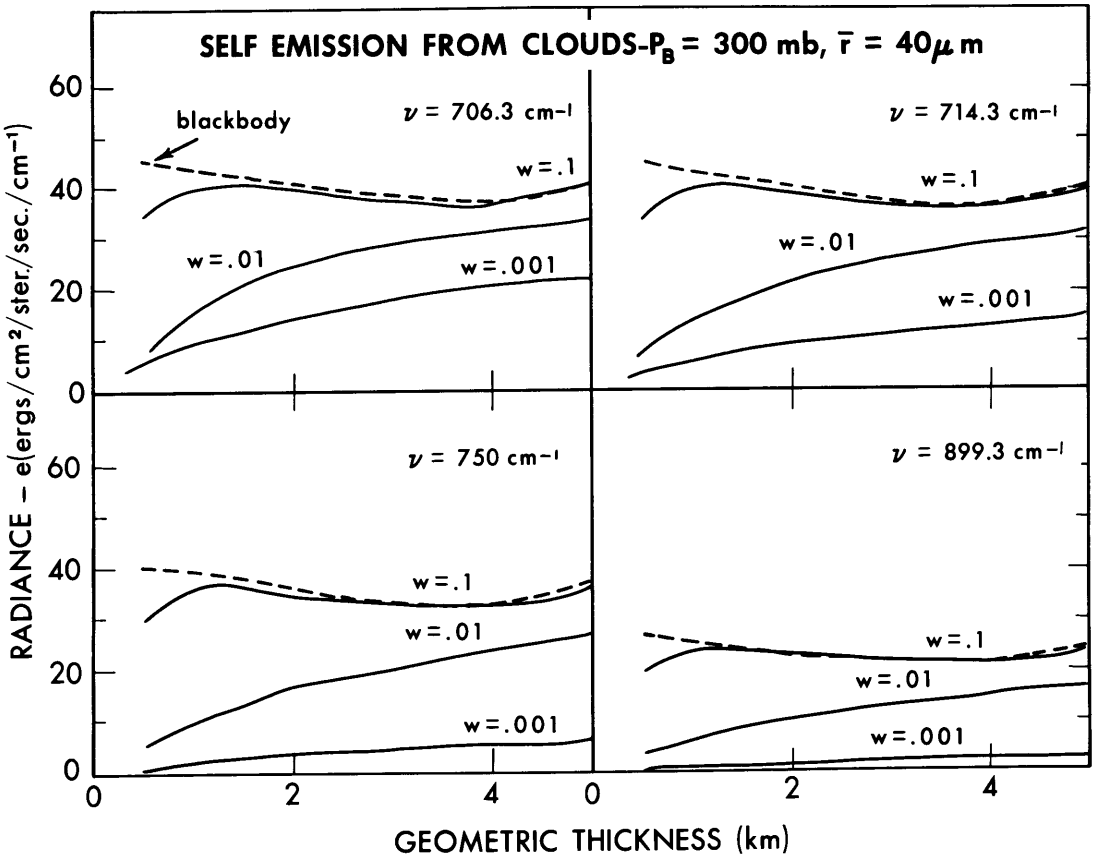

Figure 4.10--Radiance due to the self-emission from the cloud versus the geometric thickness of the cloud. w is the ice concentration in the units, g/m^3. The dashed curves are the blackbody curves.

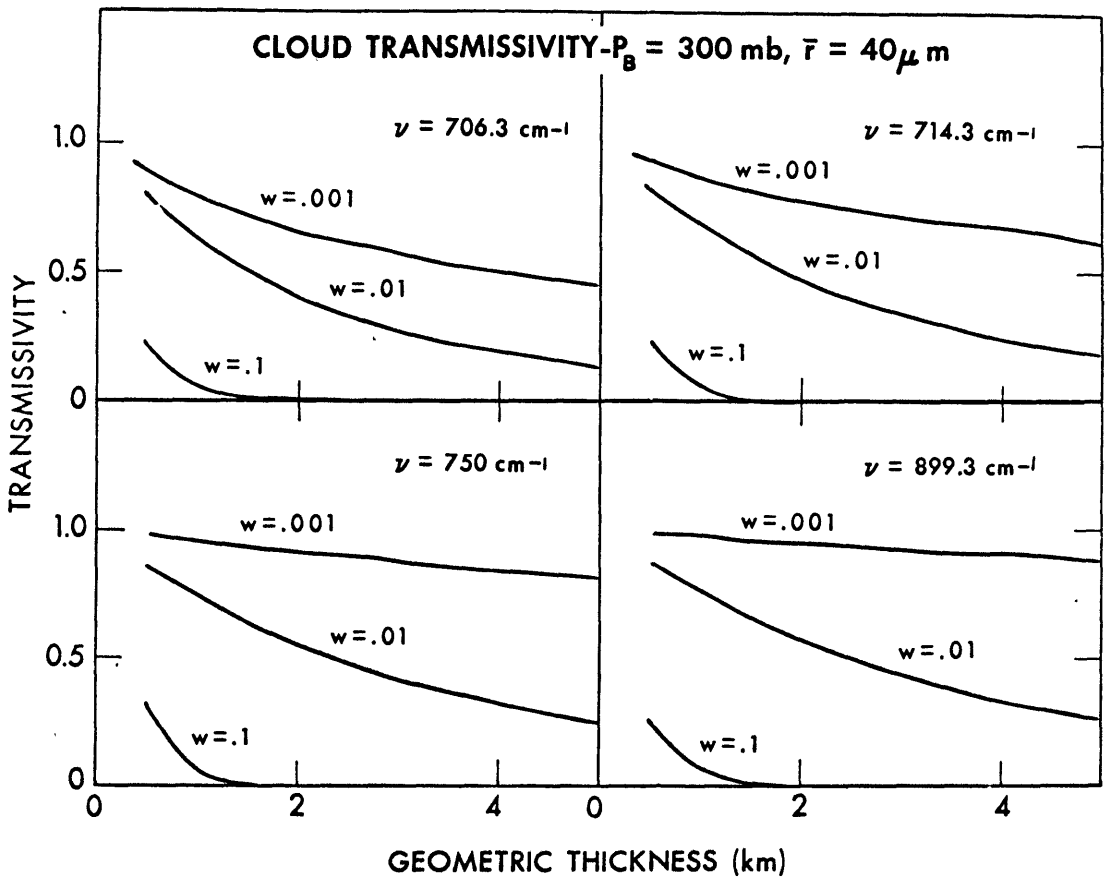

Figure 4.11--Cloud transmissivity versus the geometric thickness of the cloud for the same clouds as presented in figure 4.10.

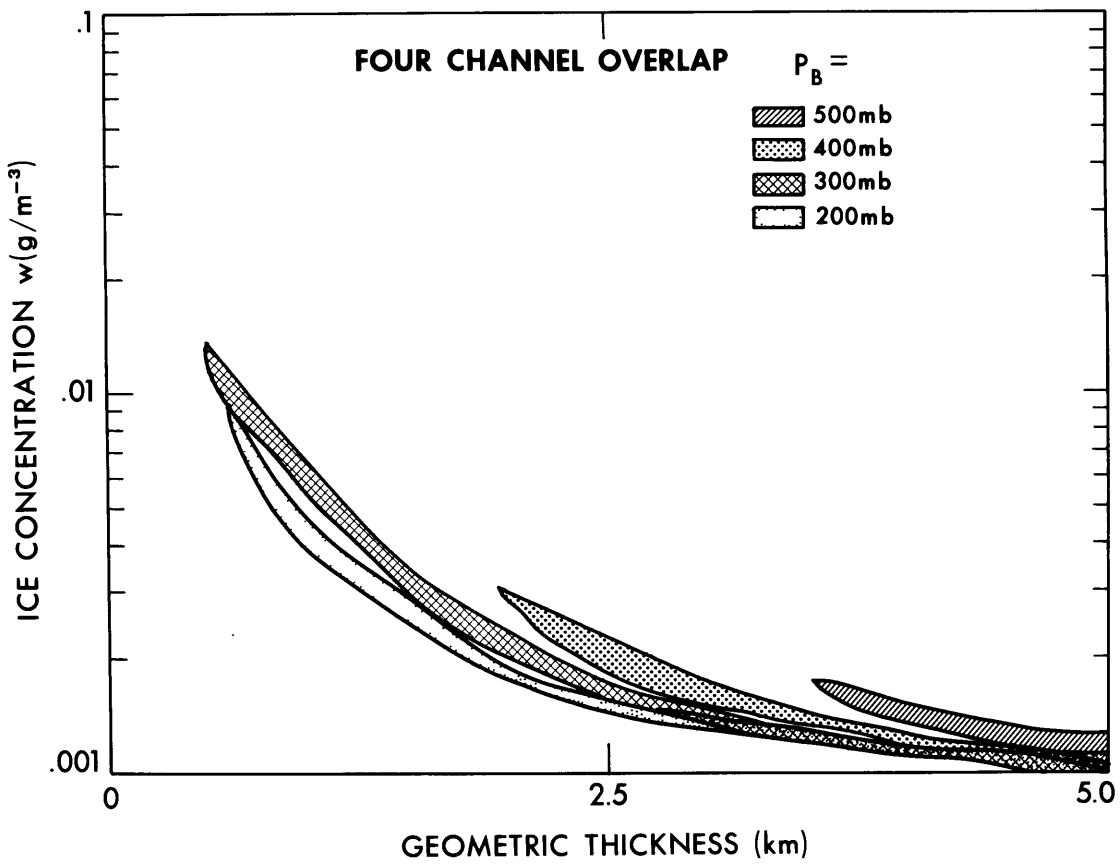

Figure 4.12--Ice conentrations versus the geometric thickness of possible cirrus clouds for the St. Ste. Marie area at 1613Z, April 24, 1969.

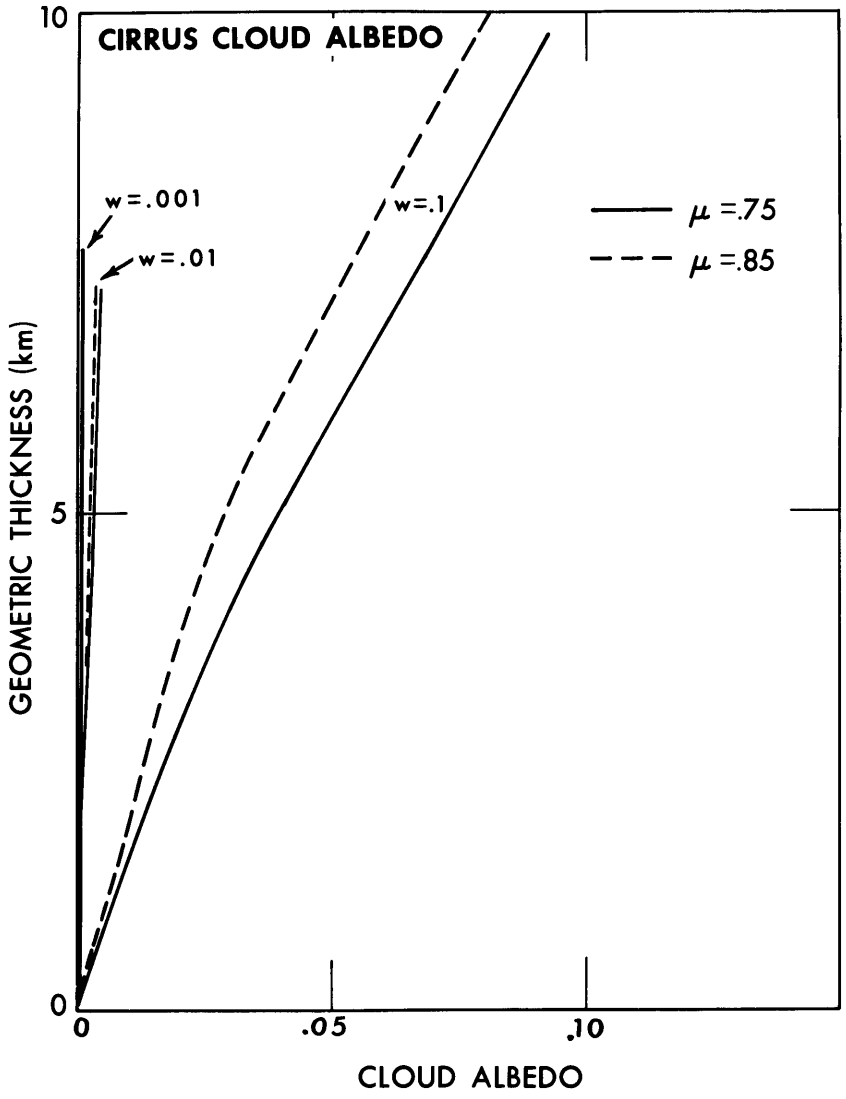

Figure 4.13--Cirrus cloud albedo versus the geometric thickness for three ice concentrations and two solar zenith angles. μ is the cosine of the solar zenith angle.

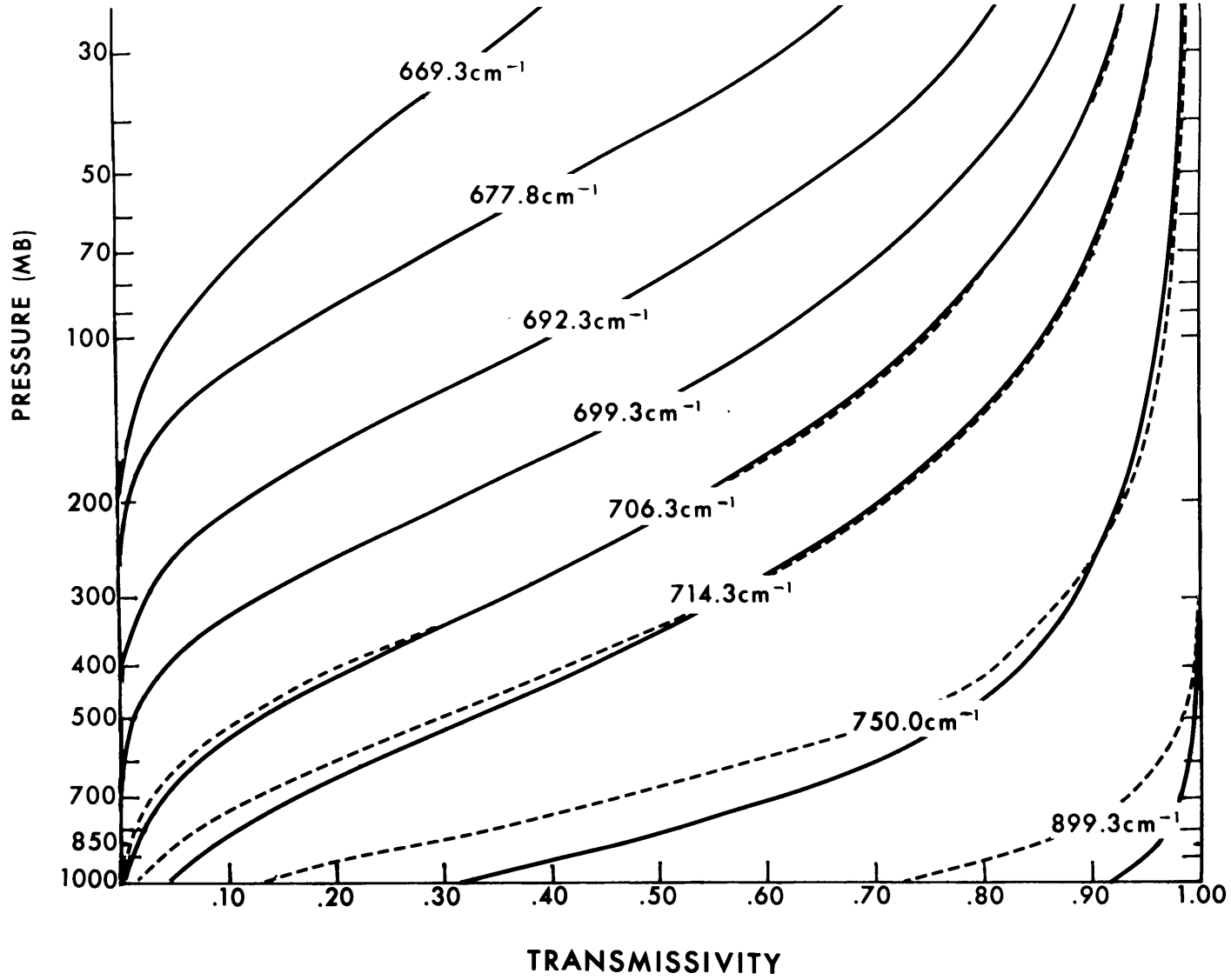

Figure 4.14--Typical transmissivities for the SIRS-A channels versus the pressure. Solid lines are for high latitude and dashed lines are for low latitude (from W. Smith).

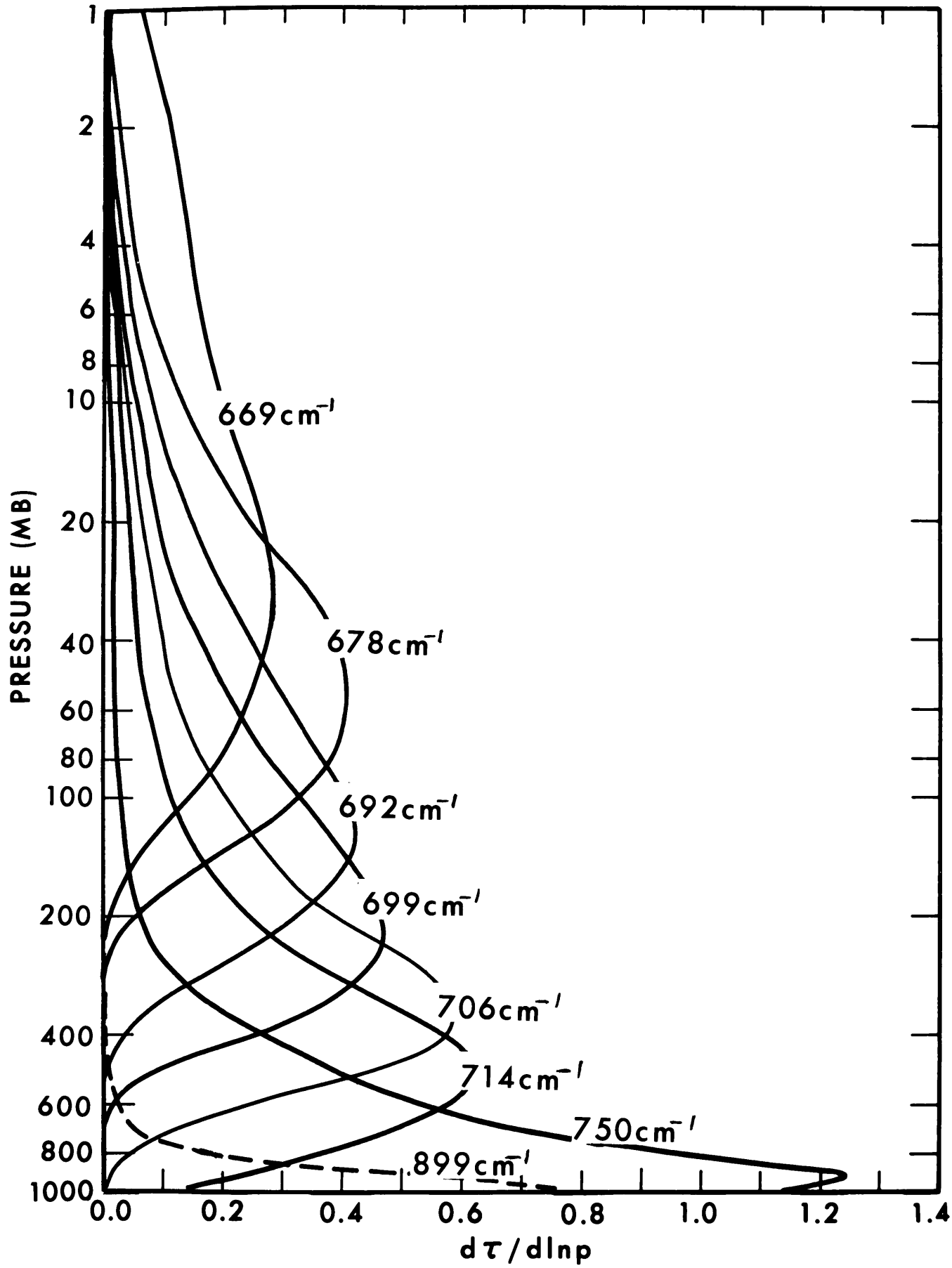

Figure 4.15--Typical weighting functions, d τ/d ln p for the SIRS-A channels versus the pressure (from W. Smith).

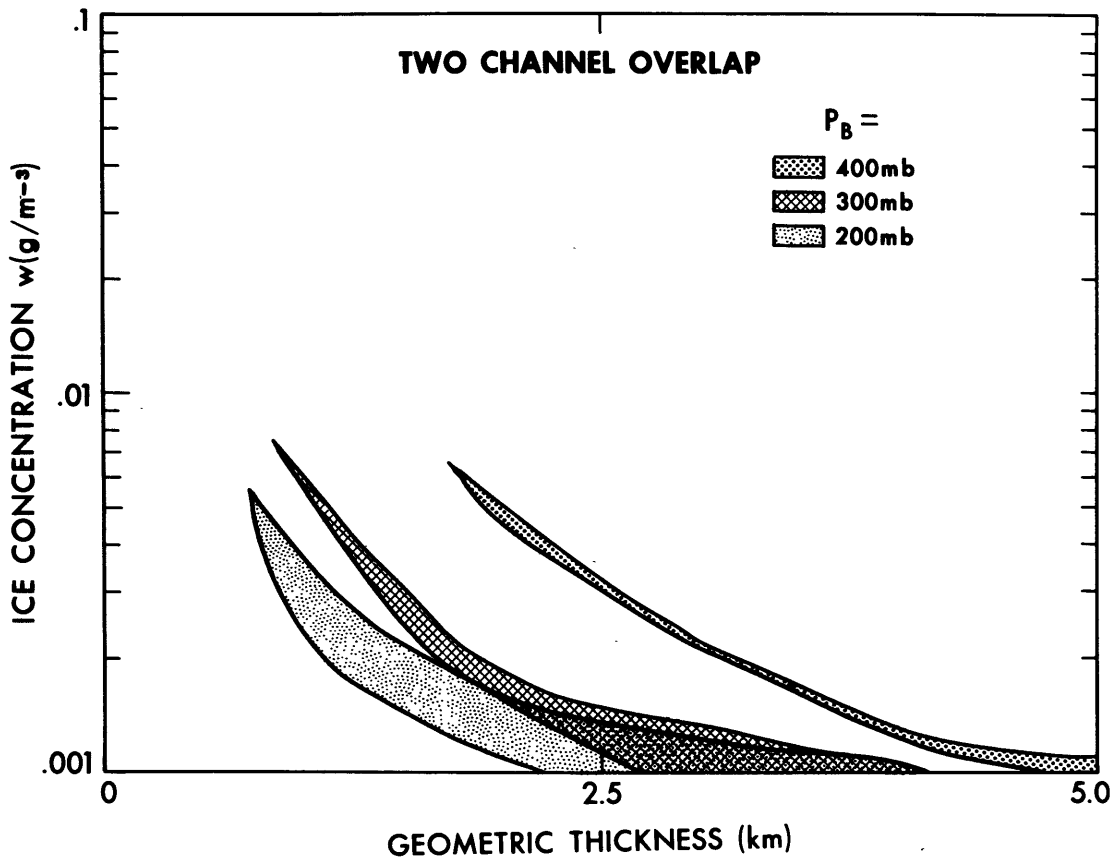

Figure 4.16--Ice concentration versus the geometric thickness of possible cirrus clouds for the Fort Worth area at 1731Z, April 22, 1969.

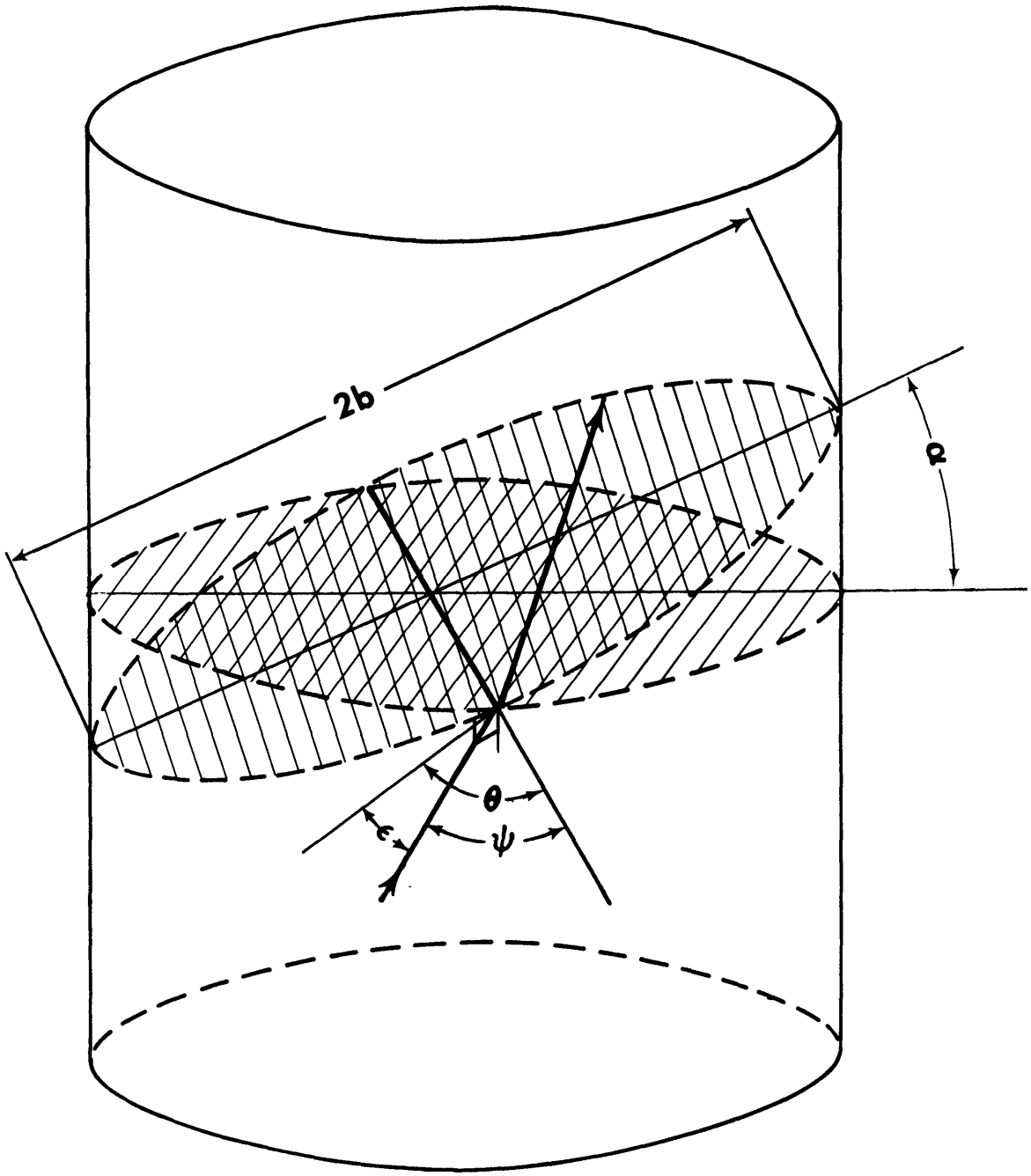

Figure A.1--Geometry of refraction through a cylinder.

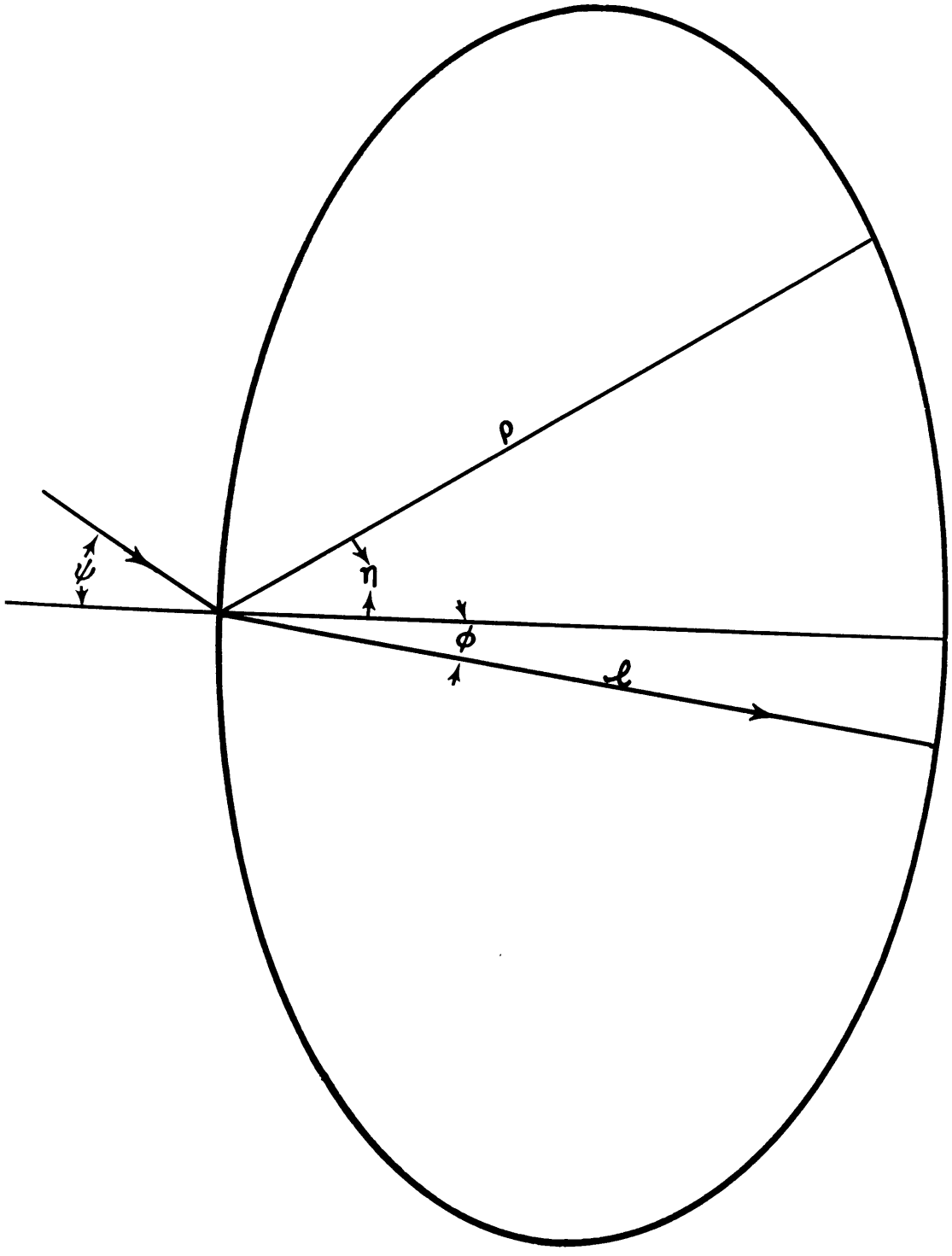

Figure A.2--Elliptical cross-section of cylinder containing refracted rays.

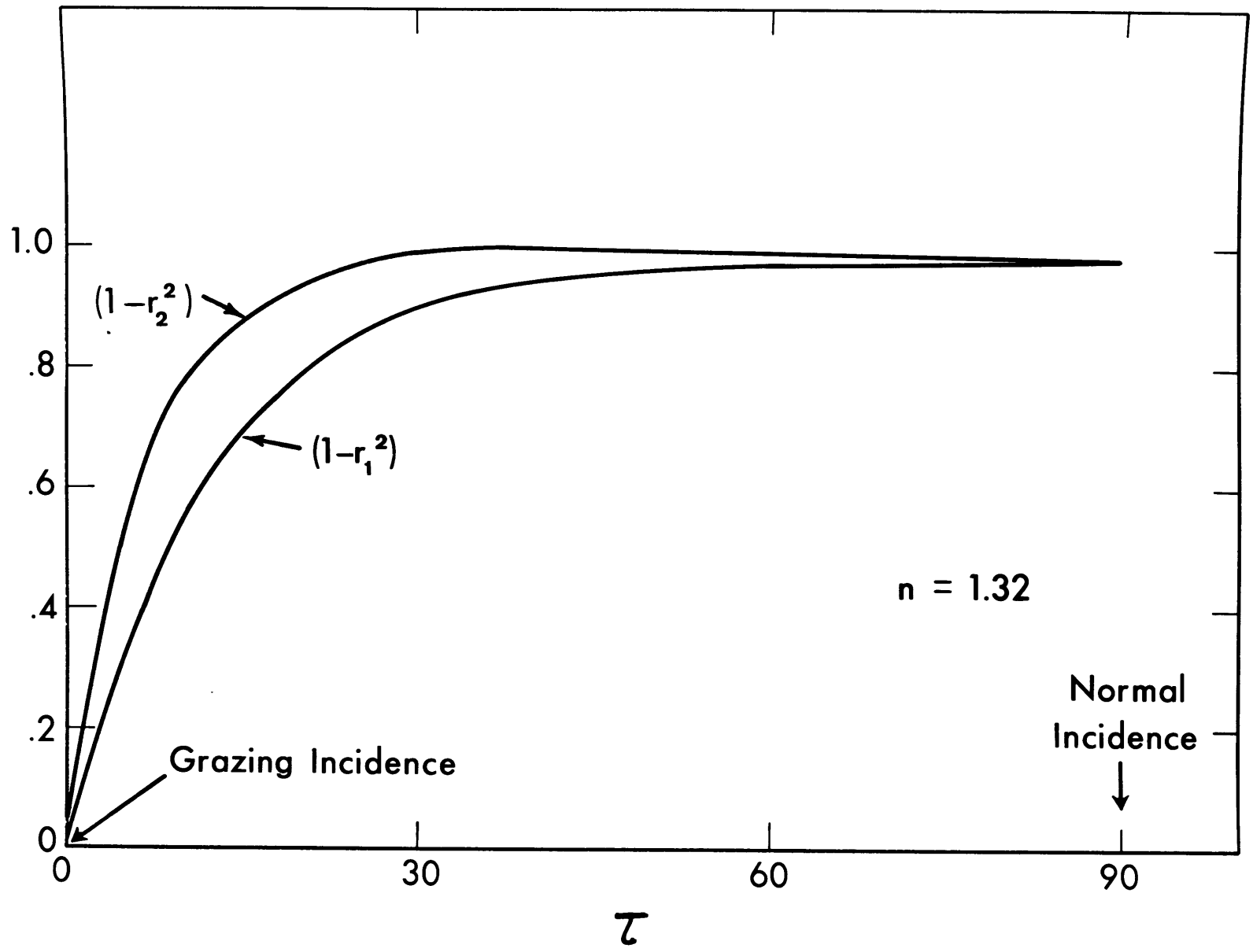

Figure A.3--Fractions of the incident radiation entering a cylinder for the two polarizations versus the angle of incidence τ. The index of refraction n = 1.32.

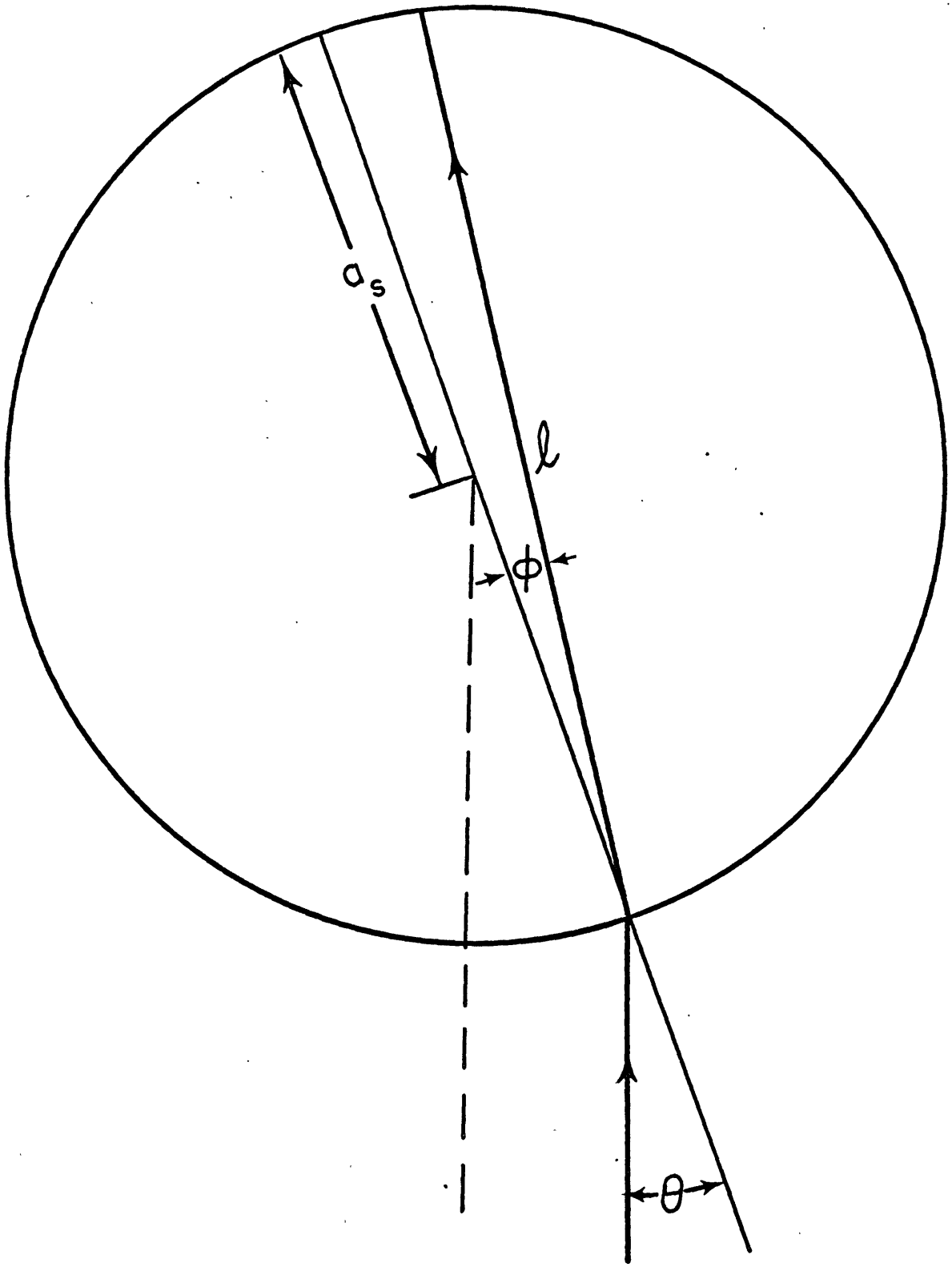

Figure A.4--Geometry of refraction through a sphere.

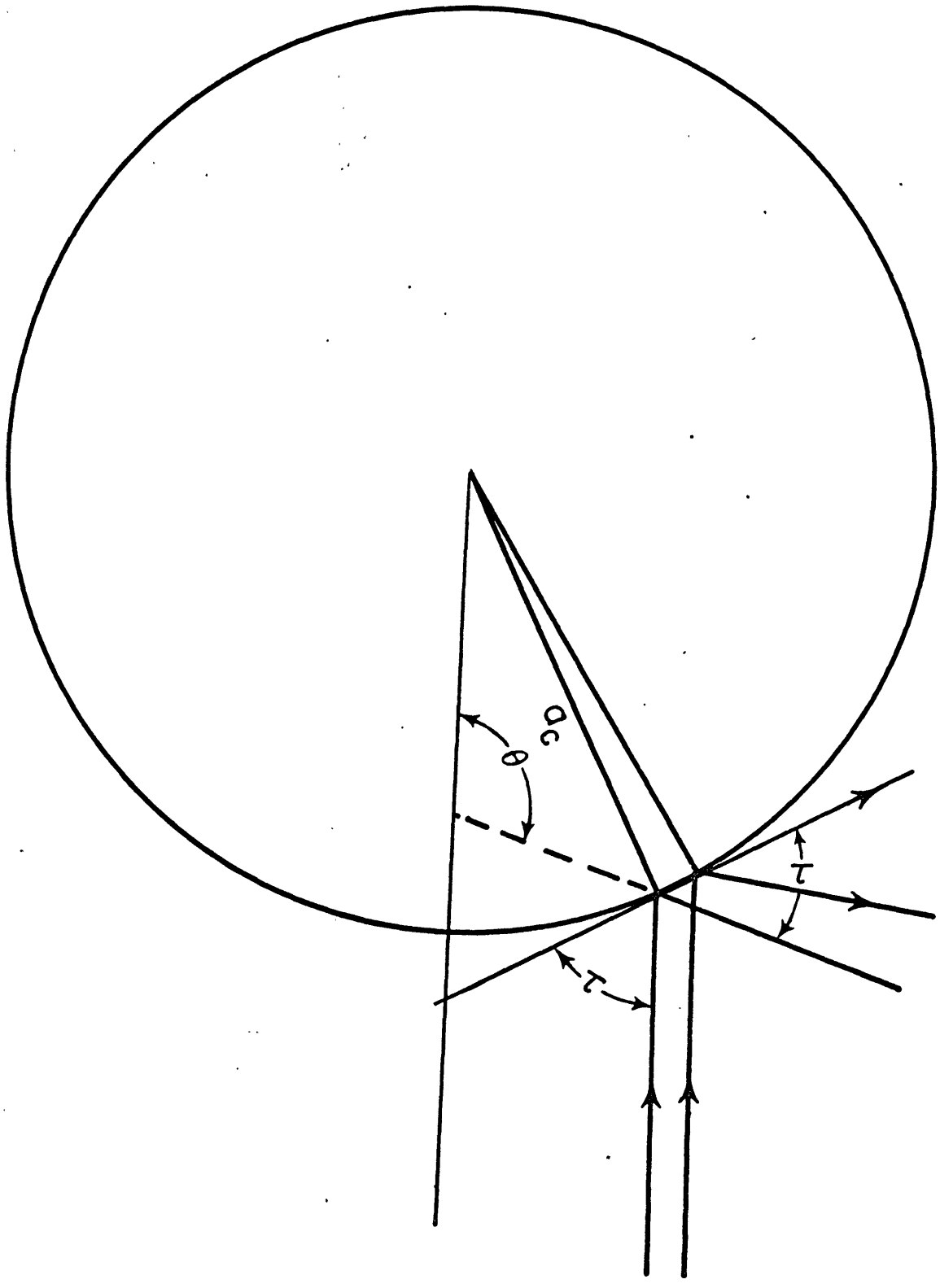

Figure B.1--Geometry of reflection from a cylinder (normal incidence).

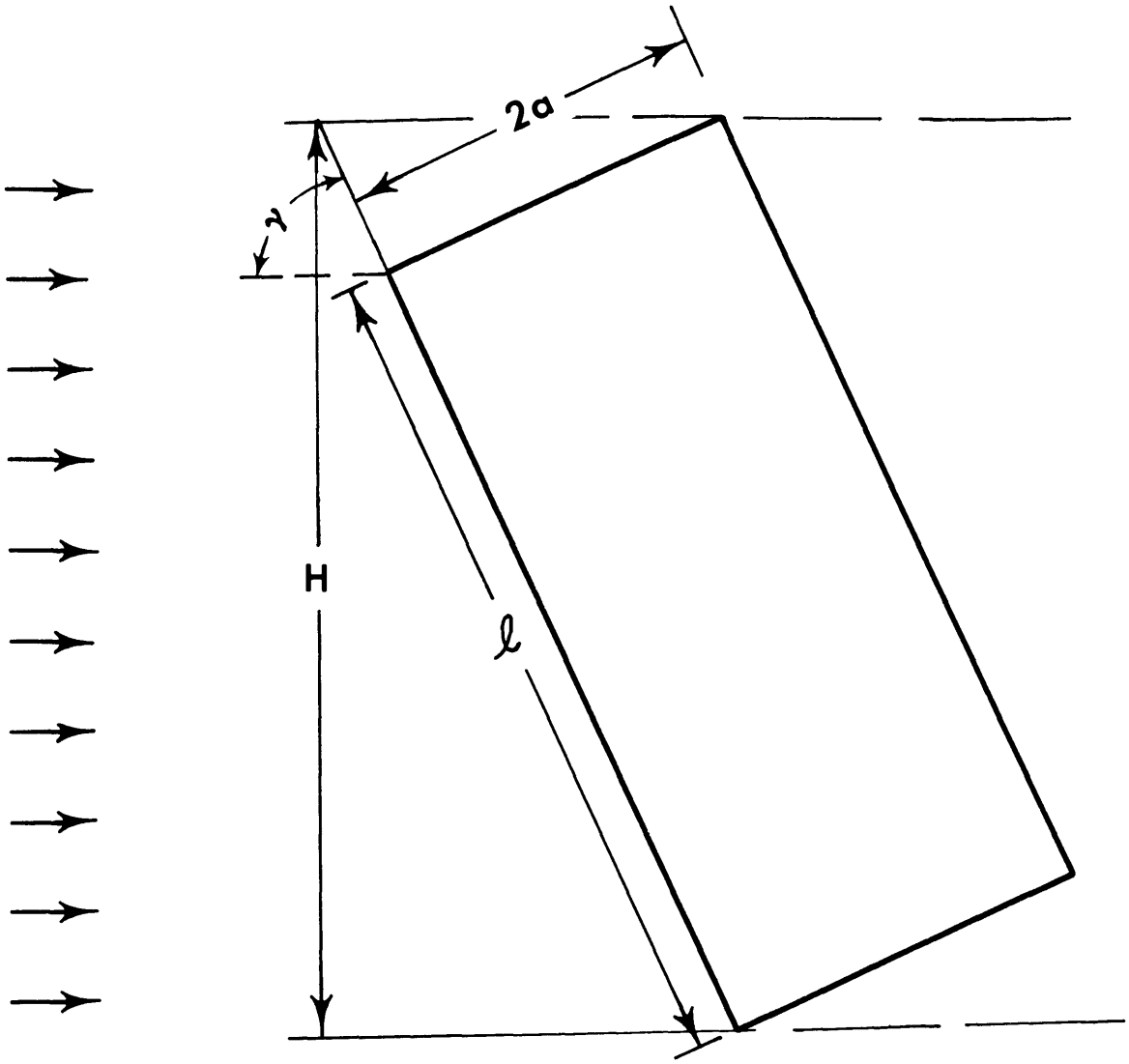

Figure C.1--Geometry of the diffraction from a rectangular solid.

BIBLIOGRAPHY

Albrecht, F., 1933: Theoretische Untersuchungen über den Strahlungsumsatz in Wolken. Meteor. Z., 50, 478-486.

Aldrick, J. B., 1919: Reflecting power of clouds. Smithson. Misc. Coll., 69, No. 10, 9 pp.

Barnes, J. C. and D. Chang, 1968: Accurate cloud cover determination and its effect on albedo computations. Final Rept. GSFC-9G53-12, Allied Research Associates, Inc., 82 pp.

Bellman, R., H. Kagiwada, R. Kalaba and S. Ueno, 1965: Computational solution of radiative transfer problems in cloud physics. Defense Documentation Center-Ad615423, The Rand Corporation, 11 pp.

Cheltsov, N. I., 1952: Reflection, transmission, and absorption of energy in some cloud forms. Trudy T_sAO, No. 8.

Cherrix, G. T. and B. A. Sparkman, 1967: A preliminary report on bidirectional reflectances of stratocumulus clouds measured with an airborne medium resolution radiometer. GSFC-X-622-67-48, 33 pp.

Dietzius, R., 1922: Die Lichtdurchlässigkeit und die Albedo von Nebel und Wolken. Beitr. Physik fr. Atmos., 10, 202-206.

Drayson, S. R., 1967: The calculation of long-wave radiative transfer in planetary atmospheres. The University of Michigan, 07584-1-T, 110 pp.

_____, 1969: Investigation of atmospheric absorption for remote sensing applications. The University of Michigan, 01427-1-F, 20 pp.

Feigelson, E. M., 1964: Light and Heat Radiation in Stratus Clouds. Moscow, Academy of Sciences of the U.S.S.R., Institute of the Physics of the Atmosphere, 245 pp.

Fletcher, R. D. and D. Sartor, 1952: Cirrus. Weatherwise, 5, 8-9.

Fritz, S., 1953: Scattering and absorption of solar energy by clouds. Ph.D. thesis, Massachusetts Institute of Technology, 175 pp.

Gates, D. M. and C. C. Shaw, 1960: Infrared transmission of clouds, J. Op. Soc. of Amer., 50, 876-882.

Griggs, M., 1968: Emissivities of natural surfaces in the 8- to 14-micron spectral window. J. Geophys. Res., 73, 7545-7551.

Hall, F., Jr., 1968: A physical model of cirrus 8-12 infrared radiance. App. Optics, 7, 2264-2269.

Hewson, E. W., 1943: Reflection, absorption, and transmission of solar radiation by fog and cloud. Q. J. Roy. Met. Soc., 69, 47-62.

Hodkinson, J. R. and I. Greenleaves, 1963: Computations of light scattering and extinction by spheres according to diffraction and geometrical optics, and some comparison with the Mie theory. J. Op. Soc. of Amer., 53, 577-588.

Howell, H. B. and H. Jacobowitz, 1970: Matrix method applied to the multiple scattering of polarized light. J. Atmos. Sci., 27 (in press).

Hulburt, E. O., 1943: Propagation of radiation in a scattering and absorbing medium. J. Op. Soc. of Amer., 31, 42-45.

Hulst, van de, 1957: Light Scattering By Small Particles, New York, John Wiley and Sons, Inc., 47 pp.

_____, 1963: A New Look at Multiple Scattering. New York, NASA Goddard Space Flight Center, 81 pp.

Humphreys, W. J., 1964: Physics of the Air. New York, Dover Publications, Inc., 676 pp.

Jayaweera, K. O. L. F. and B. J. Mason, 1965: The behavior of freely falling cylinders and cones in a viscons fluid. J. Fluid Mech., 22, 709-720.

_____, 1965: The falling motions of loaded cylinders and discs simulating snow crystals. Q. J. Roy. Met. Soc., 92, 151-156.

Kampe, H. J. Anfm and H. K. Weickmann, 1951: The influence of temperature on the shape of ice crystals growing at water saturation. J. Meteor., 8, 168-174.

_____, 1957: Physics of clouds. Meteorological Research Reviews, 3, 182-225.

Kuhn, P. M., 1963: Measured effective long-wave emissivity of clouds. Mon. Wea. Rev., 91, 635-640.

_____, and H. K. Weickmann, 1969: High altitude radiometric measurements of cirrus. J. Appl. Meteor., 8, 147-154.

Luckiesh, M., 1919: Aerial Photometry. Astrophys. J., 49, 108-130.

McDonald, R. K. and R. W. Delterne, 1963: Cirrus infrared reflection measurements. J. Op. Soc. of Amer., 53, 860-868.

Mecke, R., 1921: Uber Zerstreuung und Beugung des Lichtes durch Nebel und Wolken. Ann. Physik, 65, 257-273.

Mee, J. R. and R. E. Williamson, 1965: Measurement and effect of atmospheric factors on a laminar flow control aircraft. Proc. of the 5th Annual Nat. Conf. On Environmental Effects On Aircraft and Propulsion Systems.

Mie, G., 1908: Beigrade für optik trufen medien speziell kolloidaler Metallosungen. Ann. der Physik, 25, 377-445.

Mossop, S. C. and A. Ono, 1969: Measurements of ice crystal concentration in clouds. J. Atmos. Sci., 26, 130-137.

Murgatroyd, R. J. and P. Goldsmith, 1953: Cirrus clouds over southern England. Paper of the Meteor. Research Comm., London, M.R.P., No. 833, 13 pp.

Nakaya, U. and Y. Sekido, 1936: General classification of snow crystals and their frequency of occurrence. J. Faculty Sci. Hokkaido Imper. Univ., Ser. 11, 1, 243, 264.

Nakaya, U., 1951: The formation of ice crystals. Compendium of Meteorology, Boston, Amer. Met. Soc., 207-220.

_____, 1954: Snow Crystals: Natural and Artificial. Cambridge, Harvard University Press, 174 pp.

Neiburger, M., 1949: Reflection, absorption, and transmission of insolation by stratus cloud. J. Meteor., 6, 98-104.

Ono, A., 1969: The shape and riming properties of ice crystals in natural clouds. J. Atmos. Sci., 26, 138-147.

Plass, G. N. and G. Kattawar, 1968: Monte Carlo calculations of light scattering from clouds. Applied Optics, 7, 415-419.

Rodgers, C. D., 1967: The use of emissivity in atmospheric radiation calculations. Q. J. Roy. Met. Soc., 93, 43-53.

Ruff, I., R. Koffler, S. Fritz, J. Winston, and P. K. Rao, 1967: Angular distribution of solar radiation reflected from clouds as determined from TIROS IV radiometer measurements. NESC-38, 64 pp.

Saiedy, F., H. Jacobowitz and D. Q. Wark, 1967: On cloud-top determination from Gemini-5, J. Atmos. Sci., 24, 63-69.

Salomonson, V. V. and W. E. Marlatt, 1968: Anisotropic solar reflectance over white sand, snow, and stratus cloud. Atmos. Sci. Paper No. 120, Dept. of Atmos. Sci., Colorado State U.

Schaefer, V. J., 1962: Condensed water in the free atmosphere in air colder than -40°C. J. Appl. Meteor., 1, 481-488.

Schuster, A., 1905: Radiation through a foggy atmosphere. Astrophys. J., 21. 1-22.

Smith, W. L., 1969: A polynomial representation of carbon dioxide and water vapor transmission. NESC-47, 20 pp.

Stone, R. G., 1957: A compendium on cirrus and cirrus forecasting. AWS, TR 105-130.

Twomey, S., H. Jacobowitz, and H. B. Howell, 1966: Matrix methods for multiple scattering problems. J. Atmos. Sci., 23, 289-296.

_____, 1967: Light scattering by cloud layers. J. Atmos. Sci., 24, 70-79.

United States Air Force, 1960: Handbook of Geophysics. New York, The Macmillan Co., 673 pp.

Valovcin, R. F., 1968: Infrared measurements of jet-stream cirrus. J. Appl. Meteor., 7, 817-826.

Weickmann, H. K., 1945: Formen and Bildung atmospharischer Eiskristalle. Beitr. Phys., Frei. Atmos., 28, 12-52.

_____, 1947: Die Eisphase in der Atmosphare, Reports and Translations, 716, Ministry of Supply, London, 173 and 175-177.

_____, 1949: Die Eisphase in der Atmosphare. Ber. Dent. Wetterd., 6, 54 pp.

Wiener, C., 1907: Die Helligkeit des klaren Himmels und die Beleuchtung durch Sonne, Himmel und Ruckstrahlung, Abhandl. Kaiser-Leop-Carol, Deutech, Akad. Katurforsch, 73, 1-240.

Williams, J. E., ed., 1958: World Atlas. Englewood Cliffs, New Jersey, Prentice Hall, 122 pp.

Yamamoto, G., M. Tanaka, and K. Kamitani, 1966: Radiative transfer in water clouds in the 10-micron window region. J. Atmos. Sci., 23, 305-313.